UNIVERSITY OF CALIFORNIA, SAN DIEGO

# Investigation of Turbulence-Driven Shear Flows in Toroidal and Cylindrical Plasmas

A dissertation submitted in partial satisfaction of the
requirements for the degree
Doctor of Philosophy

in

Engineering Sciences (Engineering Physics)

by

Rongjie Hong

Committee in charge:

Professor George Robert Tynan, Chair
Professor Farhat N. Beg
Professor Patrick H. Diamond
Professor Stefan G. Llewellyn Smith
Professor Kevin B. Quest

2017

The dissertation of Rongjie Hong is approved, and it is acceptable in quality and form for publication on microfilm and electronically:

_____

_____

_____

_____

_____

Chair

University of California, San Diego

2017

DEDICATION

To My Parents, *Manqing* and *Shaojin*.

TABLE OF CONTENTS

LIST OF FIGURES

ACKNOWLEDGEMENTS

Many thanks go, first of all, to my advisor, Prof. George Tynan, for his constant encouragement and support in the past five years. I greatly appreciate our scientific discussions, in which he always reminds me of the big picture and helps me improve my research in many aspects. Meanwhile, George also gave me great freedom to explore various problems, even though they were not directly related to my thesis. Those runaway explorations, although not included in this thesis, let me know how to be an independent scientist. In Chinese traditional culture, an advisor is not only a teacher but also seen as an exemplar of the life. George is such an excellent model for me in many ways, although I doubt he has ever known that. I still remember that, in a small casual conversation, he talked about why he entered fusion energy research from industry, believing that being rich does not automatically lead to a rich life. This idea had a subtle influence on me. Whenever I felt frustrated and had a thought of leaving this area, I would take a step back and tell myself to be patient and fight one more round.

I also owe my deep gratitude to Prof. Patrick Diamond. Pat spent a lot of time explaining relevant physics concepts to me; he is truly an excellent teacher. His high standard on the quality of scientific work is admirable. I will never forget the days when I suffered from plasma physics courses given by Pat. Such torture extremely expanded the scope of my knowledge in plasma physics. The strict training I got from him will definitely benefit my career in the future. (*I will keep reading Lev Davidovich!*)

I should give my sincere gratitude to other committee members, Prof. Farhat Beg, Prof. Stefan Llewellyn Smith and Prof. Kevin Quest. Thank you all very much for the invaluable comments and suggestions on my thesis research.

I would also like to thank other research scientists, graduate students and staffs with whom I worked during my study in the CSDX and PISCES group. Particularly, I want to thank Jiacong Li for our fruitful discussions on how to explain our data using

relevant physics models. I also spent most of the time in UCSD working closely with Dr. Saikat Chakraborty Thakur, as well as Leo Chousal and Rolando Hernandez, on our beloved linear device — CSDX. Saikat, thank you for sharing most of the laborious work in the lab. Without your help I could not have finished this thesis on time.

Finally, I want to thank my parents for their endless encouragement and support during these years, and appreciate their understanding of my few visits due to the busy work. Many thanks to my fiancee, Yiqiao. Thanks for loving me the way you do; you make me want to be a better man.

Chapter 2, in part, has been submitted for publication of the material as it may appear in Nuclear Fusion, 2017, R Hong, G R Tynan, P H Diamond, L Nie, D Guo, L Ting, R Ke, Y Wu, B Yuan, and M Xu. Copyright IOP Publishing, 2017. The dissertation author was the primary investigator and author of this paper.

Chapter 3, in part is currently being prepared for submission for publication. R Hong, J C Li, S C Thakur, R Hajjar, P H Diamond, and G R Tynan. The dissertation author was the primary investigator and author of this material.

The text and data in Chapter 4 is a reprint of the material as it appears in Plasma Physics and Controlled Fusion, 2017, R Hong, S J Wukitch, Y Lin, J L Terry, I Cziegler, M L Reinke and G R Tynan. Copyright 2017 IOP Publishing. The dissertation author was the primary investigator and author of this paper.

The density limit physics study is partially supported by the Chinese National Fusion Project for ITER under Grant No 2013GB107001, the National Natural Science Foundation of China under Grant Nos 11375053 and 11575055, and the International S&T Cooperation Program of China under Grant No 2015DFA61760.

The study on RF-induced plasma flows and potentials is supported by the U.S. DoE, Office of Science, Office of Fusion Energy Sciences, User Facility Alcator C-Mod under DE-FC02-99ER54512 and DE-SC 0010720.

## VITA

| | |
|---|---|
| 2009 | B.Sc. in Applied Physics, Beijing University of Aeronautics and Astronautics, Beijing, China |
| 2012 | M.Sc. in Plasma Physics, Institute of Plasma Physics, Chinese Academy Of Sciences, Hefei, China |
| 2012–2017 | Graduate Student Researcher, Center for Energy Research, University of California, San Diego, USA |
| 2017 | Teaching Assistant, Department of Mechanical and Aerospace Engineering, University of California, San Diego, USA |
| 2017 | Ph.D. in Engineering Sciences (Engineering Physics), University of California, San Diego, USA |

## PUBLICATIONS

R Hong, S J Wukitch, Y Lin, J L Terry, I Cziegler, M L Reinke and G R Tynan. "Characterization of SOL plasma flows and potentials in ICRF-heated plasmas in Alcator C-Mod", *Plasma Physics and Controlled Fusion*, 59:105008, 2017.

R Hong, G R Tynan, P H Diamond, L Nie, D Guo, T Long, R Ke, Y Wu, B Yuan, and M Xu. "Edge Shear Flows and Particle Transport near the Density Limit of the HL-2A Tokamak", accepted by *Nuclear Fusion*.

R Hong, J C Li, S C Thakur, R Hajjar, P H Diamond, and G R Tynan. "Generation of Intrinsic Sheared Parallel Flow and its Connection to Mean Azimuthal Flow in Cylindrical Magnetized Plasmas", submitted to *Physics of Plasmas*.

R Hong, J C Li, S C Thakur, R Hajjar, P H Diamond, and G R Tynan. "Tracing the Pathway from Drift-Wave Turbulence with Broken Symmetry to the Onset of Axial Mean Flow", submitted to *Physical Review Letters*.

ABSTRACT OF THE DISSERTATION

**Investigation of Turbulence-Driven Shear Flows in Toroidal and Cylindrical Plasmas**

by

Rongjie Hong

Doctor of Philosophy in Engineering Sciences (Engineering Physics)

University of California, San Diego, 2017

Professor George Robert Tynan, Chair

Turbulence-driven shear flows in both transverse and parallel directions have been investigated in a tokamak (HL-2A) and a linear device (CSDX). The first part of this study is devoted to the evolution of edge shear flow and its effect on regulating turbulent transport that have long been suspected to play an important role in plasmas operating near the Greenwald density limit. In this study, equilibrium profiles as well as the turbulent particle flux and Reynolds stress across the separatrix in the HL-2A tokamak are examined as $n_G$ is approached in ohmic L-mode discharges. As the normalized line-averaged density is raised, the shearing rate of the mean poloidal flow drops, and

the turbulent drive for the low-frequency zonal flow (the Reynolds power) collapses. Correspondingly, the turbulent particle transport increases drastically with increasing collision rates. The geodesic acoustic modes (GAMs) gain more energy from the ambient turbulence at higher densities, but have smaller shearing rate than low-frequency zonal flows. The increased density also introduces decreased adiabaticity, which not only enhances the particle transport but is also related to reduction in the eddy-tilting and the Reynolds power. Both effects may lead to cooling of edge plasmas and therefore the onset of MHD instabilities that limit the plasma density. The second part is focused on the generation of intrinsic parallel flow in a linear magnetized device–CSDX. Generation of a radially sheared axial flow by a turbulent Reynolds stress is observed in the CSDX linear magnetized plasma device. As the magnetic field increases, the density gradient steepens and a finite parallel Reynolds stress develops and drives a radially sheared mean parallel flow. The plasma fluctuations are collisional drift waves driven by the density gradient. The turbulent stress is the dominant force driving the axial flow, and is sufficient to reverse the plasma flow at the outer boundary. The axial flow shearing rate and the axial Reynolds power track the increasing density gradient. Moreover, the joint probability density function of radial and axial velocity fluctuations becomes highly elongated and more strongly correlated at higher magnetic field, indicating a stronger spectral asymmetry in spectral correlator. This gives rise to a finite residual stress that drives the mean parallel flow.

# Chapter 1

# Introduction

## 1.1 Energy Demands and Nuclear Fusion

The ability to obtain ample and affordable energy is often connected to the quality of human life. As illustrated in figure 1.1, a nation's Human Development Index (HDI) [UND05], which is published by United Nations and commonly regarded as a measure of life quality, depends in part on energy consumption. Clearly, to improve or maintain a high quality of life, access to adequate and economical energy is now and will continue to be a pivotal factor. While we are struggling to acquire more energy, nowadays it is chiefly from burning fossil fuels, which results in a rapid growth of greenhouse gas (GHG) emissions. GHG emissions since the Industrial Revolution has been found to be correlated with climate change and global warming issues [CBJ+00], which in turn have a significant impact on ecosystems, economies and communities [PY03, RPH+03, TCG+04]. To overcome these challenges, continued access to abundant, secure and environment-friendly energy is crucial. Nuclear fusion is such a candidate that will help us enjoy the benefits of clean, safe and affordable energy in the foreseeable future.

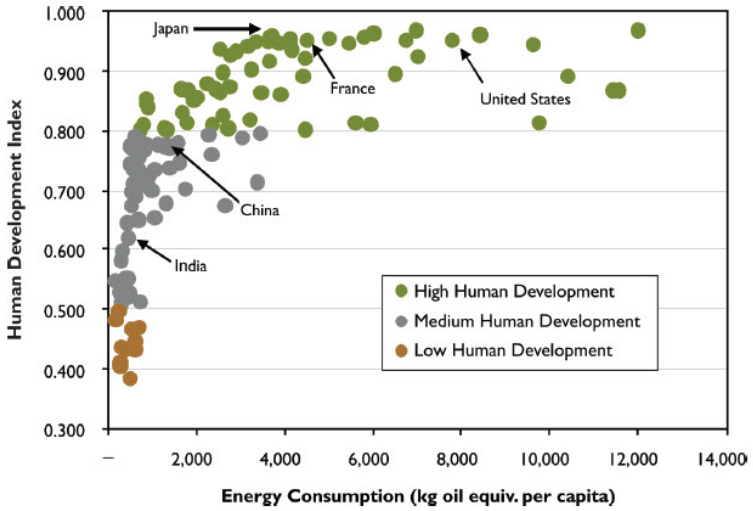


**Figure 1.1**: 2005 Human Development Index versus Energy Consumption (Per Capita Kilograms Oil Equivalent) [UND05]

**Table 1.1**: Fusion reactions with relatively large cross-sections.

| Reactants | Products |
|---|---|
| D–D | T (1 MeV) + p (3 MeV) |
| D–D | $^{3}$He (0.8 MeV) + n (2.5 MeV) |
| D–T | $^{4}$He (3.5 MeV) + n (14 MeV) |
| D–$^{3}$He | $^{4}$He (3.7 MeV) + p (14.7 MeV) |

Thermonuclear fusion is the primary energy source of stars, e.g. the sun. The nuclear fusion reactions release energy when the mass of the reactant nuclei exceeds that of the reaction products. Fusion reactions in our sun mostly rely on proton-proton interaction, whose cross-section is too small for laboratory reactions. Laboratory fusion research uses hydrogen isotopes which are more reactive. Table 1.1 lists the most important reactions used in our fusion research. The deuterium-tritium (D–T) reaction has the most favorable cross-section and can be operated at about 10 keV. The D–D reaction may have economic or environmental advantages due to the relative abundance of deuterium, but it would have to be operated at a much higher temperature (about 25 keV).

At such high temperatures for fusion reactions, the fuel is fully ionized into an

electrically neutral medium of unbound positive and negative particles, i.e. a *plasma*. High temperature plasmas cannot be confined exclusively by material walls, thus another method is required. One useful way is to confine such plasmas magnetically. As subject to Lorentz force, each charged particle moves uniformly along the magnetic field, while gyrating about the field line, i.e. executing helical orbits about an axis parallel to the field line. By bending the field lines into a ring or a doughnut shape, we expect to confine the charged particles in both parallel and perpendicular directions. Many designs of existing fusion devices, such as tokamak, stellarator and reversed field pinch (figure 1.2), are derived from this simple toroidal configuration.

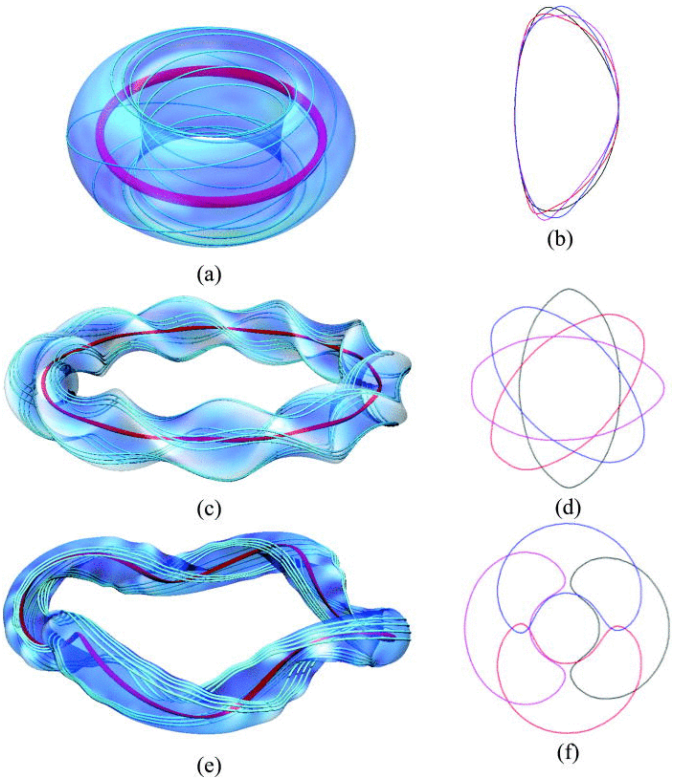


**Figure 1.2**: Schematic of some toroidal magnetic configurations (left column) and their cross-sections (right column).

## 1.2 Tokamaks

The tokamak is a kind of toroidal magnetic confinement device [WC11], which was first proposed by Igor Tamm and Andrei Sakharov in the Soviet Union. Until now, it achieves the better confinement than any other kind of magnetic fusion device. The principal magnetic field is the toroidal field $B_\varphi$. However, this field alone cannot confine the plasma efficiently. It is necessary to introduce a poloidal magnetic field $B_\theta$, such that the plasma pressure gradient $\nabla p$ is partly balanced by the magnetic force $J_\varphi \times B_\theta$. In a tokamak, this poloidal field is mainly produced by current in the plasma itself, with the current flowing in the toroidal direction. The currents and fields are illustrated in figure 1.3. The resulting magnetic field lines then have a helical trajectory around the torus. These revolving field lines will form nested toroidal magnetic flux surfaces (figure 1.4).

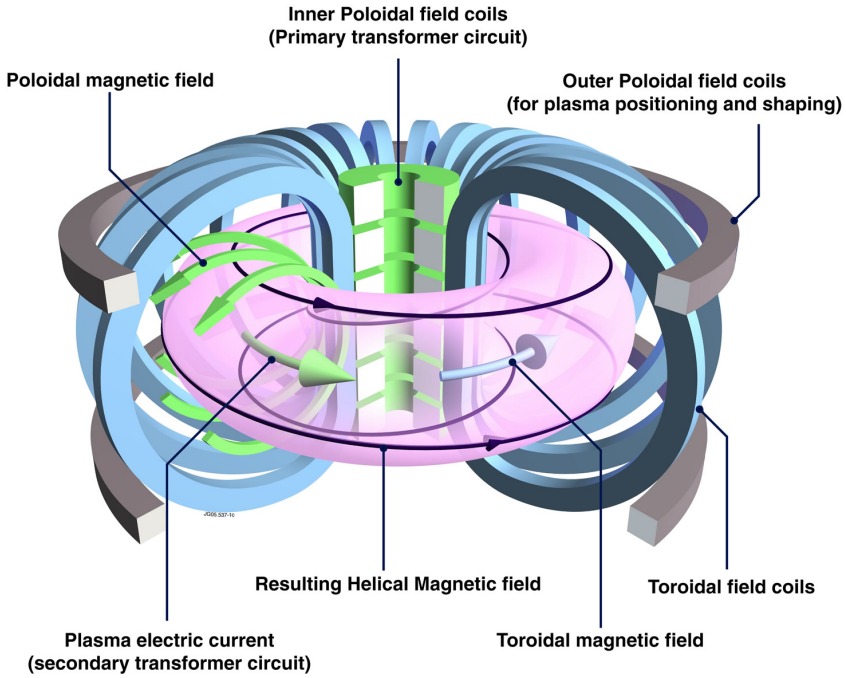


**Figure 1.3**: The toroidal field and poloidal field within the vessel of a tokamak.

The basic condition for equilibrium is that the force on the plasma be zero at all points. This requires that the magnetic force balances the force due to pressure gradient,

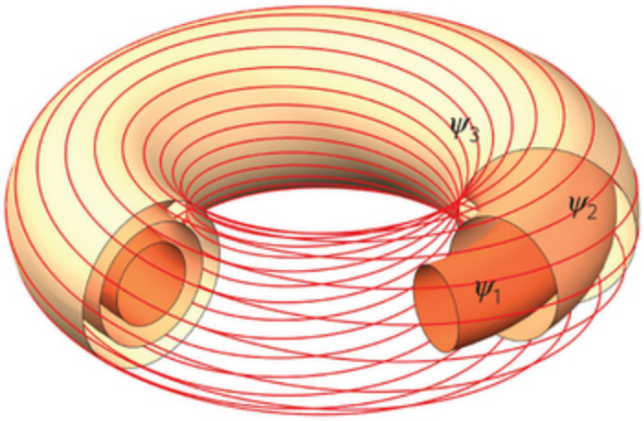


**Figure 1.4**: Magnetic flux surfaces forming a set of nested toroids.

i.e.

$$\mathbf{J} \times \mathbf{B} = \nabla p.$$

Clearly, from this equation we have $\mathbf{B} \cdot \nabla p = 0$. Therefore, there is no pressure gradient along the magnetic field lines, and the magnetic flux surfaces are surfaces of constant pressure. Then the pressure gradient only exists in radial direction, i.e. $\partial_r p = J_\varphi B_\theta - J_\theta B_\varphi$.

Unlike in an infinite straight solenoid, the magnetic field from toroidal field coils is not constant inside the coils. The basic shape of the toroidal field $B_\varphi$ is obtained from Ampere's law, that is taking a line integral around a circular toroidal circuit inside the toroidal field coils, and neglecting the small poloidal current

$$2\pi R B_\varphi = \mu_0 I_c,$$

where $R$ is the major radius and $I_c$ is the total current in the coils. Thus the radial variation of the toroidal field is

$$B_\varphi \propto \frac{1}{R}.$$

This variation is significant in present tokamaks. Later we will see its effects on the

plasma.

## 1.3 Confinement Demands and Turbulent Transport

To achieve larger economic advantages, it is desirable that fusion reactions can be self-sustained, that is in ignition. This leads to two demands on the quality of confinement:

a) the temperature must exceeds some critical temperature for significant fusion yield

b) the product of density, temperature and confinement time must exceed the ignition condition

For a D–T plasma, the critical temperature for fusion reaction is close to 10 keV, while the ignition condition is estimated as $nT\tau_E > 5 \times 10^{21}$ m$^{-3}$ keV s (see detailed derivations in [WC11]). Here the energy confinement time, $\tau_E$, is defined in terms of plasma energy content, $W$, and energy loss rate, $P_{\mathrm{L}}$, in a steady state plasma, i.e. $\tau_E = \dfrac{W}{P_{\mathrm{L}}}$. In most existing fusion devices, the nuclear power is so small that the energy loss is usually balanced by external heating power, $P_{\mathrm{H}}$, and confinement time can be determined from experimentally know quantities, i.e. $\tau_E = \dfrac{W}{P_{\mathrm{H}}}$. Similarly, the particle confinement time, $\tau_p$, is define in terms of particle content and replacement rate.

It seems possible to satisfy both demands if the confinement loss is only due to the Coulomb collisions of charged particles. However, at least as late as early 1960's [Boe64], people found that the measured cross-field fluxes are much greater than given by collisional processes by about one or two orders of magnitude, preventing us from achieving the ignition condition. These "anomalous" losses, which cannot be described by the collisional theory, are commonly regarded as *turbulent transport*, since they are ascribed to micro-turbulence (i.e. fine-scale, incoherent fluctuations) [Lie85, WCM$^+$90]. The most common family of micro-turbulence is drift wave turbulence, which can be

driven by plasma gradients [Hor99]. Using a random-walk model, we can qualitatively estimate the transport coefficients in both collisional and turbulent cases.

In the collisional theory [HH76], the random-walk step size is generally set by the width of closed banana trajectories in the steady state magnetic fields, and the step period is set by the collisional de-correlation time. At low collisionalities relevant to fusion plasmas, the cross-field transport coefficients have the form of $G_c\rho^2\nu$ , where $G_c$ is a dimensionless geometrical factor, $\rho$ is the gyroradius of the species under consideration and $\nu$ is the collision rate.

In the micro-turbulence case, the turbulence correlation length, $l_c$, is usually a multiple of the ion sound gyroradius, $\rho_s$, and the turbulence amplitude is of the order of the mixing length estimate $\left(\tilde{n}/n_0 \sim \frac{1}{k_\perp L_n}\right)$ in which the gradient of the perturbed density approximately equals the gradient of the mean density. Here, $L_n = (d_r \ln n_0)^{-1}$ is the density scale length and $k_\perp$ is the wavenumber perpendicular to the magnetic field. In electrostatic turbulence, one estimates $e\tilde{\phi}/T \sim \tilde{n}/n_0$, where $\phi$ is the electrostatic potential. Using the mixing length estimate for density perturbations, the turbulent velocity can be estimated as $\tilde{v} \sim k_\perp\tilde{\phi}/B$. As a result, the random-walk transport coefficient, $l_c\tilde{v}$, takes the form of $G_t\dfrac{T}{eB}\dfrac{\rho_s}{L_n}$, where $G_t$ is a dimensionless factor that depends on micro-turbulence types and other plasma parameters.

There is another estimate of cross-field transport, which is even worse than the gyro-Bohm scaling, i.e. the Bohm scaling. This scaling typically corresponds to large-scale turbulence or MHD situations, in which $\tilde{n}/n_0 \sim 1$ and $k_\perp l_c \sim 1$. Therefore, the transport coefficients scale as $\dfrac{T}{eB}$. Clearly, the Bohm scaling can give larger transport coefficient than gyro-Bohm case, and suggests that the transport cannot be reduced as the machine size is increased.

Both these two scalings gives much higher diffusivity than that given by collisional process in high temperature plasmas. Recently, it has also been realized that the cross-field

transport is neither pure gyro-Bohm type $\left(\sim B^{-2}\right)$ nor Bohm type $\left(\sim B^{-1}\right)$ in toroidally confined plasmas [RMS$^+$05, SRB$^+$14].

## 1.4 Improved Confinement by Shear Flows

Although the plasma confinement is limited by turbulent transport, it was observed in the early 1980's that under certain conditions there is a discontinuous improvement in confinement as the heating power is increased [WBB$^+$82]. Typically the confinement time can be increased by a factor of two. This regime of higher confinement is called the $H$-mode and the previous lower level is called the $L$-mode. The $H$-mode is achieved more readily in plasmas bounded by a separatrix. The improvement in confinement is mainly featured by a so-called edge transport barrier (ETB), i.e. steepened density and temperature gradients near the separatrix, as illustrated in figure 1.5. A number of other improved confinement regimes have also been identified.

The formation of edge transport barriers has been successfully explained by the $\mathbf{E}\times\mathbf{B}$ velocity shear model [Bur97, Ter00]. The fundamental physics involved in transport reduction is that the $\mathbf{E}\times\mathbf{B}$ sheared flows can affect the growth of and radial extent of turbulent eddies in the plasma. Both nonlinear decorrelation [BDT90] and linear stabilization effects [WKMH95] have been proposed. The basic nonlinear effect is the reduction in radial transport due to a decrease in the radial correlation length and the change in the phase between density, temperature, and potential fluctuations. On the other hand, linear stabilization effects are usually specific to various modes; one general feature is that unstable modes will be coupled to more stable modes caused by the $\mathbf{E}\times\mathbf{B}$ sheared flow.

The basic idea of turbulence decorrelation [BDT90, Bur97] is given in figures 1.6 and 1.7. In this simple model, density is treated as a passive scalar, affected by the velocity

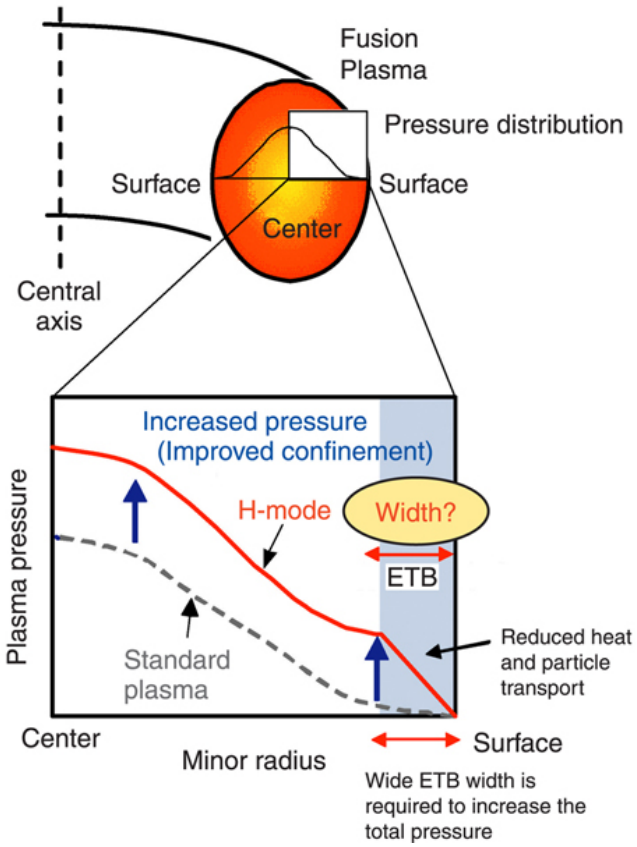


**Figure 1.5**: Schematic of pressure profiles of *H*-mode and *L*-mode. Edge transport barrier is developed in *H*-mode.

field of turbulent eddies. With no velocity shear, as shown in figure 1.6(a), the eddies coupled with a linear background density profile produce hills and valleys in the density spatial distribution. The correlation between the density and velocity perturbations then leads to radial transport (figure 1.7(a)). When a velocity shear is added, as illustrated in figure 1.7(b), the eddies are distorted and radial transport is reduced.

For linear stabilization effects of $\mathbf{E} \times \mathbf{B}$ velocity shear [WKMH95], the shear generally results in enhanced damping by coupling the unstable modes to stable modes, thus improving the overall stability of the system. Magnetic shear is often necessary in this process.

According to such velocity shear model, turbulent transport can be reduced as

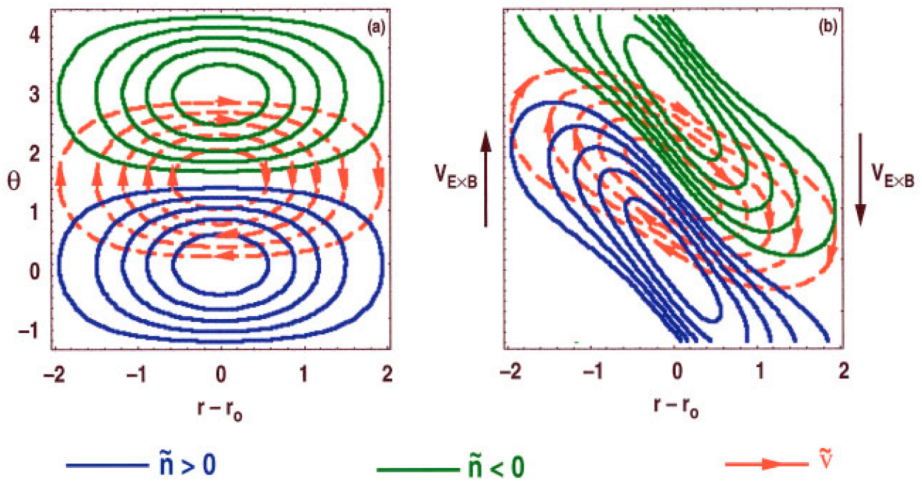


**Figure 1.6**: A simple model illustrates the effect of the $\mathbf{E} \times \mathbf{B}$ velocity shear on turbulent eddies [Bur97]. Density fluctuations (green and blue) are passive scalars convected by the eddy velocity field (red).

long as we can change the radial electric field $E_r$. The profile of $E_r$ can be altered using several methods. From the ion radial force balance equation,

$$E_r = \frac{\nabla P_i}{Z_i e n_i} - V_{\theta,i} B_\phi + V_{\phi,i} B_\theta,$$

we can see that $E_r$ can be connected to the radial gradient of ion pressure ($\nabla P_i$), parallel flow ($V_{\phi,i}$), and poloidal flow ($V_{\theta,i}$). By changing these parameters, we should be able to obtain strong sheared $E_r$ profiles in various portion of plasmas.

Although the key role of $\mathbf{E} \times \mathbf{B}$ sheared flows in sustaining the $H$-mode has been well known, the mechanism that initiates the onset of the sheared flows has remained elusive. Later, it was pointed out that the radially limited, poloidally and toroidally homogeneous $E_r \times B$ sheared flows could be developed from drift waves as a secondary instability, and that the formation of such meso-scale sheared flows could in turn regulate cross-field transport results from the micro-scale drift wave turbulence [DIIH05, Fuj09, TFM09, SMR11]. Due to their quasi-two-dimensional nature, this

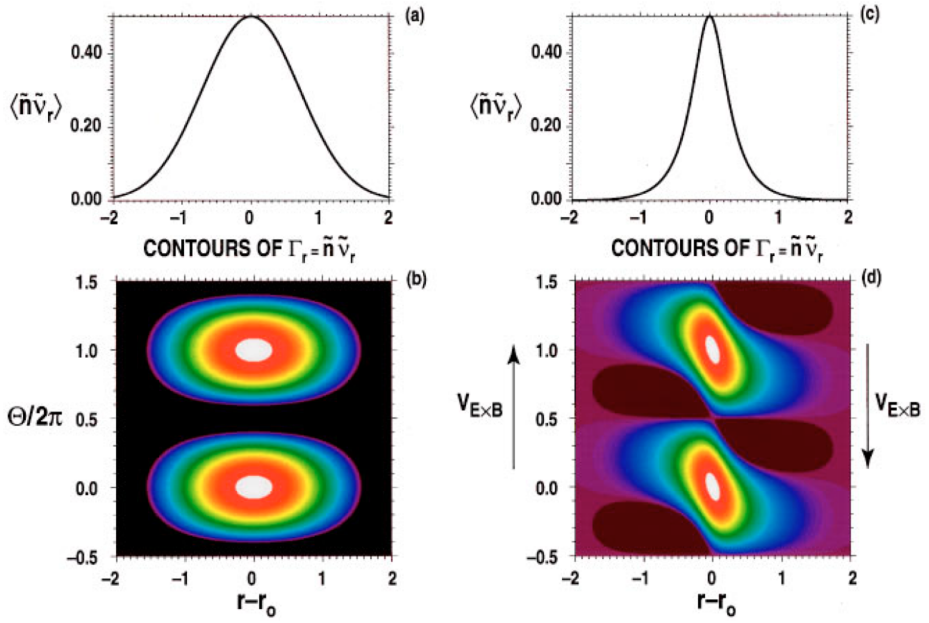


**Figure 1.7**: The effect of the $\mathbf{E} \times \mathbf{B}$ velocity shear on the particle flux $\langle \tilde{n}\tilde{v} \rangle$ [Bur97]. Eddies and shear flows are the same as the model shown in figure 1.6.

sheared poloidal $E_r \times B$ flows are called zonal flows (ZFs) by analogy to large-scale atmospheric and oceanic flows.

The relevant driving force for zonal flows results from the divergence of the Reynolds stress,

$$\mathcal{F}_\theta^{\mathrm{RS}} = -m_\mathrm{i} n \nabla_r \langle \tilde{v}_r \tilde{v}_\theta \rangle.$$

This Reynolds force can be incorporated in to ion force balance equation, leading to radial electric field generation through the same mechanism as described above. Bispectral analysis of the ZF-turbulence interaction [TFM09, SMR11] show that the kinetic energy transfer to the zonal flow comes predominantly from smaller scales. Small-scale eddies are finally absorbed by the large-scale sheared flow: the eddies are tilted, elongated and finally curled up by the flow shear (figure 1.8). This 'tilt-stretch-absorb' process was also observed in two-dimensional fluid turbulence, and is a very efficient process to transfer energy from the micro-turbulence to the large-scale shear flow [SY85]. This

self-regulating ZF-turbulence interaction has emerged as an important mechanism of the formation of edge and core transport barriers [Bur06, Fuj09, TCD+16].

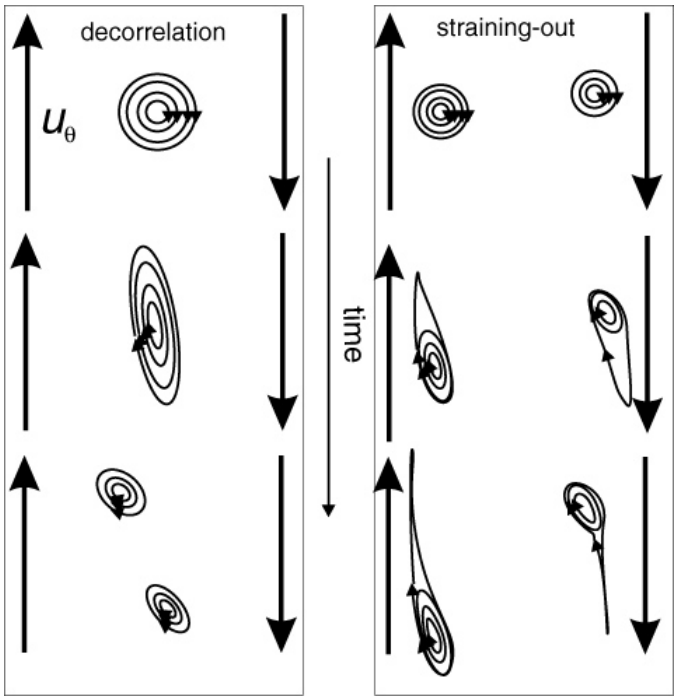


**Figure 1.8**: Sketches of the interaction between zonal flows and turbulence [SMR11]. Left: the decorrelation mechanism where larger eddies split up. Right: the straining-out mechanism where smaller eddies are taken over by the zonal flow.

In a torus, a second branch of the ZF appears due to the geodesic curvature of the magnetic field, which gives rise to density compressions as the plasma rotates poloidally with an azimuthally symmetric radially sheared poloidal velocity. These compressions can then relax via a sound wave which propagates along the magnetic field, giving rise to a finite frequency for this sheared flow with a frequency $c_s/R$ where $R$ denotes the major radius and $c_s$ is the sound speed. This finite frequency sheared flow is known as the geodesic acoustic mode (GAM), and also observed to affect turbulent transport [Bur06]

## 1.5 Density Limit in Tokamak

As shown in previous section, the fusion reaction rate scales with $n^2$. Moreover, at constant pressure, the fusion reaction is maximized at an optimum temperature of the order of 10 keV, so high density operation is desirable for magnetic confinement fusion. However, raising the line-averaged density, $\bar{n}_e$, to the Greenwald limit, $n_G\,[10^{20}\,\mathrm{m}^{-3}] = \frac{I_p[\mathrm{MA}]}{\pi a^2[\mathrm{m}^2]}$, usually leads to a significant reduction in confinement time, or even disruption, when $n_G$ is exceeded [Gre02, GTW$^+$88]. Since the discovery of this density limit, extensive experimental studies have shown that the Greenwald limit can be exceeded by increasing the core density while keeping the edge density low, i.e. by operating with peaked density profiles, using optimized fueling techniques [KHY$^+$91, LSB$^+$12, MOL$^+$02, VRC$^+$02]. These findings provide strong evidence linking the density limit to the edge physics [Gre02].

Among the phenomena in the plasma boundary region, edge cooling and radiation loss are found to be associated with the density limit, and have been widely investigated [Gre02, GTW$^+$88, SBF$^+$97, WGH$^+$89]. In radiation models [Gre02, CY02], the radiative heat loss due to increased impurity content in the plasma is thought to dominate the power balance at high densities, resulting in strong edge cooling and thus an increased resistivity, causing the toroidal current channel to shrink. The current shrinkage then leads to an increased current density gradient and the onset of resistive MHD instabilities. In particular, a thermo-resistive tearing mode model [GDA12, GDAW13, GBDA$^+$16], in which radiative cooling is balanced with the ohmic heating inside magnetic islands (figure 1.9), has been invoked to explain the dependence of the current density in the Greenwald limit scaling.

Although radiation models have achieved some success in explaining the empirical scaling, they do not address the mechanism that initiates edge cooling. One likely

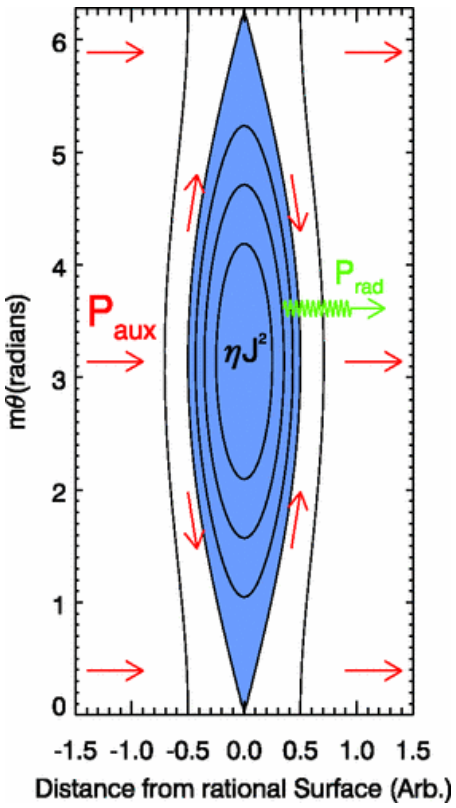


**Figure 1.9**: Sketch of a single lobe of a magnetic island [GDA12]. The radiative power balances the Ohmic heating power.

candidate is enhanced edge transport, i.e. turbulent particle and heat fluxes [Gre02]. We also note that enhanced particle transport has been observed in advance of any change in the MHD activity in both experiments and numerical simulations in high density plasmas [BYB$^+$91, RDZ98, LBG$^+$01, LHM$^+$05, SMM$^+$99]. At fixed pressure, the higher density usually implies reduced temperature and hence increases dissipative and resistive effects. These effects destabilize the resistive modes, which lead to enhanced fluctuation levels and turbulent transport [TD87]. Also, turbulent transport can be suppressed or mitigated by zonal flows that are in turn driven by the turbulence via the Reynolds force [DIIH05, Fuj09, TFM09, MRS09, XTD$^+$12, XTD$^+$11, SMR11, BRSS13]. This self-regulating process has been recognized as an important mechanism for the *L–H* transition that leads to the edge transport barrier and improved plasma confinement

[CTD+15, CTD+14, TXD+13, YMF+14, TCD+16]. However, zonal flows are subject to strong collisional damping in high density plasmas [DIIH05]. Weaker zonal flows cannot efficiently trigger the "tilt-stretch-absorption" process [MRS09, XTD+11], and therefore result in reduced Reynolds force. As a result, the self-regulation process is inhibited when the density limit is approached, and edge turbulent fluxes should increase. We suggest that the competition between collisionality triggered instabilities and the stabilizing effects of $\mathbf{E} \times \mathbf{B}$ shear flows may lead to the limit of edge density. Relevant results on this topic will be shown in Chapter 2.

## 1.6 Intrinsic Flow and Residue Stress

In addition to zonal flows, toroidal rotation (i.e. ion flows parallel to magnetic fields) and its radial shear can also improve plasma confinement in toroidally confined plasmas by stabilizing harmful MHD instabilities and mitigating turbulent transport. Unlike studies of zonal flows which have been intensively explored [Fuj09], the investigation on parallel flows (toroidal rotation) is still in progress. However, since the stabilization effect of toroidal rotation on resistive wall modes (RWMs) was clarified [TMA+07, BSB+10], the underlying physics of toroidal flows and momentum transport have been considered as an essential issue of the overall transport physics and have drawn more and more attention.

In the current generation of fusion devices, however, toroidal flows are usually provided by the external momentum input from neutral beam injection (NBI). In future reactor-grade devices, this may not be sufficient due to the large machine sizes, high densities and the limitations of beam current. For RWM stabilization in certain operational scenarios, it has been estimated that an Alfven Mach number $M_A = 0.02$ will be required, depending on the velocity profile and normalized pressure [LBGP04]. In a particular case

with $n_e = 6.7 \times 10^{19}\,\mathrm{m}^{-3}$ and $B_T = 5.2\,\mathrm{T}$, the threshold corresponds to a rotation speed of $200\,\mathrm{km\,s}^{-1}$, and it remains unclear whether this level of rotation can be generated from neutral beams.

One possible solution is to take advantage of intrinsic flows (spontaneous, self-generated in the absence of any external momentum input) that have been widely observed under a variety of operating conditions [RICd+07]. Empirical scalings (figure 1.10) show that, across the L-H transition, the increment in core toroidal velocity is proportional to the increment of the energy stored in the plasmas $\Delta W$ or in temperature gradient $\nabla T$ and is inversely proportional to the plasma current $I_p$, i.e.

$$\Delta V_\phi \propto \frac{\Delta W}{I_p} \text{ or } \propto \nabla T.$$

This scaling clearly indicates that the intrinsic flow is independent of the gradient of the toroidal momentum $\nabla V_\phi$.

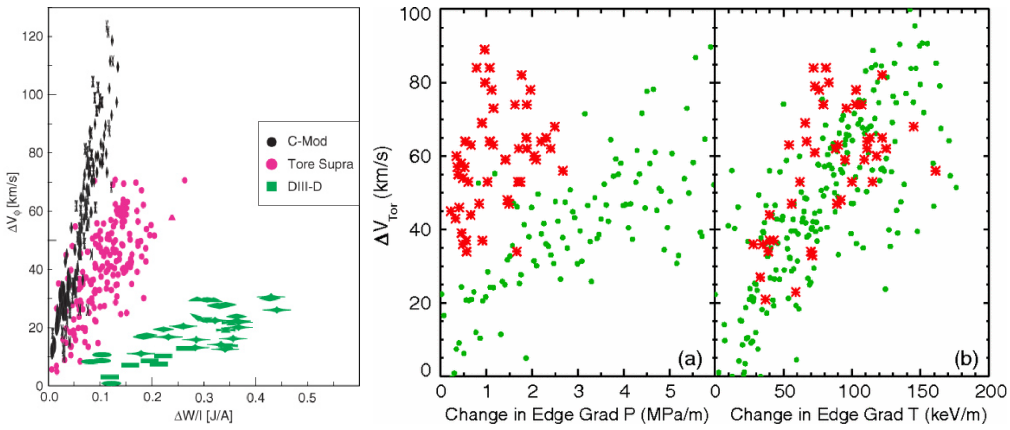


**Figure 1.10**: The toroidal velocity increment across the L-H transition. (Left) The velocity increment is proportional to the increment of the energy stored in the plasmas $\Delta W$ and is inversely proportional to the plasma current $I_p$ [RICd+07]. (Right) The velocity increment is proportional to $\nabla T$ [RHD+11].

From the theoretical point of view, the intrinsic flows are thought to be driven by off-diagonal terms in the transport matrix [DKG+13]. Without any external momentum

input, the velocity profile evolves basically through a balance between all sinks and the momentum flux gradient. The momentum flux is mainly determined by the Reynolds stress which is compromised of three terms [DMG+09]:

$$\Pi_{r\phi} = -\chi_\phi \partial_r V_\phi + V_{\rm p} V_\phi + \Pi^{\rm res},$$

where $\chi_\phi$ is the momentum diffusivity (viscosity), $V_{\rm p}$ is the momentum pinch velocity and $\Pi^{\rm res}$ is the residual stress. Note that residual stress is independent of both the toroidal velocity $V_\phi$ and its gradient $\partial_r V_\phi$, and can serve as a momentum source, with the intrinsic torque given by $-\nabla \cdot \Pi^{\rm res}$. The residual stress depends upon the underlying turbulence [DMG+09, DKG+13] and is a complicated function of the gradients of the density, temperature, pressure and current density profiles.

Evidence of the role of $\Pi^{\rm res}$ in driving intrinsic rotation has been gradually accumulated [Ric16]. Examination of the velocity profile evolution following a change from co- to counter-current NBI in JFT-2M plasmas demonstrated that there is a finite momentum flux even at zero momentum gradient and a finite offset velocity gradient even at zero momentum flux [IMM+95]. It was also shown that this off diagonal term in the momentum flux is proportional to the ion temperature gradient and inversely proportional to the plasma current. Further evidence came from observations of intrinsic rotation in C-Mod RF-heated plasmas [RGH+98] which demonstrated the origin at the plasma periphery [RLM+04] and scaling with the edge temperature gradient [RHD+11] inversely proportional to the plasma current [RBG+99]. More direct evidence from the measurements at the edge of the TEXTOR tokamak using multi-tip Langmuir and Mach probes [XHS+13], with counter-current NBI torque to balance the existing toroidal rotation, i.e. $V_\phi \approx 0$. Substantial residual stress and force have been observed at the plasma boundary, confirming the existence of a finite residual stress as a possible mechanism to

drive the intrinsic toroidal rotation. The results also show close correlation between the residual stress and the $E_r \times B$ shearing rate.

Although observations have qualitatively confirmed the role of $\Pi^{\text{res}}$ in driving intrinsic rotation, there are still many unresolved issues regarding intrinsic rotation and residual stress. One of them is the sign of the rotation. The direction of the intrinsic rotation is very sensitive to plasma parameters, such as turbulence type, confinement mode, and so on, switching its sign even with slight changes in plasma parameters [Ric16]. The other issue is that coupling between zonal flows and intrinsic toroidal flows. Since both of them are driven by ambient turbulence, their behaviors will definitely be affected by each other, increasing our difficulty in predicting the flow structures. It is fair to say that our understanding of the mechanism determining the direction and magnitude of intrinsic torque is still not enough to give a precise prediction.

## 1.7 Previous Studies of Shear Flows on CSDX

In addition to the toroidal magnetic confinement fusion devices, there are also many studies carried out on plasma devices with linear configurations, which have been widely utilized to investigate edge plasma physics and plasmaÃćÂĂÂŞmaterial interaction in magnetically confined fusion devices, because the linear devices are able to simulate scrape off layer (SOL) and divertor plasmas with open magnetic field configuration. The Controlled Shear Decorrelation Experiment (CSDX) [BTA$^+$05, TBC$^+$14] is a linear plasma device in University of California, San Diego. CSDX is a 2.8 m long linear helicon plasma device equipped with a 13.56 MHz half wave-length azimuthally symmetric (RF wave-fields have azimuthal mode number $m = 0$ and 1) helicon source with a radius $R_{\text{src}} = 7.5\,\text{cm}$, which typically produces a plasma with an on-axis density $n_e \approx 1 \times 10^{19}\,\text{m}^{-3}$ and on-axis electron temperature $T_e \approx 4 - 5$ eV. The typical operation

magnetic field is up to 2400 Gauss, and the injected RF power is 1.6kW (reflected power less than 20 W), and the neutral gas pressure is a few mTorr.

Although the parameters achieved in CSDX are quite different from those in fusion confinement experiments, the universal nature of the interaction between drift-wave turbulence and shear flows, make it possible to gain insight into the basic physics of drift turbulence and transport in such experiments. Here we highlight several key results from studies of drift turbulence and shear flows in CSDX.

### 1.7.1 Transition to drift turbulence

Detailed studies of the transition from coherent drift wave activity to broad-band drift turbulence have been carried out in CSDX [BTA$^+$05]. The development of broad drift wave spectra was studied using a Fourier transform based approach. The magnetic field strength is the control parameter. In the experiment, the transition from coherent drift waves to drift turbulence was studied as the magnetic field was increased. The gradual development of the spectra (figure 1.11) showed that linearly unstable drift wave eigenmodes were initially excited; these modes then began to interact via three-wave coupling process as determined by bicoherence analysis. Above a critical magnetic field of $\sim$ 700 G, a mode-locked (ML) spectrum developed; further increases in the magnetic field then led to the loss of the ML state and the emergence of much broader spectra.

### 1.7.2 Observations of turbulence-driven ZFs

One essential element of the nonlinear dynamics is that drift-wave turbulence can self-organized into sheared ZFs, which are linearly stable $\mathbf{E} \times \mathbf{B}$ drifts driven by the nonlinear transfer of energy from the drift waves into the ZFs. In CSDX, probe measurements confirmed the existence of a radially sheared azimuthal flow [HYJ$^+$06].

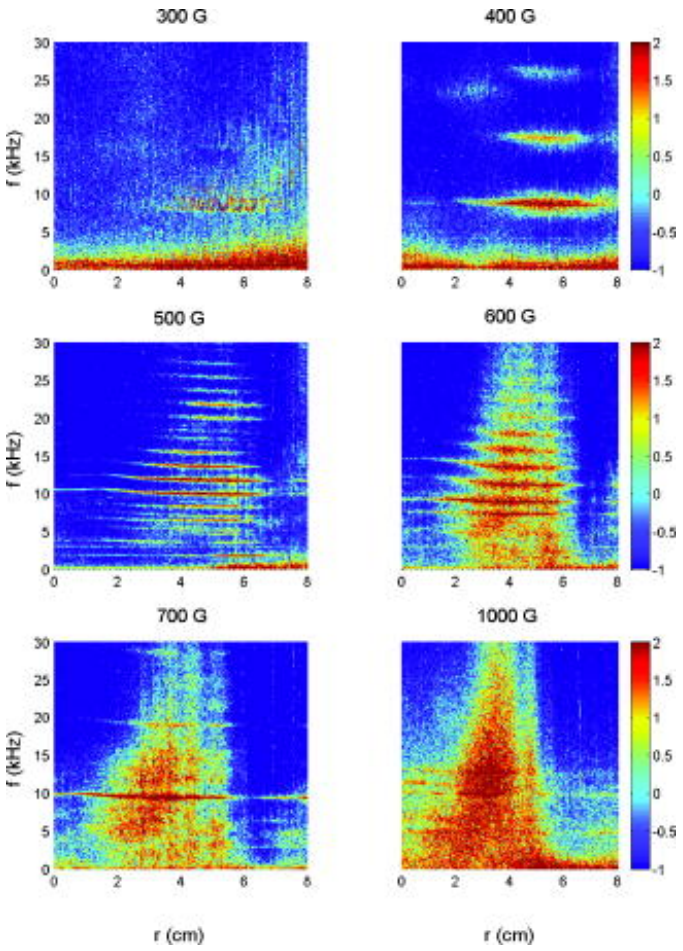


**Figure 1.11**: Evolution of the spatially resolved frequency spectrum as magnetic field is increased in a linear plasma device [BTA$^+$05].

The $m = 0$ nature of this flow has been observed by fast imaging techniques. The essential results are summarized in figure 1.12. This sheared flow was then shown to be consistent with a turbulent-driven ZF. A multi-tipped Langmuir probe array was used to measure the turbulent Reynolds stress in the experiment, and then this momentum flux was used in the turbulent momentum conservation equation along with an estimated collisional viscosity profile inferred from line-averaged ion temperature measurements. The results showed that the observed sheared flow was self-consistent with the turbulent Reynolds stress. A two-field numerical simulation of the drift turbulence was also performed, and showed the emergence of the shear flow during the development of the drift turbulence;

the simulation result was also consistent with the experimental observations.

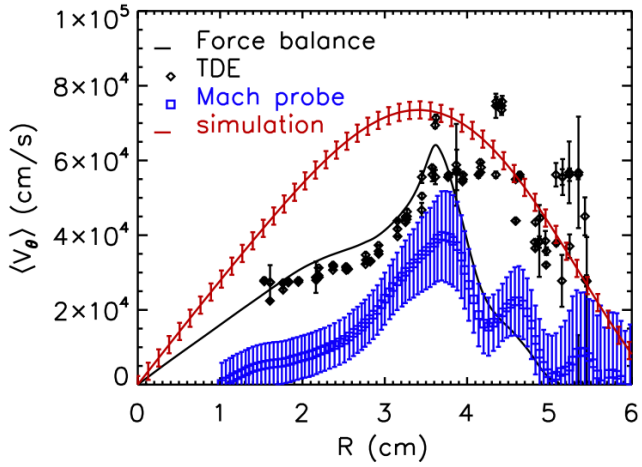


**Figure 1.12**: Radially sheared azimuthal flow velocity profile in CSDX [THY$^+$06].

### 1.7.3 Frequency resolved nonlinear energy transfer

Frequency-resolved nonlinear internal and kinetic energy transfer rates have been measured in CSDX [XTH$^+$09]. A 3-step Langmuir probe array was used to measure the time evolution of velocities and their gradients at fixed locations in the experiment. By using bi-spectral technique, the frequency-resolved nonlinear energy transfer rate were estimated, as shown in figure 1.13. The results clearly show strong nonlinear energy transfer activities among different scales. In addition, the net kinetic energy transfer results show that the zonal flows gain energy from small scale fluctuations, consistent with previous time-domain observations of turbulence-driven shear flows.

### 1.7.4 Intrinsic (azimuthal) rotation and residual stress

In CSDX it has long been observed that the mean azimuthal flow can be driven by the turbulent Reynolds stress, with peak value near the maximum density gradient. However, the underlying physics that determines the Reynolds stress remains unclear.

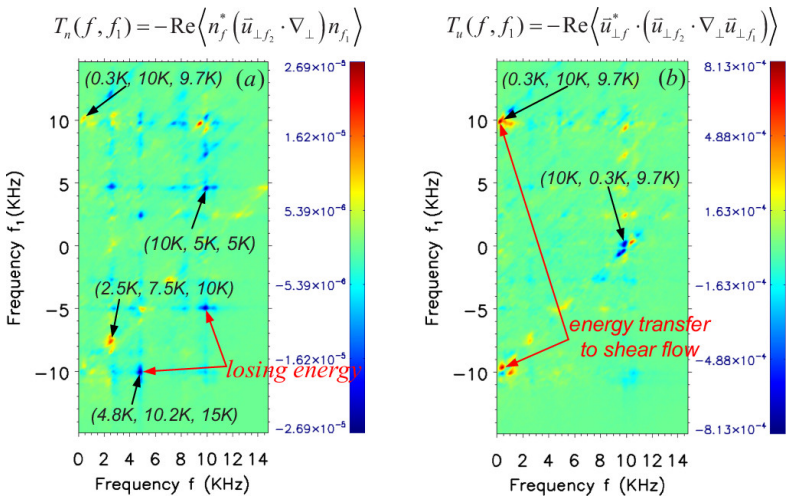


**Figure 1.13**: The experimentally measured nonlinear energy transfer rates [XTH+09]. (a) Internal energy transfer. (b) Kinetic energy transfer.

Recent experiments suggest an edge drive mechanism to explain the origin of the azimuthal stress in CSDX [YXD+10]. The experiment was based on the measurement of a non-diffusive turbulent momentum transport term, i.e. *residual stress* mentioned in last section. The Reynolds stress term, which is the total turbulent momentum transport, is written as

$$\Pi_{r\theta} = -\chi_\theta \partial_r V_\theta + V_\mathrm{p} V_\theta + \Pi^{\mathrm{res}},$$

where $\chi_\theta$ is the turbulent diffusivity, $V_\mathrm{p}$ is the pinch velocity, and $\Pi^{\mathrm{res}}$ is the residue stress. Due to the symmetry of the plasma in CSDX, the pinch term is estimated to be zero since it relies on the presence of trapped particles. The estimations show that the residual stress profile peaks at $r \approx 4\,\mathrm{cm}$ and provides the major torque for the mean azimuthal flow, as shown in figure 1.14(e). When combined with a no-slip boundary condition in the outer regions, due to strong flow damping by neutral gas in this region, this residue stress then gives rise to a net plasma fluid rotation in the observed direction.

In addition to intrinsic azimuthal rotation, we have also observed the axial flows increase as the magnetic field is raised. The phenomenon is associated with the growth of drift-wave turbulence and thus is related to the physics of intrinsic flows. A detailed

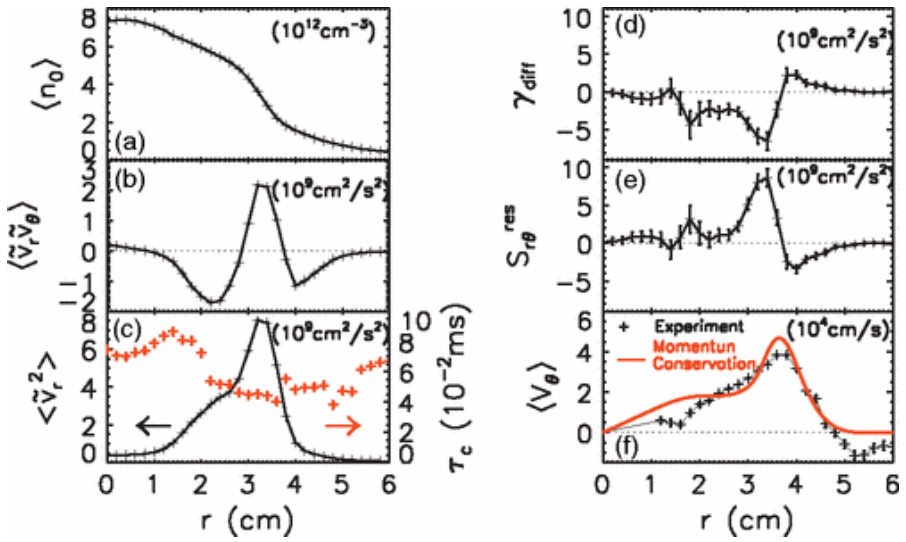


**Figure 1.14**: Radial profiles of (a) mean density, (b) measured total Reynolds Stress, (c) mean-squared radial turbulent velocity (black) and autocorrelation time (red), (d) diffusive momentum flux, (e) residual stress, and (f) mean azimuthal flow [YXD+10].

study of axial flows will be given in this thesis.

## 1.8 Thesis Outline

The main body of this dissertation consists of three topics which are presented in Chapter 2–4. In Chapter 5 we summarize the key results from Chapter 2–4, and suggest some possible topics for future work.

In Chapter 2, we study the evolution of edge sheared flows and their effects on regulating edge particle transport near the Greenwald limit in the HL-2A tokamak. It has long been suspected the enhanced edge particle flux is associated with collapsed edge sheared flows as the density limit is approached in tokamaks. Detailed equilibrium profiles as well as the turbulent particle flux and Reynolds stress across the separatrix are examined as $n_G$ is approached in ohmic L-mode discharges. As the normalized line-averaged density $\bar{n}_e/n_G$ is raised, the electron density and pressure gradient increase, and the electron temperature flattens. The shearing rate of the poloidal $\mathbf{E}\times\mathbf{B}$ and turbulent phase

velocities drop. Also, turbulent particle transport increases in high collisionality plasmas. The turbulent drive for the low-frequency zonal flow (the Reynolds power) collapses at higher $\bar{n}_e/n_G$ values, while the geodesic acoustic modes (GAMs) gain more energy in higher density plasmas. But the shearing rate of GAMs is less than low-frequency zonal flows, i.e. $\omega_{\mathrm{GAM}} \sim 0.3 \times \omega_{\mathrm{sh}}$, indicating that zonal flows play a leading role in turbulence suppression. Besides damping the edge shear flows through increased collisional dissipation, the increased collisionality can also be connected to an increased non-adiabatic electron response at high densities, which raises the cross-correlation between density and potential perturbations. Moreover, enhanced particle transport can be incorporated into radiation models to explain strong MHD instabilities and disruptions when the Greenwald limit is exceed.

Chapter 3 is focused on the generation of intrinsic axial flow in cylindrical plasmas without magnetic shear. The plasma flows and Reynolds stresses in both axial and azimuthal directions are simultaneously measured in a linear magnetized plasma device (CSDX) by using a combined Langmuir and Mach probe array. The axial flow shearing rate $V_z'$ and the axial Reynolds power $\mathcal{P}_z^{Re}$ track the rising density gradient as the B field is raised. The axial Reynolds stress is the dominant source driving the axial flow as the density gradient grows during the magnetic field scan. The joint probability density function of radial and axial velocity fluctuations, $\mathsf{P}\,(\tilde{v}_r, \tilde{v}_z)$, is highly tilted and anisotropic at higher magnetic field, indicating enhanced imbalance of the spectral correlator $\langle k_\theta k_z \rangle$ which can give rise to nonzero residual stress according to the dynamical symmetry breaking model. Furthermore, the axial velocity shear $V_z'$ and its turbulent drive $\mathcal{P}_z^{Re}$ rise with increasing azimuthal velocity shear $V_\theta'$ when $B < 800$ G; after 800 G, $V_\theta'$ and its turbulent drive collapse. Also, the direct energy exchange between axial and azimuthal flows is low, since the axial Reynolds power is about 10 times smaller than its azimuthal counterpart.

Chapter 4 is devoted to ICRF-induced plasma flows and potentials in the Alcator C-Mod tokamak. Gas-puff imaging techniques are employed to determine the far SOL region radial electric field and the plasma potential in ICRF heated discharges. The 2-dimensional velocity fields of the turbulent structures, which are advected by RF-induced $\mathbf{E} \times \mathbf{B}$ flows, are obtained via the time-delay estimation (TDE) techniques. Both the magnitude and radial extension of the radial electric field $E_r$ are observed to increase with the toroidal magnetic field strength $B_\varphi$ and the ICRF power. In particular, the RF-induced $E_r$ extends from the vicinity of the ICRF antenna to the separatrix when $B_\varphi = 7.9\,\mathrm{T}$ and $P_{\mathrm{ICRF}} \gtrsim 1\,\mathrm{MW}$. In addition, low-Z impurity seeding near the antenna is found to substantially reduce the sheath potential associated with ICRF power. The TDE techniques have also been used to estimate ICRF-induced potentials in different antenna configurations: (1) conventional toroidally-aligned (TA) antenna versus field-aligned (FA) antenna; (2) FA monopole versus FA dipole. It shows that FA and TA antennas produce similar magnitude of plasma potentials, and the FA monopole induced greater potential than the FA dipole phasing. The TDE estimations of RF-induced plasma potentials are consistent with previous results based on the poloidal phase velocity.

# Chapter 2

# Edge Shear Flows and Particle Transport near Greenwald Limit

As introduced in Chapter 1, the enhanced edge transport is supposed to be an important element that initiates edge cooling and thus leads to the enhanced particle transport and thus the density limit. Turbulent fluxes, as exhibited during the *L-H* transition, can be suppressed by strong shear flows via turbulence decorrelation. However, the shear flows are subject to substantial collisional damping effects in high density plasmas. As a result, damped shear flows cannot mitigate turbulent transport efficiently at higher density. Studies of turbulent transport in the scrape-off layer (SOL) as $\bar{n}_e$ is raised to the Greenwald limit have shown a pronounced increase in SOL turbulence intermittency [LBG$^+$01, LHM$^+$05], demonstrating that turbulent transport undergoes important changes as the density limit is approached. However, as of now, to our knowledge, the evolution of the turbulent particle and momentum fluxes, zonal flows and GAMs, and their interactions across the SOL, separatrix and edge plasma region have not been reported. We conducted a density scanning experiments on HL-2A to determine the evolution of edge shear flows when the Greenwald limit is approached.

## 2.1 Predator-Prey Model Summary

The zonal flow-turbulence interaction is usually describe by the predator-prey model [DIIH05]. In order to design experiments and diagnostic/data analysis schemes that could be used to directly measure the shear flows and turbulent stress, the predatorÃćÂĂÂŞprey model was then recast into a more primitive turbulent $K-\epsilon$ model [TXD$^+$13, TCD$^+$16] that expressed the evolution of the turbulent and ZF scale kinetic energy explicitly in terms of the underlying turbulent flow production rate that is mediated by the Reynolds power done by the turbulence on the sheared ZF. In a simplified form, these two energy scales evolve according to the model

$$\partial_t \tilde{K} = -\partial_r \tilde{T} - \mathcal{P} + (\gamma_{\text{eff}} - \gamma_{\text{dec}})\tilde{K}, \tag{2.1}$$

$$\partial_t \bar{K} = -\partial_r \bar{T} + \mathcal{P} - \nu_{\text{LF}} \bar{K}, \tag{2.2}$$

where the terms are given as

$$\begin{aligned}
&\bar{K} = \frac{1}{2}\langle v_\theta \rangle^2, \quad \tilde{K} = \frac{1}{2}\langle \tilde{v}_\theta^2 \rangle, \\
&\mathcal{P} = \langle \tilde{v}_r \tilde{v}_\theta \rangle \partial_r \langle v_\theta \rangle, \\
&\bar{T} = \langle \tilde{v}_r \tilde{v}_\theta \rangle \langle v_\theta \rangle, \quad \tilde{T} = \langle \tilde{v}_r \tilde{v}_\theta^2 \rangle, \\
&\langle v_\theta \rangle = \langle v_{\text{E}\times\text{B}} \rangle + \langle v_{\text{dia,i}} \rangle.
\end{aligned}$$

Here, $\tilde{K}$ and $\bar{K}$ denote the kinetic energy of turbulence and shear flow respectively, $\mathcal{P}$ denotes the nonlinear energy production of shear flow, $\tilde{T}$ and $\bar{T}$ denote the radial flux of of turbulent intensity and zonal flow intensity, $\gamma_{\text{eff}}$ is the growth rate of the underlying instabilities driving the turbulence, $\gamma_{\text{dec}}$ is the effective rate of turbulence decorrelation due to high-frequency dissipation effects, and $\nu_{\text{LF}}$ is the dissipation rate of low-frequency shear flow. Note that this model implicitly assumes a scale separation between turbulence

timescales and slower 'mean' quantities such as pressure gradient and ion diamagnetic flow $\langle v_{\mathrm{dia,i}} \rangle$.

According to this model, a quantity that characterizes the growth of shear flow energy $\bar{K}$ due to the nonlinear energy transfer of kinetic energy from turbulence is given as

$$\mathcal{P}_{\mathrm{Re}} = \mathcal{P} - \partial_r \bar{T} = -\langle v_\theta \rangle \partial_r \langle \tilde{v}_\theta \tilde{v}_r \rangle.$$

This quantity is called Reynolds power hereafter, which is the product of the shear flow velocity $\langle v_\theta \rangle$ and the Reynolds force $\mathcal{F}^{Re} = -\partial_r \langle \tilde{v}_r \tilde{v}_\theta \rangle$. Also, low-frequency flows decay at a rate $\nu_{\mathrm{LF}}$ due to collisional friction. It is expected that the zonal flows can diminished through two manners: (a) the collapsed turbulent stress which leads to lower nonlinear energy transfer into zonal flows $\mathcal{P}_{\mathrm{Re}}$ and (b) increased collision rate $\nu_{\mathrm{LF}}$ resulting in a stronger damping effect. Both effects can cause a reduction in zonal flow intensity, and thus decrease the shear decorrelation effects on turbulent transport, that is to decrease $\gamma_{\mathrm{dec}}$. With collapsed zonal flows, the enhanced particle flux can be expected. We carried out a density scanning experiment to see the effect of increased collisionality on zonal flows and the particle flux.

## 2.2 Experimental Arrangement

The experiment was carried out in the HL-2A tokamak [LDY$^+$05, DDD$^+$13, XTD$^+$12], which has a major radius of $R = 1.65\,\mathrm{m}$ and a minor radius of $a = 0.4\,\mathrm{m}$. In this study ohmic L-mode discharges were produced in the lower-single-null (LSN) geometry with the "favorable" $\nabla \mathbf{B} \times \mathbf{B}$ drift direction (toward the X-point). The plasma current was $I_p = 150\,\mathrm{kA}$, the toroidal magnetic field was $B_T = 1.3\,\mathrm{T}$, and the edge safety factor was about $3.5 - 4$. The Greenwald limit density was $n_G = I_p/\pi a^2 \approx 3.2 \times 10^{19}$ $\mathrm{m}^{-3}$ in these conditions. In this shot-by-shot density scanning experiment, the line-

averaged densities $\bar{n}_e$ measured by the HCN laser interferometer ramped from $0.8 \times 10^{19}$ to $2.8 \times 10^{19}$ m$^{-3}$ which correspond to a normalized density range of $0.25 - 0.9\, n_G$.

A multi-tip Langmuir probe array was used to investigate the edge turbulence and shear flows at the low-field-side (LFS) mid-plane of the tokamak [XTD+12]. The probe is composed of a $3 \times 5$ array of graphite tips, i.e. 5 steps with 3 tips on each step. The distance between two adjacent tips is 5 mm in the poloidal direction and 2.5 mm in the radial direction. Tips on the first, the third, and the fifth step were operated as triple probes, providing the electron density $n_e$ and temperature $T_e$, as well as the plasma potential $\phi_p = \phi_f + 2.8T_e$. Other tips were used to measure the floating potentials $\phi_f$. All probe data were sampled at 1 MHz using 12-bit digitizers. With this probe setup, we are also able to simultaneously measure the Reynolds stress, $-\langle \tilde{E}_r \tilde{E}_\theta \rangle / B^2$, and the turbulent particle flux, $\Gamma_r = \langle \tilde{n}_e \tilde{E}_\theta \rangle / B$, where $\tilde{E} = -\nabla \tilde{\phi}_f$.

## 2.3 Results

### 2.3.1 Equilibrium Profiles

Figure 2.1 shows the equilibrium profiles of the electron density $n_e$, electron temperature $T_e$, electron pressure $P_e = n_e T_e$, and radial electric field $E_r = -\partial_r \phi_p$ at three different normalized densities, i.e. $\bar{n}_e/n_G \approx 0.3$, 0.6 and 0.8. These profiles are obtained by taking the time average with 2 millisecond windows. As the normalized core density, $\bar{n}_e/n_G$, is raised from 0.3 to 0.8, the edge electron density increases by a factor of 3 at a position about 2 cm inside the separatrix, while the electron temperature drops from about 60 eV to 30 eV. Meanwhile, the electron pressure and its radial gradient increase with $\bar{n}_e/n_G$. The peak value of the radial electric field is reduced (figure 2.1(d)) due to the flattening of the plasma potential profiles at higher $\bar{n}_e/n_G$ values.

### 2.3.2 Kinetic Energy Transfer Analysis

The poloidal phase velocity of plasma fluctuations, $\langle v_\theta \rangle$ (figure 2.3(a)), can be inferred using the time-delay estimation (TDE) technique from two poloidally separated floating potential signals [XTD+12]. Here, a pair of 2 msec long time series are used to evaluate the local dispersion relations, i.e. conditional power spectra $S(k_\theta|f) = \frac{S(k_\theta,f)}{\sum_{k_\theta} S(k_\theta,f)}$ at each position (figure 2.2), introducing a spatial resolution of 1 mm (with a 50% overlap). This corresponds to the distance over which the probe tips move during the 2 msec window. The high-frequency fluctuations appear to propagate in the electron diamagnetic drift (EDD) direction inside the separatrix and propagate in the ion diamagnetic drift (IDD) direction in the SOL region. When $\bar{n}_e/n_G$ is raised, $\langle v_\theta \rangle$ decreases, particularly in the SOL region. In addition, as shown in figure 2.3(b), the turbulent Reynolds stress (with $\tilde{v}_\theta$ and $\tilde{v}_r$ in the frequency range of $20 < f < 100\,\mathrm{kHz}$), collapses at higher $\bar{n}_e/n_G$ values, leading to a reduced Reynolds force $\mathcal{F}_{Re} = -\partial_r \langle \tilde{v}_\theta \tilde{v}_r \rangle$. The Reynolds power $\mathcal{P}_{Re} = -\langle v_\theta \rangle \partial_r \langle \tilde{v}_\theta \tilde{v}_r \rangle$ (figure 2.3(c)) can also be calculated, and represents the nonlinear kinetic energy transferred from the turbulence into the shear flow. Note here that this quantity looks at the net transfer of kinetic energy from the 20-100 kHz turbulent fluctuations into the low-frequency poloidal velocity ($f < 0.5$ kHz). The peak value of the Reynolds power decreases significantly, when $\bar{n}_e/n_G$ is increased from 0.3 to 0.8, indicating a decline in the nonlinear energy transfer from the turbulence to the edge shear flow. The changes in turbulent Reynolds stress can be also seen in figure 2.4 that shows the joint probability density functions (PDFs) of radial and azimuthal velocities, $\mathbb{P}(\tilde{v}_r, \tilde{v}_\theta)$, at a position of $r - r_{\mathrm{sep}} = -2\,\mathrm{cm}$, at different normalized plasma densities. The tilting angle of the joint PDF decreases as $\bar{n}_e/n_G$ is raised, indicating a reduced anisotropy in the orientation of eddies.

Since the edge gradients provide free energy to the turbulence, it would be natural to seek the relation between relevant local gradients and the spatially averaged Reynolds

power, $\mathcal{P}_{Re}^{av} = \int \mathcal{P}_{Re}\, r dr / \int r dr$, where the integration is over $-1 < r - r_{\rm sep} < 1$ cm. Figure 2.5 shows the averaged Reynolds power as a function of edge gradients: (a) normalized electron pressure gradient, $L_{P_e}^{-1} = d_r \ln P_e$; (b) normalized density gradient $L_{n_e}^{-1} = d_r \ln n_e$; (c) normalized electron temperature gradient, $L_{T_e}^{-1} = d_r \ln T_e$; (d) mean shearing rate of poloidal velocity, $\omega_{\rm sh} \approx \left|\frac{\partial \langle v_\theta \rangle}{\partial r}\right|$. While it is not sensitive to the changes in the temperature gradient, $\mathcal{P}_{Re}^{av}$ decreases as $L_{n_e}^{-1}$ is increased, implying a suppression of the nonlinear energy transfer from the turbulence to the low-frequency shear flow at higher densities.

As shown in figure 2.6, the shearing rate of the poloidal flow $\omega_{\rm sh}$ decreases when the collision rate of either ions or electrons is raised. Here, electron and ion collision rates are spatially averaged over $-1 < r - r_{\rm sep} < 1$ cm. They are calculated respectively via $\nu_{\rm e} = 2.91 \times 10^{-6} n T_e^{-3/2} \ln\Lambda$ and $\nu_{\rm i} = 4.8 \times 10^{-8} Z^4 \mu^{-1/2} n T_i^{-3/2} \ln\Lambda$, with the approximation of $T_i \approx T_e$, where $Z$ is the charge number, $\mu$ is the ion mass number, and $\ln\Lambda$ is the Coulomb logarithm, which is 13.6 for electrons and 6.8 for ions. This phenomenon conforms to the prediction [LHL+99, DIIH05] that stronger Coulomb collisions damp zonal flows at higher collisionality. Correspondingly, the averaged Reynolds power $\mathcal{P}_{Re}^{av}$ decreases with increased collision rates (figure 2.7), indicating that the nonlinear energy transfer from the turbulence to the edge shear flow is reduced at higher density and collisionality.

The kinetic energy transfer between the edge turbulence and shear flows has also been investigated in the frequency domain. In the auto-spectra of perpendicular velocities $v_\perp(f)$ (figure 2.8(a)), at least two distinct flow patterns can be recognized, which are geodesic acoustic modes (GAMs) (centered at $f \approx 12$ kHz) and the turbulence ($f > 30$ kHz). These two patterns have been observed in previous experiments in this device [LLY+08, XTD+12, ZLD+06]. While there is no obvious changes in the spectra of turbulent velocities, the power contained in GAMs velocity fluctuations increases by a

factor of three as $\bar{n}_e/n_G$ is raised from 0.3 to 0.8.

The 2D frequency-resolved nonlinear energy transfer for $\bar{n}_e/n_G = 0.3$ and 0.8 are shown in figure 2.9, which are computed from 100 ensembles of time-stationary data taken roughly at $r - r_{\text{sep}} = -2\,\text{cm}$. A positive value (red) at $(f, f_1)$ suggests that the perpendicular velocity fluctuations associated with $f$ gain kinetic energy from fluctuations at $f_1$; a negative value (blue) suggests that the fluctuations at $f$ lose energy to those at $f_1$. As shown in figure 2.9, the GAMs (at $f \approx 12\,\text{kHz}$) gain energy from high-frequency fluctuations ($f \approx 40 - 100\,\text{kHz}$). Figure 2.8(b) shows the the net frequency-resolved nonlinear energy transfer rate [XTD$^+$12, XTH$^+$10], $\mathcal{T}_v(f) = -\,\text{Re}\sum_{f_1}\left\langle \mathbf{v}^*_{\perp,f}\cdot\left(\mathbf{v}_{\perp,f-f_1}\cdot\nabla_\perp\mathbf{v}_{\perp,f_1}\right)\right\rangle$, at different $\bar{n}_e/n_G$ values, which can be obtain by integrating over $f_1$ axis in the 2D nonlinear energy transfer map. The GAMs appear to gain more kinetic energy from the turbulent fluctuations when $\bar{n}_e/n_G$ is higher. By normalizing the energy transfer rate using auto-power of perpendicular velocity fluctuations, we can obtain the effective frequency-resolved nonlinear growth or damping rate (figure 2.8(c)), $\gamma_{\text{NL}}(f) = \mathcal{T}_v(f)/\langle\tilde{v}^2_\perp(f)\rangle$. As shown in figure 2.8(c), the effective nonlinear growth rate of GAMs, $\gamma^{\text{GAM}}_{\text{NL}}$, increased significantly as $\bar{n}_e/n_G$ is raised.

Meanwhile, the shearing rate of GAMs can be estimated using $\omega_{\text{GAM}} = \partial_r v_\theta(f = f_{\text{GAM}})$. As shown in figure 2.10, the mean value of $\omega_{\text{GAM}}$'s envelope increases from 7 to $10\times10^4\,\text{s}^{-1}$ when $\bar{n}_e/n_G$ increases from 0.3 to 0.8. Also, the eddy turn-over rate is estimated as $\omega_{\text{eddy}} = \tau^{-1}_{\text{eddy}} \sim \frac{\tilde{\phi}_f}{BL_rL_\theta} \sim 4.6 - 12\times10^4\,\text{s}^{-1}$, where $B = 1.3\,\text{T}$ is the toroidal field, and $\tilde{\phi}_f \sim 30 - 50\,\text{V}$ is the fluctuation amplitude of floating potentials, and $L_r \sim 1\,\text{cm}$ and $L_\theta \sim 3 - 5\,\text{cm}$ are respectively the turbulent eddy sizes in radial and poloidal directions [ZLD$^+$06, XTD$^+$12]. While the shearing rate of GAMs is comparable to the eddy turn-over rate at higher densities, i.e. $\omega_{\text{GAM}} \sim \omega_{\text{eddy}}$, it is still less than the mean flow shearing rate, i.e. $\omega_{\text{GAM}} \sim 0.3\times\omega_{\text{sh}}$. This indicates that, although GAMs are able to affect the turbulence saturation level and the turbulence dynamics, mean flow

plays the leading role in turbulence suppression.

### 2.3.3 Enhanced Particle Flux

Figure 2.11(a) shows the radial profiles of particle flux at three normalized core densities. The turbulent particle flux, $\Gamma_r = \langle \tilde{n}_e \tilde{v}_r \rangle$, increases substantially when $\bar{n}_e/n_G$ is raised from 0.3 to 0.8, in spite of the increase of GAMs amplitudes. The root-mean-square (RMS) of the density and radial velocity fluctuations ($20 < f < 100\,\mathrm{kHz}$) are shown in figure 2.11(b) and 2.11(c), respectively. While the variation in RMS of radial velocity fluctuations $|\tilde{v}_r|$ is negligible, the RMS of electron density fluctuations $|\tilde{n}_e|$ grows twofold as the core density is increased. The cross-phase at each position between $\tilde{n}_e$ and $\tilde{v}_r$ can be evaluated via $\varphi_{n_e,v_r}(f) = \arctan \dfrac{\mathrm{Im}\, S_{n_e,v_r}(f)}{\mathrm{Re}\, S_{n_e,v_r}(f)}$, where $S_{n_e,v_r}(f)$ is the cross-power spectra between $\tilde{n}_e$ and $\tilde{v}_r$. The cosine of the cross-phase indicates the cross-correlation between these two signals. By integrating over $20 < f < 100\,\mathrm{kHz}$, we can obtain the profile of the cross-correlation $\cos\varphi_{n_e,v_r}$ (figure 2.11(d)), which increases with $\bar{n}_e/n_G$ values inside the separatrix. Moreover, the cross-phase between density and floating potential fluctuations, $\varphi_{n_e,\phi}$ (figure 2.11(e)), also increases slightly as the plasma density is raised.

In figure 2.12 the averaged particle flux $\langle \Gamma_r \rangle$ inside the separatrix ($-2 < r - r_{\mathrm{sep}} < 0\,\mathrm{cm}$) is plotted as the function of edge gradients: (a) normalized pressure gradient $L_{P_e}^{-1}$; (b) normalized density gradient $L_{n_e}^{-1}$; (c) normalized electron temperature gradient $L_{T_e}^{-1}$ ; (d) mean shearing rate of poloidal velocity. While increasing with $L_{P_e}^{-1}$ and $L_{n_e}^{-1}$, the particle flux $\langle \Gamma_r \rangle$ decreases at higher $\omega_{\mathrm{sh}}$ which corresponds to lower density.

The $\langle \cos\varphi_{n_e,v_r} \rangle$ and normalized RMS of density fluctuations, $\langle \tilde{n}_e^2 \rangle^{\frac{1}{2}} / \langle n_e \rangle$, are compared against the four edge gradients respectively in figure 2.13 and 2.14. Both of them increase with $L_{P_e}^{-1}$ and $L_{n_e}^{-1}$, and drop at larger the mean shearing rate $\omega_{\mathrm{sh}}$. while the increase in $\langle \cos\varphi_{n_e,v_r} \rangle$ is about 40%, the $\langle \tilde{n}_e^2 \rangle^{\frac{1}{2}} / \langle n_e \rangle$ increases about 200%, showing

that the growth in density fluctuation amplitude plays a major role in enhanced particle transport.

## 2.4 Discussion

### 2.4.1 Reduced Shear Flows and Enhanced Particle Transport

In our measurements, the shearing rate of edge mean flows decreases at higher densities. The reduction in edge $\langle E_r \rangle$ shear, as $\bar{n}_e/n_G$ is raised, has also been reported by 3-dimensional fluid simulations of the plasma boundary regions [XNR$^+$03], in which the radial electric well broadens at higher densities. These findings agree with theoretical considerations [DIIH05] and numerical simulations [LHL$^+$99] that shear flows are subject to collisional damping effects.

It has been known that strong shear flows are able to tilt and stretch the turbulent eddies, creating the anisotropy to stimulate the Reynolds force that amplifies the zonal flows (ZFs) [DIIH05, MRS09, XTD$^+$11, SMR11]. This self-regulating process couples the energy of the turbulence to the zonal flow, reducing the amplitude of high-frequency fluctuations that drive turbulent transport. In this study, as the mean flow shear decreases at higher densities, the turbulent Reynolds stress is observed to flatten, leading to reduced Reynolds force and nonlinear energy transfer. The Reynolds force is also negligible in the SOL region. Meanwhile, the tilting angle of the joint PDF of radial and poloidal velocities $\mathbb{P}(\tilde{v}_r, \tilde{v}_\theta)$ decreases, implying that the eddy-tilting process is inhibited when the Greenwald limit is approached.

With the collapsed mean flow shear, enhanced particle transport is also observed. Noticeably, GAMs have greater effective nonlinear growth rate, $\gamma_{\mathrm{NL}}^{\mathrm{GAM}}$, and shearing rate, $\omega_{\mathrm{GAM}}$, at higher densities. $\omega_{\mathrm{GAM}}$ is comparable with the eddy turn-over rate $\omega_{\mathrm{eddy}}$, i.e. $\omega_{\mathrm{GAM}} \sim \omega_{\mathrm{eddy}}$, suggesting GAMs should be able to affect the turbulence

dynamics and saturation level. However, $\omega_{\mathrm{GAM}}$ is still less than mean shearing rate $\omega_{\mathrm{sh}}$, i.e. $\omega_{\mathrm{GAM}} \sim 0.3 \times \omega_{\mathrm{sh}}$. The turbulence suppression effect by GAMs is thus less efficient than mean flows.

Besides effects due to shear flows, particle transport can also be altered by the non-adiabatic electron response. The adiabatic parameter, $k_{\|}^2 v_{t,e}^2/\omega\nu_e$, is estimated to drop from about 2 to 0.3, as $\bar{n}_e/n_G$ is raised from 0.3 to 0.8, where $k_{\|} \sim 1/qR$ is the parallel wavenumber, $v_{t,e}$ is the electron thermal speed, $\nu_e$ is the electron collision rate, and $\omega$ is the dominant frequency of turbulence. Such significant change in the adiabatic parameter indicates a possible conversion from *adiabatic* drift waves to *non-adiabatic* resistivity driven modes, e.g. resistive ballooning modes, due to the increased collisionality [TD87, RDZ98, XNR$^+$03, LHM$^+$05]. These resistive modes have larger fluctuation levels and cross-phase between density and potential perturbations, and therefore produce larger cross-field particle flux and enhance edge cooling. All these processes and their interplay discussed above is summarized in figure 2.15.

In order to obtain steady edge profiles, we employed the shot-by-shot density scans in this study. However, a perturbative study using the density ramp-up or modulation would be necessary to resolve which is first affected by the increased collisionality, the collisional damping of shear flows or the collapse of the Reynolds force (turbulent vorticity flux).

### 2.4.2 Link the Enhanced Transport to Radiation Models

Although the enhanced edge transport can explain the decrease of plasma confinement in high collisionality plasmas, the discharges operated near the Greenwald limit are often terminated directly by strong MHD instabilities [Gre02, GTW$^+$88]. As shown in figure 2.16, the enhanced turbulent flux can be incorporated into a schematic of the conventional radiation models, especially the thermo-resistive tearing mode model

[GDA12, GBDA$^+$16] that gives the dependence on plasma current density. The enhanced particle transport will increase the convective heat flux, $\langle T_e \rangle \langle \tilde{n}_e \tilde{v}_r \rangle$, which dominates the heat loss in plasma boundary regions at higher plasma densities [LBG$^+$01], and thus result in strong edge cooling. The edge cooling can increase the resistivity and current density gradient. $\nabla J$ then drives tearing modes and hence increase radiation losses, which further decreases the edge temperature. This process iterates until the disruption occurs.

### 2.4.3 Different Behaviors of Zonal Flows and GAMs

The results shown in section 2.3.2 demonstrate that the low-frequency zonal flow gains less energy from the turbulence at higher densities, and its shearing rate decreases as well. Meanwhile, GAMs gain more energy and thus have higher effective growth rate $\gamma_{\rm NL}^{\rm GAM}$ at higher densities, even though the turbulence intensity does not change. Similar observations on GAMs have been reported in a recent investigation from JET [SHH$^+$16], in which GAMs amplitudes measured by Doppler backscattering increase as the line-averaged density is raised. The competition between ZFs and GAMs has also been observed in earlier experiments in HL-2A [XTD$^+$12] and Alcator C-Mod [CHH$^+$17]. In HL-2A's ECRH power scanning experiments, the amplitudes and effective nonlinear growth rates $\gamma_{\rm NL}$ of ZFs and GAMs were found to increase with the ECRH power, until the ZFs dominate the nonlinear energy transfer process when $P_{\rm ECRH} \geq 730\,{\rm kW}$ [XTD$^+$12]. Although some theoretical models [MD10a, MD11] have explored the different behaviors of low-frequency ZFs and GAMs, a detailed comparison between the theory and measurements is still lacking. The physics of the coupling between ZFs and GAMs as a function of the heating power and plasma density remains to be studied.

### 2.4.4 Potential Effect of Magnetic Stress

One topic that deserves further investigation is the effect of magnetic stress, $\langle \tilde{B}_\theta \tilde{B}_r \rangle$, on the driving force for zonal flows near the Greenwald limit. The divergence of the Maxwell stress is known to induce a force on plasmas. The signs of the divergences of the Reynolds stress and magnetic stress are opposite for the drift-Alfven waves [DIIH05, KG08], resulting in a lower driving force for the zonal flows in the limit of finite $\hat{\beta}$. As reported in both experiments [LHM$^+$05] and numerical simulations [RDZ98], electromagnetic fluid drift turbulence grows and becomes the dominant modes controlling edge transport when the density limit is approached.

In present study, the MHD ballooning parameter, $\alpha_{\mathrm{MHD}} = \frac{q^2 R}{L_{Pe}} \beta$ with $\beta = \frac{4\mu_0 P_{e0}}{B^2}$, increases from about 0.1 to 0.3 at the edge as $\bar{n}_e / n_G$ is raised from 0.3 to 0.8. Therefore, magnetic fluctuations are supposed to increase, and their effects on shear flows should be considered. Nonetheless, even without any direct measurement of electromagnetic effects, the reduction in turbulent force for the zonal flows at higher densities suggests that zonal flow is an important element in density limit physics. A probe array that is capable of measuring magnetic and Reynolds stresses has been developed. Direct magnetic stress measurements are in progress. We hope to report more results on this topic in the future.

## 2.5 Summary

Using a multi-tip Langmuir probe array, edge turbulent particle transport and shear flows have been investigated as the Greenwald limit is approached in the HL-2A tokamak. The results demonstrate that as the line-averaged density increases, the density gradient inside the separatrix increases sharply. The electron temperature profile and poloidal phase velocity of turbulent fluctuations drop as the density increases toward the Greenwald limit. Meanwhile, the low-frequency zonal flow shear and its turbulent drive

(Reynolds power) are observed to decrease in high collisionality discharges. Therefore, ZFs cannot regulate turbulent transport. The frequency-resolved nonlinear energy transfer analysis shows that GAMs have larger effective nonlinear growth rate $\gamma_{\mathrm{NL}}^{\mathrm{GAM}}$ at higher $\bar{n}_e/n_G$ values. However, $\omega_{\mathrm{GAM}}$ is still less than the shearing rate of mean flows by a factor of $3-5$. Furthermore, the increase of the cross-correlation between $\tilde{n}_e$ and $\tilde{v}_r$, as well as the amplitude of $\tilde{n}_e$, results in substantial enhancement of particle transport in high collisionality plasmas, increasing edge cooling and therefore driving the strong MHD instabilities that lead to disruptions. The adiabatic parameter, $k_{\parallel}^2 v_{t,e}^2/\omega\nu_e$, drops significantly from about 3 to 0.5 as $\bar{n}_e/n_G$ increases from 0.3 to 0.8. These findings suggest that the increased collisionality may not only damp the low-frequency zonal flow via Coulomb collisions, but also increase the non-adiabatic electron response and hence increase particle transport.

In addition to the poloidal shear flows discussed in present study, the toroidal shear flows can play an important role in mitigating instabilities and improving the plasma confinement. Accordingly, the dynamics of toroidal shear flows and their coupling with poloidal flows in high collisionality plasmas may deserve further explorations.

# Acknowledgments

Chapter 2, in part, has been submitted for publication of the material as it may appear in Nuclear Fusion, 2017, R Hong, G R Tynan, P H Diamond, L Nie, D Guo, L Ting, R Ke, Y Wu, B Yuan, and M Xu. Copyright IOP Publishing, 2017. The dissertation author was the primary investigator and author of this paper.

This work is supported by the Chinese National Fusion Project for ITER under Grant No 2013GB107001, the National Natural Science Foundation of China under Grant Nos 11375053 and 11575055, and the International S&T Cooperation Program of China

under Grant No 2015DFA61760.

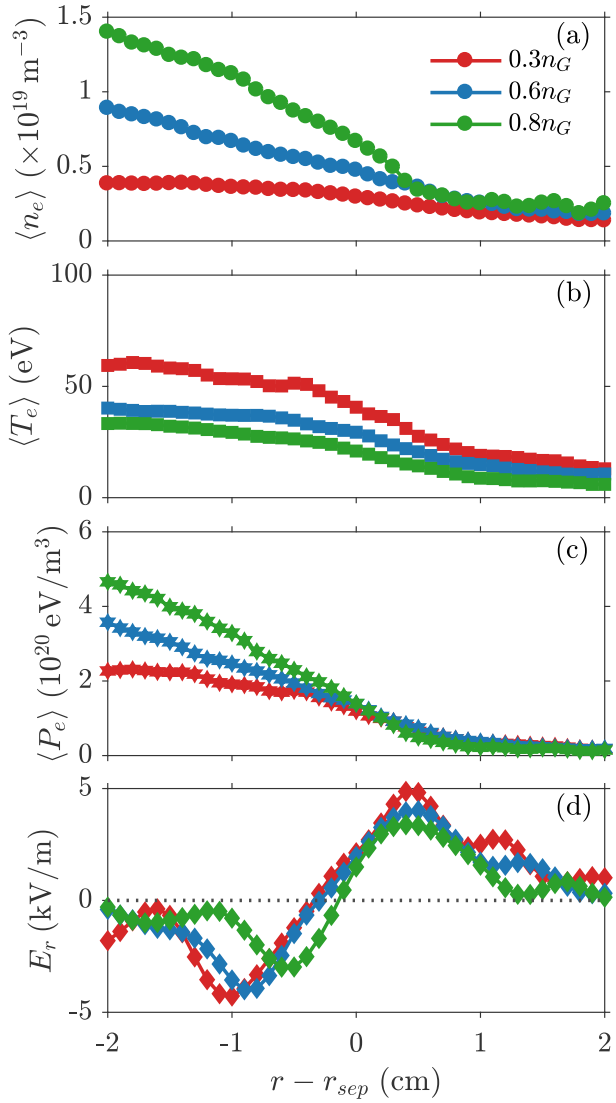


**Figure 2.1**: Equilibrium profiles of the electron density (a), electron temperature (b), electron pressure (c) and radial electric field (d), at three normalized line-averaged densities $\bar{n}_e$.

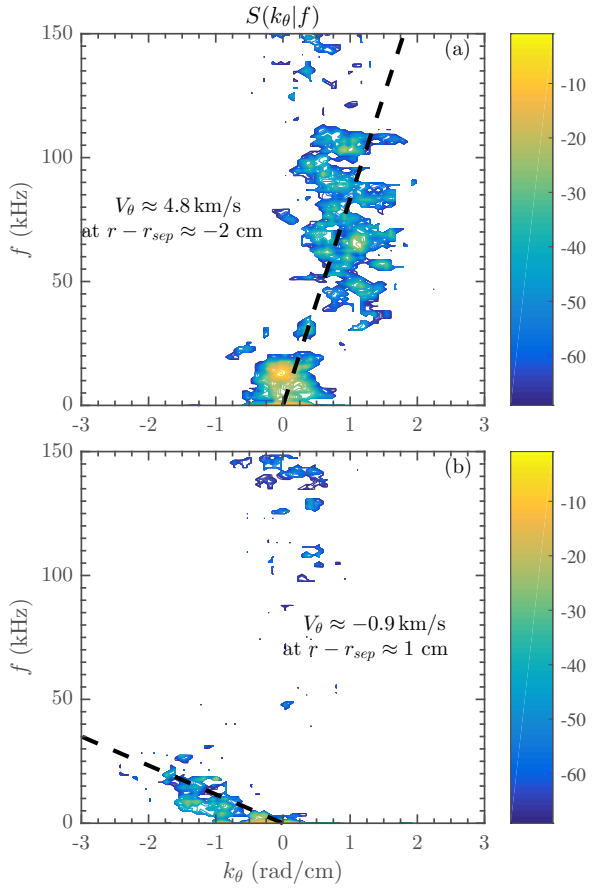


**Figure 2.2**: A typical conditional spectra $S(k_\theta|f)$ at $r - r_{\mathrm{sep}} \approx -2\,\mathrm{cm}$ (a) and 1 cm (b), when $\bar{n}_e/n_G \approx 0.6$. Black dash lines imply the local dispersion relations. The positive $k_\theta$ is in electron diamagnetic drift (EDD) direction and negative in ion diamagnetic drift (IDD) direction.

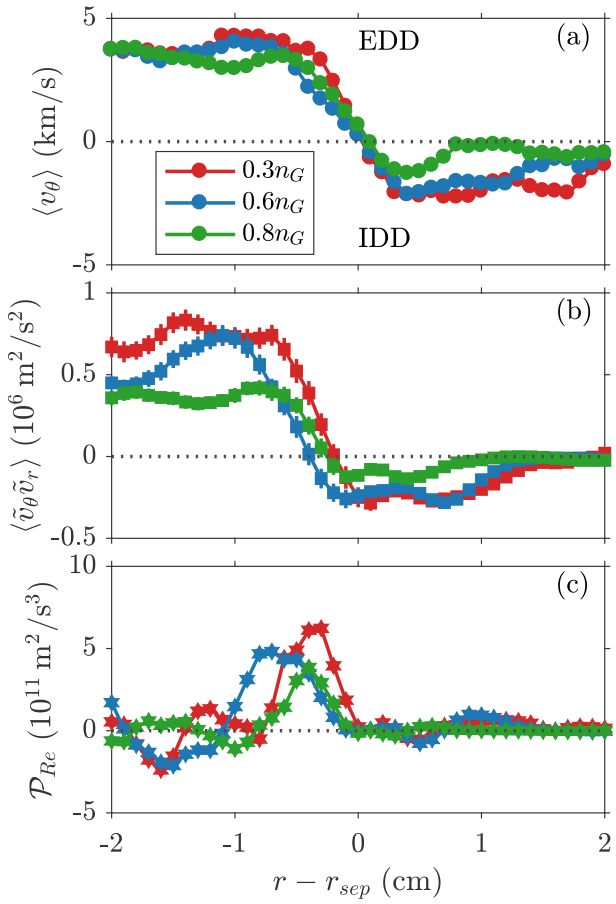


**Figure 2.3**: Profiles of the poloidal phase velocity $\langle v_\theta \rangle$ (a), turbulent Reynolds stress $\langle \tilde{v}_\theta \tilde{v}_r \rangle$ (b) and Reynolds power $\mathcal{P}_{Re} = -\langle v_\theta \rangle \partial_r \langle \tilde{v}_\theta \tilde{v}_r \rangle$ (c), at three normalized line-averaged densities $\bar{n}_e/n_G$. The positive $\langle v_\theta \rangle$ is in electron diamagnetic drift (EDD) direction and negative $\langle v_\theta \rangle$ in ion diamagnetic drift (IDD) direction.

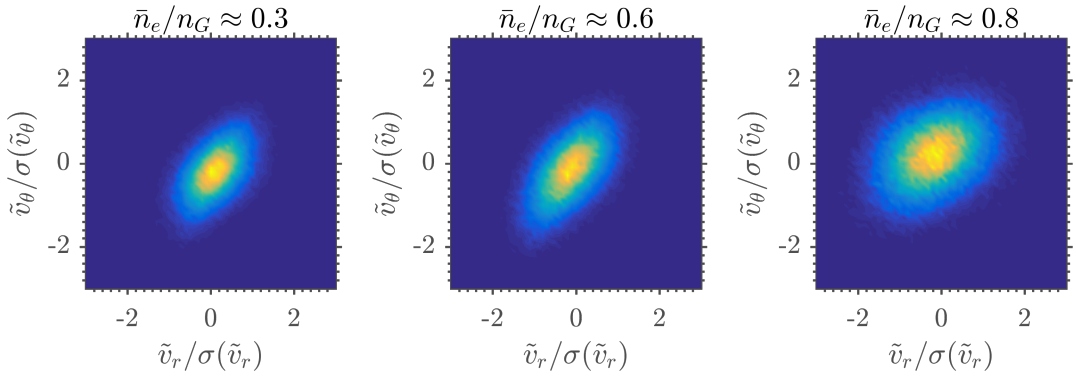


**Figure 2.4**: Joint PDF of radial and azimuthal velocities, $\mathbb{P}(\tilde{v}_r, \tilde{v}_\theta)$, at $r - r_{\text{sep}} = -2\,\text{cm}$ at three densities. Velocities are normalized by their standard deviations.

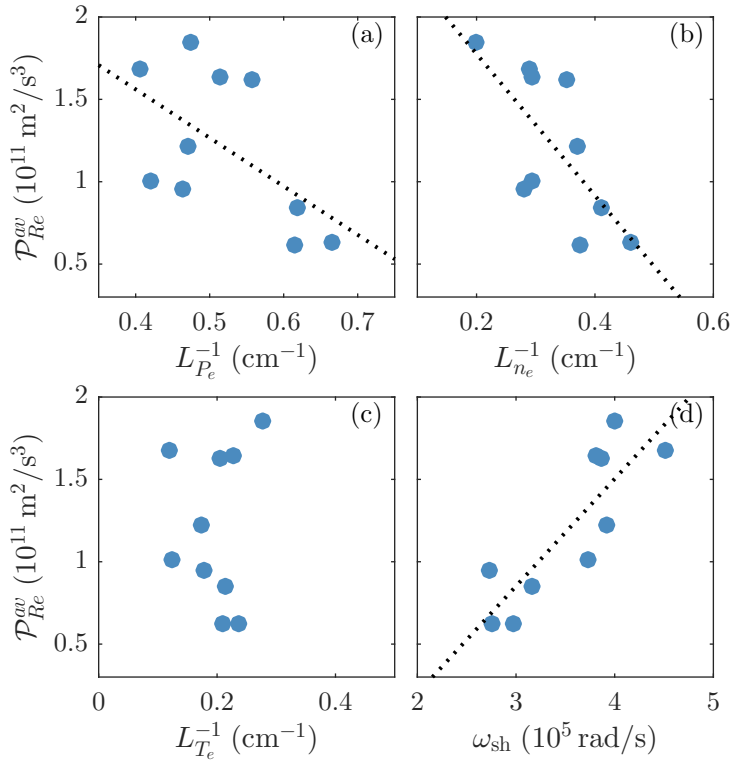


**Figure 2.5**: Averaged Reynolds powers, $\mathcal{P}_{Re}^{av} = \int \mathcal{P}_{Re}\, r dr / \int r dr$ where $-1 < r - r_{\mathrm{sep}} < 1$ cm, compare against the normalized pressure gradient $L_{P_e}^{-1}$ (a), the normalized density gradient $L_{n_e}^{-1}$ (b), the normalized electron temperature gradient $L_{T_e}^{-1}$ (c), and the shearing rate of poloidal velocity (d). Black dotted lines imply the linear trends.

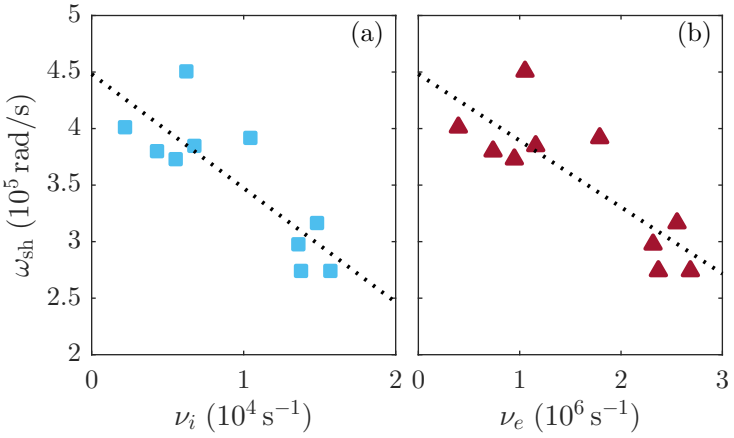


**Figure 2.6**: The flow shearing rate, $\omega_{\mathrm{sh}}$, compares against the ion collision rate $\nu_{\mathrm{i}}$ (a) and the electron collision rate $\nu_{\mathrm{e}}$ (b). Black dotted lines imply the linear trends.

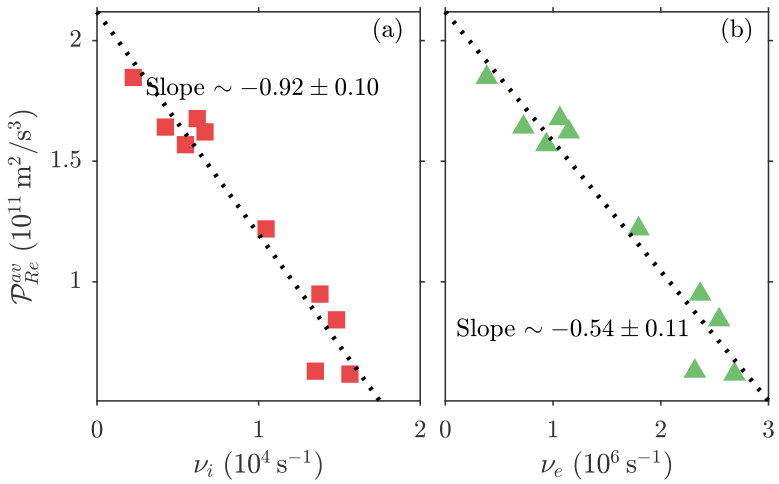


**Figure 2.7**: The averaged Reynolds power, $\mathcal{P}_{Re}^{av}$, compares against the ion collision rate $\nu_\mathrm{i}$ (a) and electron collision rate $\nu_\mathrm{e}$ (b). Black dotted lines imply the linear trends.

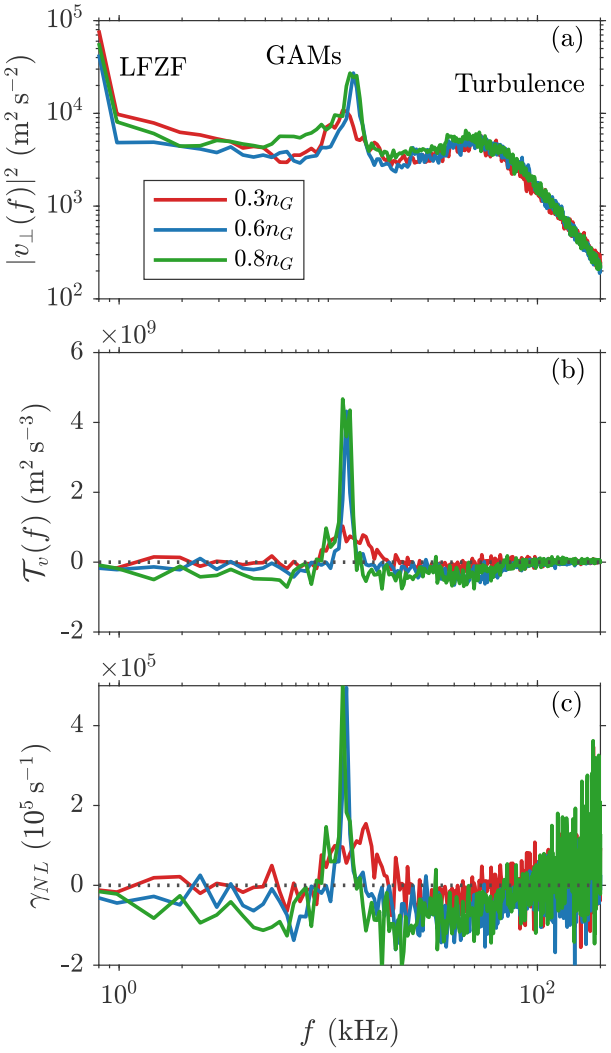


**Figure 2.8**: Auto-spectra of perpendicular velocity fluctuations (a), the nonlinear kinetic energy transfer rate $\mathcal{T}_v(f)$ (b), and the effective growth rate due to energy transfer $\gamma_{\mathrm{NL}} = \mathcal{T}_v(f)/\langle\tilde{v}_\perp^2(f)\rangle$ (c), at three normalized densities $\bar{n}_e/n_G$, at a position of $r - r_{\mathrm{sep}} \approx -2\,\mathrm{cm}$.

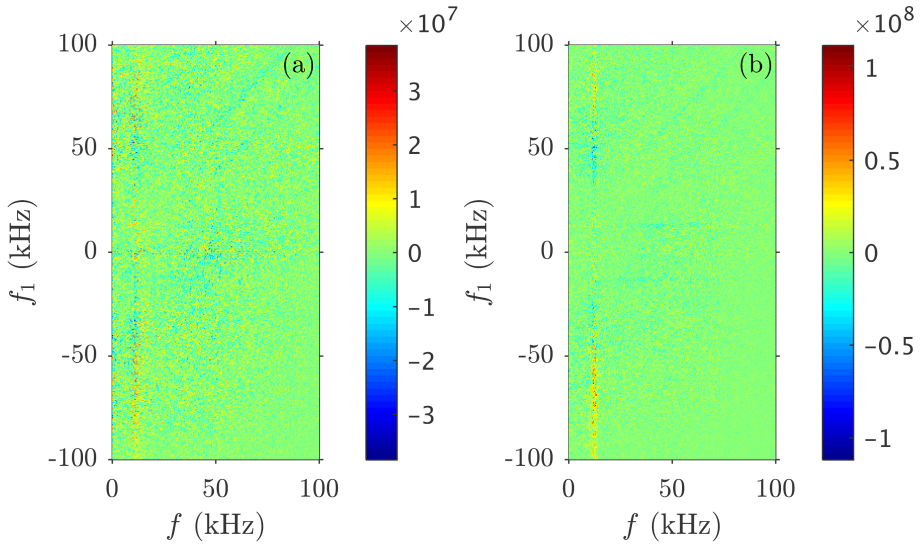


**Figure 2.9**: 2D nonlinear kinetic energy transfer for $\bar{n}_e/n_G \approx 0.3$ (left) and 0.8 (right). A positive value (red) at $(f, f_1)$ means that the perpendicular velocity fluctuations, $v_\perp$, associated with $f$ gain kinetic energy from those at $f_1$; a negative value (blue) means $v_\perp$ at $f$ lose energy to those at $f_1$.

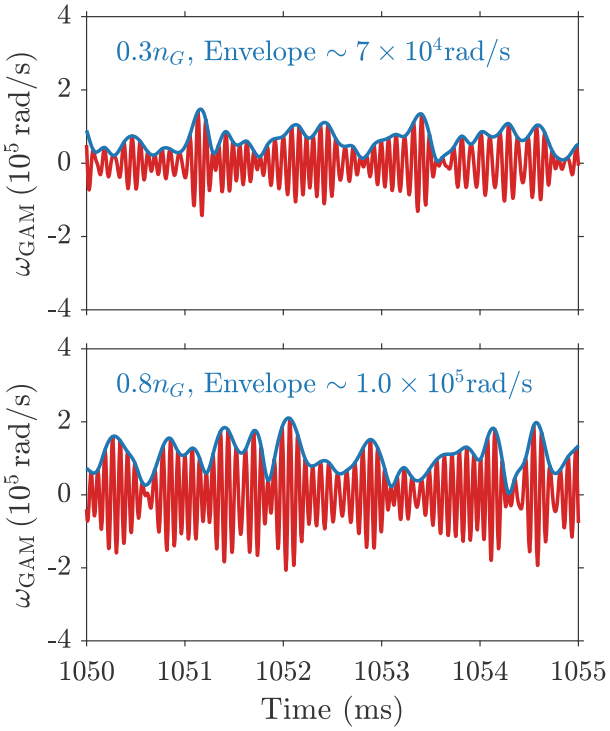


**Figure 2.10**: The shearing rate of GAMs, $\omega_{\mathrm{GAM}}$, for $\bar{n}_e/n_G \approx 0.3$ (left) and 0.8 (right). Blue curves indicate envelopes of $\omega_{\mathrm{GAM}}$. The mean values of envelops are $\sim 7 \times 10^4$ rad/s for $\bar{n}_e/n_G \approx 0.3$ and $\sim 10 \times 10^4$ rad/s for $\bar{n}_e/n_G \approx 0.8$.

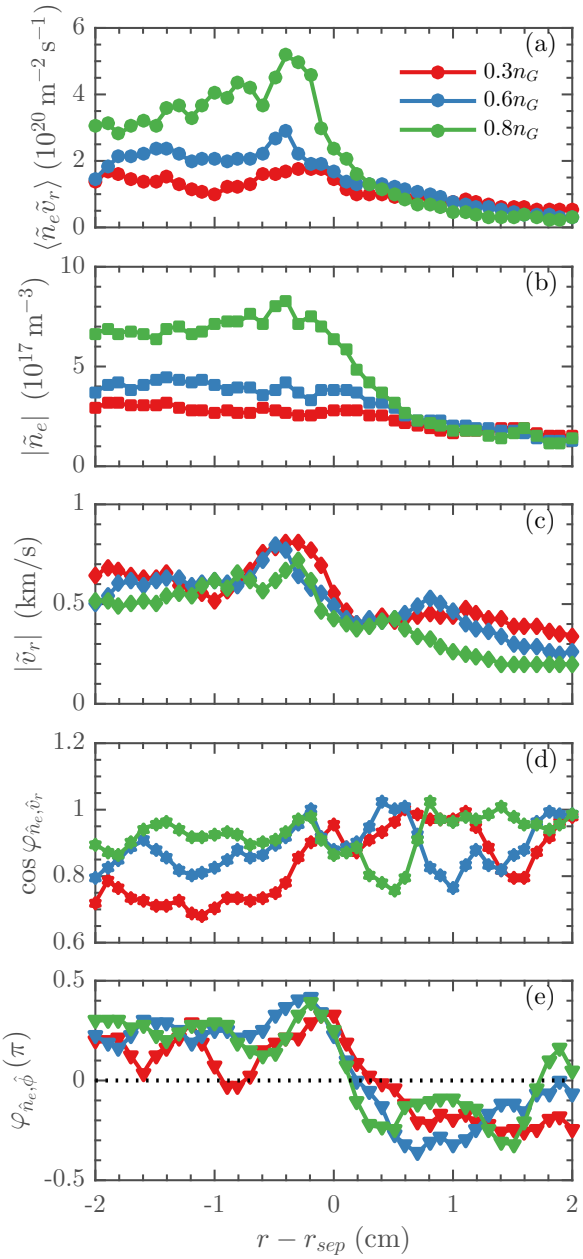


**Figure 2.11**: Radial profiles of electron particle flux (a), RMS of electron density fluctuations (b), RMS of radial velocity fluctuations (c), cross-correlation between velocity and density fluctuations (d), and cross-phase between density and floating potential perturbations (e).

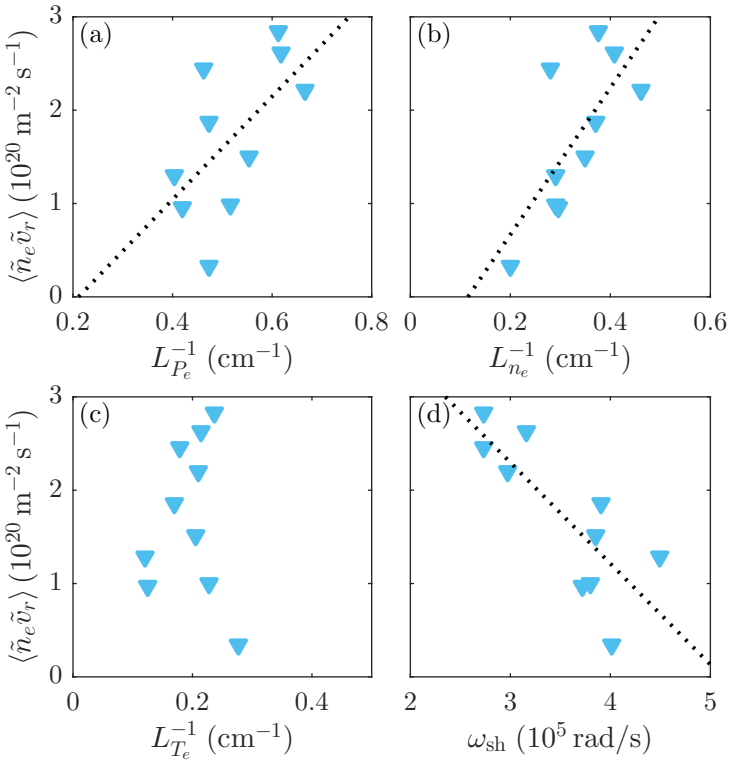


**Figure 2.12**: Averaged particle flux, $\langle \tilde{n}_e \tilde{v}_r \rangle$, inside the separatrix compares against normalized pressure gradient $L_{P_e}^{-1}$ (a), normalized density gradient $L_{n_e}^{-1}$ (b), normalized electron temperature gradient $L_{T_e}^{-1}$ (c), and mean shearing rate of poloidal velocity (d). Black dotted lines imply the linear trends.

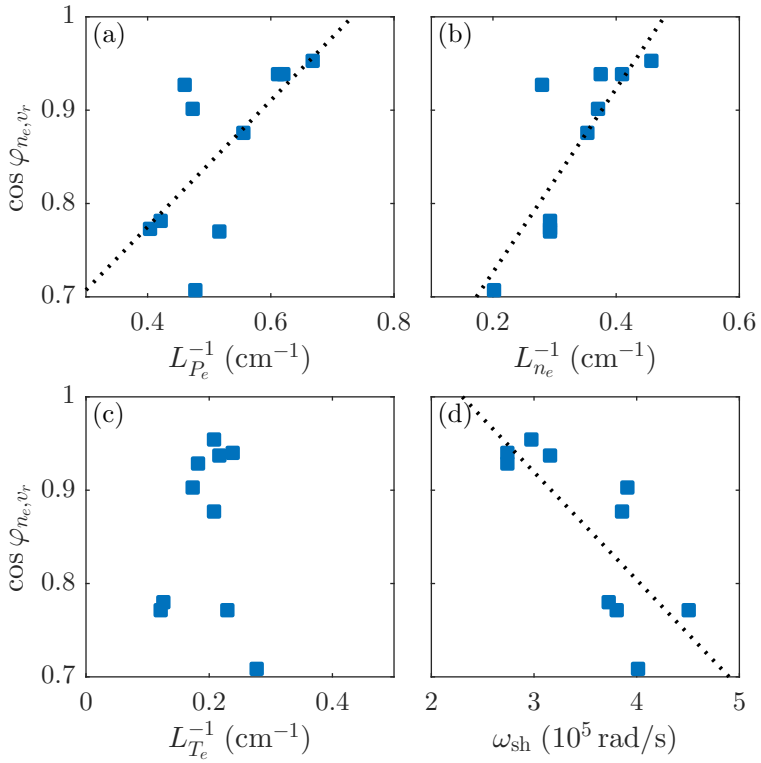


**Figure 2.13**: The averaged cross-correlation, $\langle \cos \varphi_{n_e,v_r} \rangle$, compares against normalized pressure gradient $L_{P_e}^{-1}$ (a), normalized density gradient $L_{n_e}^{-1}$ (b), normalized electron temperature gradient $L_{T_e}^{-1}$ (c), and mean shearing rate of poloidal velocity (d). Black dotted lines imply the linear trends.

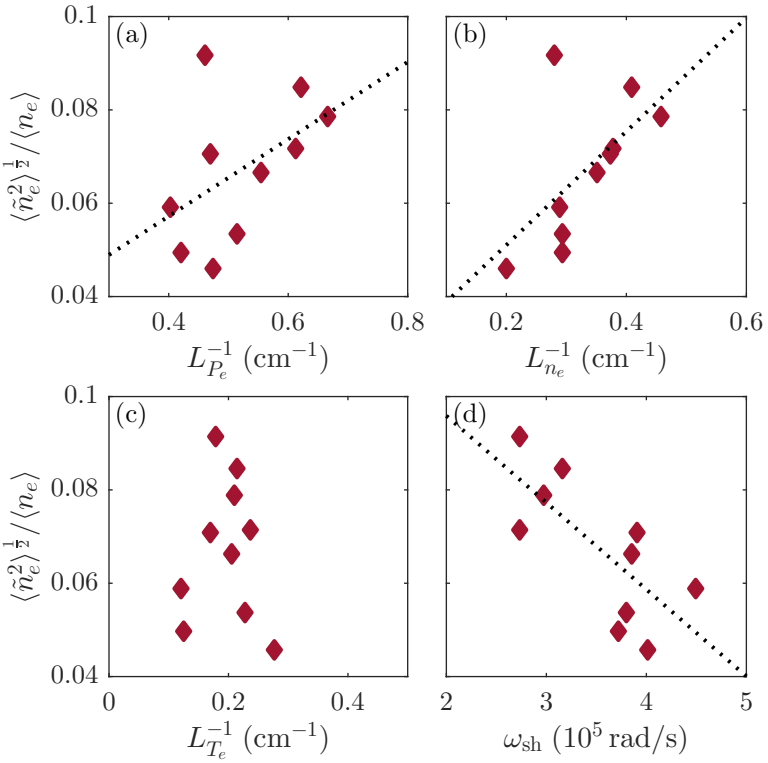


**Figure 2.14**: The normalized RMS of density fluctuations, $\langle \tilde{n}_e^2 \rangle^{\frac{1}{2}} / \langle n_e \rangle$, compares against normalized pressure gradient $L_{P_e}^{-1}$ (a), normalized density gradient $L_{n_e}^{-1}$ (b), normalized electron temperature gradient $L_{T_e}^{-1}$ (c), and mean shearing rate of poloidal velocity (d). Black dotted lines imply the linear trends.

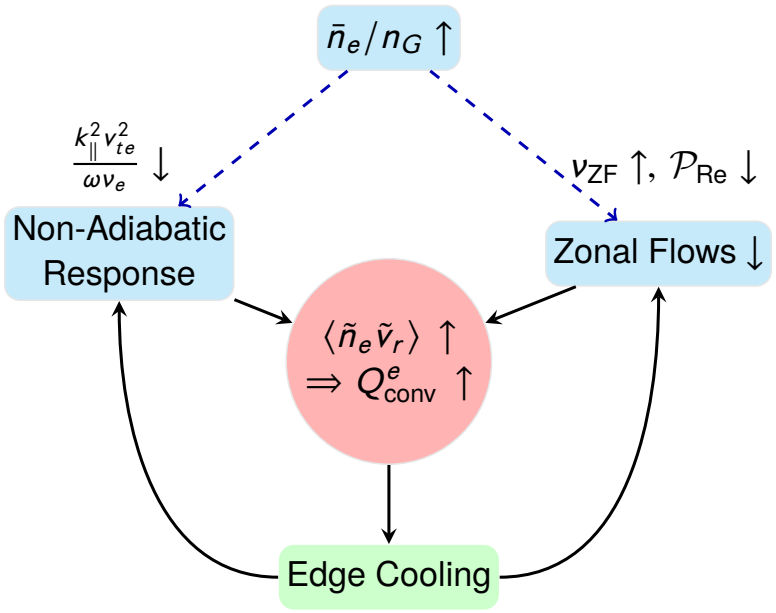


**Figure 2.15**: Sketch of a possible feedback mechanism in high collisionality plasmas. The increased collisionality increases the collisional dissipation of zonal flows, and enhances the correlation between $\tilde{n}_e$ and $\tilde{v}_r$. Both effects can further enhance turbulent particle flux and edge cooling.

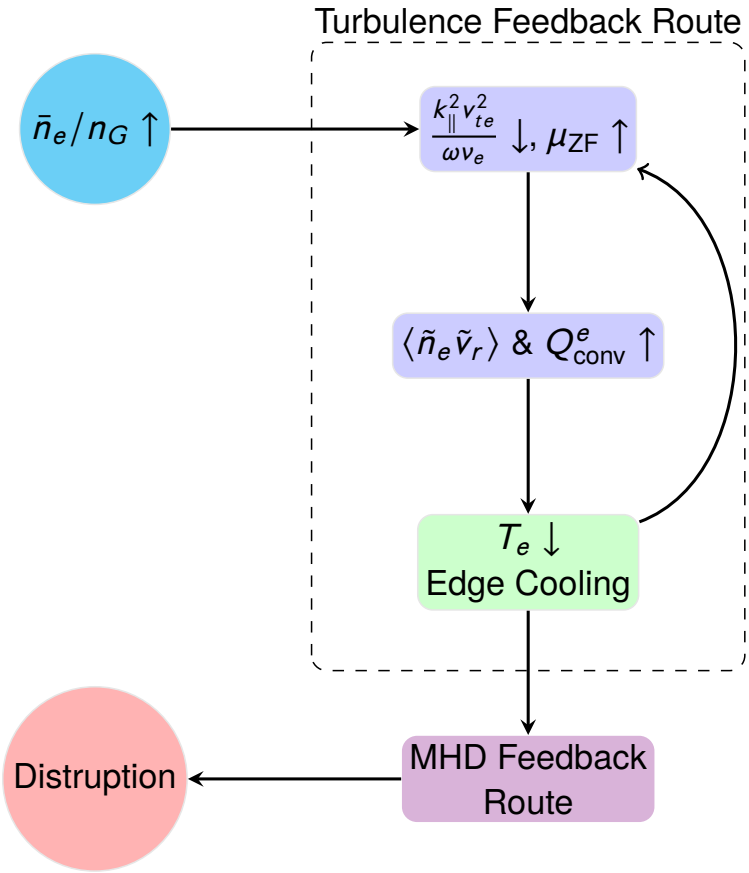


**Figure 2.16**: Schematic of a possible mechanism, which combines the enhanced turbulent transport with MHD radiation models, for disruptions in density limit.

# Chapter 3

# Intrinsic Axial Flow and Secondary Flow Coupling

As mentioned in last chapter, the intrinsic parallel flow (aka toroidal rotation in tokamak) can be driven by the underlying turbulence and thus affect the flow dynamics in plasmas. To study the generation of intrinsic parallel flows, we carried out experiments in a linear magnetized device, CSDX, using a combined Langmuir and Mach probe array.

## 3.1 Introduction

Plasma flows along the magnetic field lines play a vital role in the stabilization of plasma instabilities and the development of transport barriers [GSJ$^+$02, RGJ$^+$07, RICd$^+$07, dRB$^+$07, DKG$^+$13, IR14, Ric16]. In most existing magnetic confinement fusion devices, the parallel flow or toroidal rotation is directly driven by external momentum sources such as neutral beam injection (NBI). However, in large scale devices like ITER, the NBI driven rotation will be inadequate due to the limited neutral beam penetration in high density plasmas. In order to optimize and improve the confinement regimes in ITER

and beyond, therefore, it is important to uncover alternative mechanisms that can drive sufficient parallel plasma flows.

A phenomenon called intrinsic flow has been identified in magnetically confined plasmas [SBd$^+$07, dRB$^+$07, MBB$^+$11, RHD$^+$11, DKG$^+$13, IR14, Ric16], in which the plasma rotates without any input of toroidal momentum. This intrinsic flow can be large [RICd$^+$07, MBB$^+$11, Ric16], and thus there is strong interest in knowing whether there is sufficient toroidal torque in future fusion devices to affect confinement and MHD stability. Empirical results show that intrinsic torque in H-mode plasmas scales with the plasma stored energy over the plasma current (ÃćÂĂÂIJRice scalingÃćÂĂÂİ) [RICd$^+$07]. Further measurements from C-Mod reveal that the intrinsic torque is proportional to the edge temperature gradient [RHD$^+$11]. In addition, probe measurements from the plasma boundary region of TJ-II stellarator [GHP$^+$06] and TEXTOR tokamak [XHS$^+$13] confirm the existence of significant turbulent drive for the parallel shear flow when large edge $E_r \times B$ shear flows are triggered.

These experimental observations suggest that intrinsic flows can be driven by the residual turbulent stress which emerges from the non-diffusive part of the parallel Reynolds stress $\langle \tilde{v}_r \tilde{v}_z \rangle$ and depends on the underlying turbulence driven by the gradients of various plasma profiles. A number of theoretical models based on symmetry breaking in $k-$space have been proposed to explain the development of the residual stress [DKG$^+$13]. In these models the residual stress is determined by the correlator, $\langle k_z k_\theta \rangle = \sum_{\mathbf{k}} k_z k_\theta \left|\hat{\phi}_{\mathbf{k}}\right|^2 / \sum_{\mathbf{k}} \left|\hat{\phi}_{\mathbf{k}}\right|^2$, which is effectively set by the spatial structure of the $k$-spectrum $\left|\hat{\phi}_{\mathbf{k}}(r)\right|^2$. Theory suggests that the asymmetry can result from the spatial variation of fluctuation intensity profiles [GDH$^+$10], or can be induced by the sheared $E_r \times B$ flow that shifts modes off resonant surfaces [GDHS07]. These mechanisms indicate that the residual stress is positively related to $E_r \times B$ flow shear and turbulent intensity gradient, i.e. $\Pi_{rz}^{\mathrm{Res}} \sim V_E'$ and $\Pi_{rz}^{\mathrm{Res}} \sim I'$, respectively. The predicted model

scaling was consistent with direct measurements of the residual stress in TEXTOR [XHS+13].

Although this symmetry breaking mechanism was able to explain the development of the residual stress in that earlier work, those conventional models require finite magnetic shear, and hence encounter difficulty when they are applied to plasmas with zero or weak magnetic shear. Moreover, C-Mod experiments indicates that intrinsic flow is more sensitive to the magnitude of the central safety factor $q_0$ rather than the magnetic shear [RPR+13]. Furthermore, turbulence-driven parallel flow has been observed in a linear device, PANTA [IKK+16, KIK+16], which has uniform magnetic fields and no magnetic shear.

To describe the generation of the intrinsic flow in absence of magnetic shear, a so-called dynamical symmetry breaking mechanism has been proposed [LDXT16]. In this model, the residual stress driven by the density gradient induces a reduction in the total turbulent viscosity, and therefore amplifies the mean axial flow. In light of this model, it is now possible to address a fundamental issue of intrinsic flow studies in linear plasma devices: How are intrinsic parallel flows formed in systems without magnetic shear, and what controls the saturation of the mean flow profile? In this study, we carry out experiments in a linear device, the Controlled Shear Decorrelation eXperiment (CSDX) [BTA+05, TBC+14], and seek to answer the following questions: (1) Are parallel flows in a linear device driven by an intrinsic mechanism? (2) What is the effect of turbulent stress on mean parallel flow? (3) How do the self-generated transverse and parallel flows interact with each other?

The remainder of the present paper is organized as follows. Section 3.2 recapitulates the theoretical background that motivates the experiment. The experimental setup and approach for the measurement of turbulent stresses in CSDX is documented in Section 3.3, and the evolution of the equilibrium profiles is addressed in Section 3.4.

The scaling properties of turbulence-driven shear flow and its turbulent drive are then presented in Section 3.5, and the role of transverse flow in the generation of intrinsic axial flow is discussed in Section 3.6. Finally, the main experimental results are summarized in Section 3.7.

## 3.2 Model Summary

The turbulent axial Reynolds stress in cylindrical plasmas typically consists of a diffusive term and a residual stress term, [LDXT16] and can be written as

$$\langle \tilde{v}_r \tilde{v}_z \rangle = -\chi_z V_z' + \Pi_{rz}^{\mathrm{Res}},$$

where $\chi_z \sim \left\langle \tilde{v}_r^2 \right\rangle \tau_c$ is the positive-definite turbulent momentum diffusivity, $\tau_c$ is the autocorrelation time of turbulence, $V_z'$ is the radial gradient of the mean axial flow, and $\Pi_{rz}^{\mathrm{Res}}$ is the residual stress. Here, the momentum pinch term is ignored because there is no toroidal effect in the linear device, where the magnetic fields lines are straight and uniform. The positive-definite diffusive term, which is a diagonal term in the transport equations, can dissipate the axial flow profile but cannot act as a momentum source. The divergence of the residual stress, $-\nabla_r \cdot \Pi_{rz}^{\mathrm{Res}}$, constitutes an intrinsic turbulent force in axial direction, and can in principle serve to amplify sheared axial flow.

The residual stress is driven by the underlying turbulence, and is typically determined by the spectral correlator, i.e. $\langle k_z k_\theta \rangle \sim \sum_{\mathbf{k}} k_z k_\theta \left| \hat{\phi}_{\mathbf{k}} \right|^2$. A nonzero correlator requires symmetry breaking – that is a spectral imbalance in $\mathbf{k}$-space. Conventional mechanisms [DKG+13] for symmetry breaking are usually associated with magnetic shear, assuming $k_z \sim k_\theta x / L_s$. Accordingly, the correlator is determined by $\langle k_z k_\theta \rangle \sim k_\theta^2 \langle x \rangle / L_s$, where $L_s = \hat{s}/qR$ is the magnetic shear length. Thus a strong radial gradient of the ExB flow, $V_E'$, and/or in the turbulence intensity, $I'$, over the radial scale of the fluctuations can

break the spectral symmetry and give rise to a finite residual stress.

These conventional models, however, are not applicable to plasmas with weak or zero magnetic shear. To resolve this issue, a dynamical symmetry breaking mechanism has been proposed to explain the development of intrinsic axial flow in absence of magnetic shear. [LDXT16] According to this model, in the presence a seed axial shear flow, a finite perturbation of the mean axial flow profile can break the spectral symmetry and generate a finite residual stress, leading to a momentum flux with a negative viscosity, $\Pi_{rz}^{\mathrm{Res}} \sim \left|\chi_z^{\mathrm{Res}}\right| V_z'$, and thereby magnifying the initial flow profile perturbation. The perturbation is then amplified via a closed feedback loop, as in a modulational instability. Close to the plasma center, the seed axial shear flow, by analogy with turbulent hydrodynamic pipe flows, can be driven by an axial pressure drop between the heating source and the endplate, $\Delta P = P(z=0) - P(z=L)$, where $L$ is the axial dimension of the linear device. Flow near the device walls is presumed small due to strong plasma-neutral coupling. As a result, the radially sheared axial flow in a linear device is driven by $\Delta P$ and dissipated by the total viscosity that consists of the ambient turbulent viscosity and the negative viscosity increment induced by the residual stress, i.e. $V_z' \sim \frac{\Delta P}{\chi_z - \left|\chi_z^{\mathrm{Res}}\right|}$. Thus, with the external excitation (e.g. $\Delta P$), a total negative viscosity is not necessary to generate axial flows, and $V_z'$ is enhanced by $-\left|\chi_z^{\mathrm{Res}}\right|$.

In this dynamical symmetry breaking model, the free energy source of the residual stress is the plasma density gradient, and thus it is natural to seek to express the residual stress in terms of the density gradient. The first order parallel flow dynamics can be simplified as

$$\frac{\partial \tilde{v}_z}{\partial t} = -c_s^2 \nabla_z \left[\frac{e\tilde{\phi}}{T} + \frac{\tilde{P}}{P_0}\right] - \tilde{v}_r \frac{\partial V_z}{\partial r},$$

where $c_s$ denotes the sound speed, $\tilde{P}$ is the pressure fluctuation, and $\tilde{\phi}$ is the potential fluctuation. In a drift wave system with adiabatic electrons, we have $e\tilde{\phi}/T \sim \tilde{n}/n_0$ and $\tilde{P}/P_0 \sim \tilde{n}/n_0$ as temperature fluctuations are thought to be small in this experiment.

Consequently, the equation is reduced to

$$\tilde{v}_z \approx -\sigma_{vT}\frac{c_s^2\tau}{L_z}\frac{\tilde{n}}{n_0} - \tilde{v}_r\tau\frac{\partial V_z}{\partial r}.$$

Here, $\tau \sim \tilde{v}_r/l_c$ is the eddy turn-over time, $l_c$ is the mixing length of the turbulence, $L_z$ is the characteristic axial dimension, and $\sigma_{vT}$ is the coefficient for the acoustic coupling. Given a quasilinear response of the density fluctuation, $\tilde{n}/n_0 \sim \frac{l_c}{n_0}\frac{\partial n_0}{\partial r}$, one can obtain

$$\tilde{v}_z \approx -\sigma_{vT}\frac{c_s^2 l_c^2}{L_z}\frac{1}{n_0}\frac{\partial n_0}{\partial r} - l_c\frac{\partial V_z}{\partial r}.$$

As a result, the total turbulent stress consists of two parts, a turbulent diffusive term driven by the velocity shear and a residual term driven by the density gradient, i.e.

$$\langle \tilde{v}_r\tilde{v}_z\rangle = -\chi_z\frac{\partial V_z}{\partial r} - \sigma_{vT}\frac{c_s^2\left\langle l_c^2\right\rangle}{L_z}\frac{1}{n_0}\frac{\partial n_0}{\partial r},$$

where $\chi_z \sim l_c\tilde{v}_r \sim \left\langle \tilde{v}_r^2\right\rangle\tau$ is the turbulent viscosity. Obviously, the coefficient $\sigma_{vT}$ represents the efficiency of the density gradient in driving the residual stress, $\Pi_{rz}^{\mathrm{Res}}$, in a linear machine. $\sigma_{vT}$ can be obtained by the linear regression fit from experimental results.

## 3.3 Experimental Arrangement

The experiments were conducted on the upgraded Controlled Shear Decorrelation eXperiment (CSDX), a cylindrical plasma device with an overall length of 2.8 m and a diameter of 0.2 m (figure 3.1). The working gas was argon at a gas fill pressure of about 2 mTorr. The argon plasma was produced by a 13.56 MHz 1800 W RF helicon wave source via an antenna that surrounds a glass bell-jar, and was terminated by an insulating end-plate at the other end. The uniform magnetic field is in the axial direction (denoted

as the $-\hat{z}$ direction) and can be generated up to 2400 G. In this study the magnetic field strength was varied from 500 G to 1200 G. A higher magnetic field results in a tightened Larmor radius and is usually associated with a steepening of the density profile in CSDX. [BTA+05, TBC+14] Typical plasma parameters are as follows: the peaking electron density of $n_e \sim 1 \times 10^{19}\mathrm{m}^{-3}$, the electron temperature of $T_e \sim 3 - 5$ eV, and the ion temperature of $T_i \sim 0.3 - 0.8$ eV. More details on this device can be found in early literatures. [BTA+05, TBC+14, TGM+16]

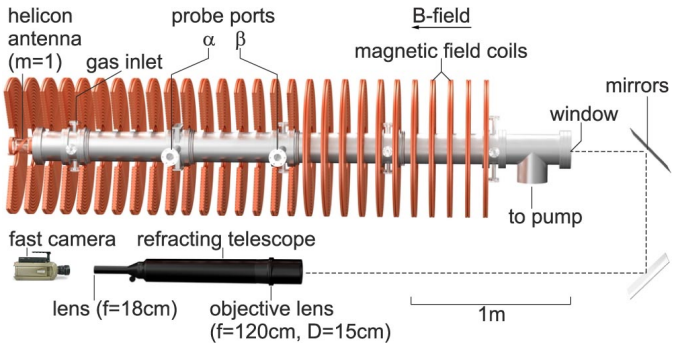


**Figure 3.1**: Schematic of CSDX with probe and fast imaging diagnostics.

A horizontal scanning probe was used to record basic plasma information such as ion saturation currents and floating potentials at port $\alpha$ that is about 1 m downstream from the helicon source. The probe array is a combination of Mach and Langmuir probes and is capable of measuring the axial and radial plasma velocities simultaneously (figure 3.2). The axial velocity, $v_z$, was measured by Mach probe which are two tips aligned nominally along the axial direction and separated by insulators. The axial velocity, according to the fluid model of ion collection by absorbing objects in combined parallel and perpendicular flows, [Hut08, PH09, MBB+11] can be given by

$$v_z = Mc_s = 0.5c_s \ln\left(\frac{J_\mathrm{u}}{J_\mathrm{d}}\right),$$

where $c_s = \sqrt{T_e/m_i}$ is the sound speed and $J_{\mathrm{u,d}}$ are the ion saturation fluxes collected by

two Mach probe tips at the up- and down-stream side. The fluctuating $\mathbf{E} \times \mathbf{B}$ velocities are estimated from the floating potential gradients between two adjacent tips ($\nabla\tilde{\phi}_{\mathrm{f}}$), i.e. $\tilde{v}_r = -\nabla_\theta \tilde{\phi}_{\mathrm{f}}/B$ and $\tilde{v}_\theta = \nabla_r \tilde{\phi}_{\mathrm{f}}/B$. The distance between two adjacent floating potential tips is about 3 mm. The sampling rate of the probe data is $f_s = 500$ kHz and the Nyquist frequency is $f_{\mathrm{Nyq}} = 250$ kHz which is well above the ion cyclotron frequency as well as the frequency of the observed dominant fluctuations ($f < 30$ kHz) in our experiments. [TBC+14] With this probe configuration, the parallel Reynolds stress $\langle \tilde{v}_z \tilde{v}_r \rangle$ and the azimuthal Reynolds stress $\langle \tilde{v}_\theta \tilde{v}_r \rangle$ can be measured simultaneously. Similar probe configurations have also been employed in other investigations on the structures of parallel ion flows. [MBB+11, IKK+16, KIK+16]

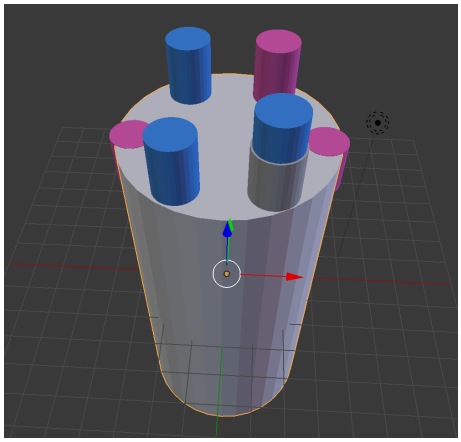

**Figure 3.2**: Illustration of a 6-tip probe array. Pink tips are negatively biased to measure the ion saturation currents; blue tips measure the floating potentials.

## 3.4 Evolution of Equilibrium Profiles

In this study, the magnetic field strength, $B$, is the only control parameter to achieve different equilibrium profiles and fluctuation intensities. As can be seen in figure 3.3(a), as the B field is raised, the plasma density and its radial gradient increases. The electron temperature $T_e$ is approximately 4 eV in the core and 2 eV at the edge (figure

3.3(b)). The inverse temperature gradient scale length, $\nabla(\ln T_e)$ is feeble compared to the inverse density gradient scale length $\nabla(\ln n)$. The temperature profile is almost unvarying during the B field scan, except a substantial increase at the very edge ($r > 6$ cm) which we do not consider here. These representative profiles are measured from discharges with 3 different magnetic fields (500, 800 and 1100 G) by an RF-compensated swept probe.

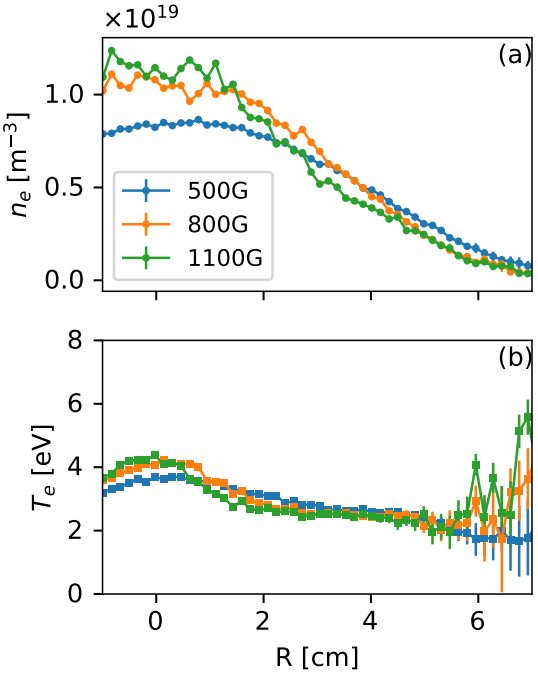


**Figure 3.3**: Equilibrium profiles of (a) plasma density, (b) electron temperature, and (c) plasma potential at three different magnetic field strength.

More detailed B scanning experiment shows that the plasma density gradient, $\nabla n_e$, rises with increasing B field strength, as can be seen in figure 3.4(a). The rise in $\nabla n_e$ leads to enhanced density fluctuation amplitude, presumably resulting from the drift-wave instability (figure 3.4(b)). Here, the fluctuations are the root-mean-square values (RMS) normalized by the maxima of their time-averaged profiles. The normalized potential fluctuation, $e\tilde{\phi}/T_e$, also increases with B field strength, and even exceeds one when $B > 1000$ G (figure 3.4(c)). The large potential fluctuations suggest that shear

instabilities like KelvinÃćÂĂÂŞHelmholtz type or centrifugal modes might become significant at higher B fields. [Jas72, MXTT11]

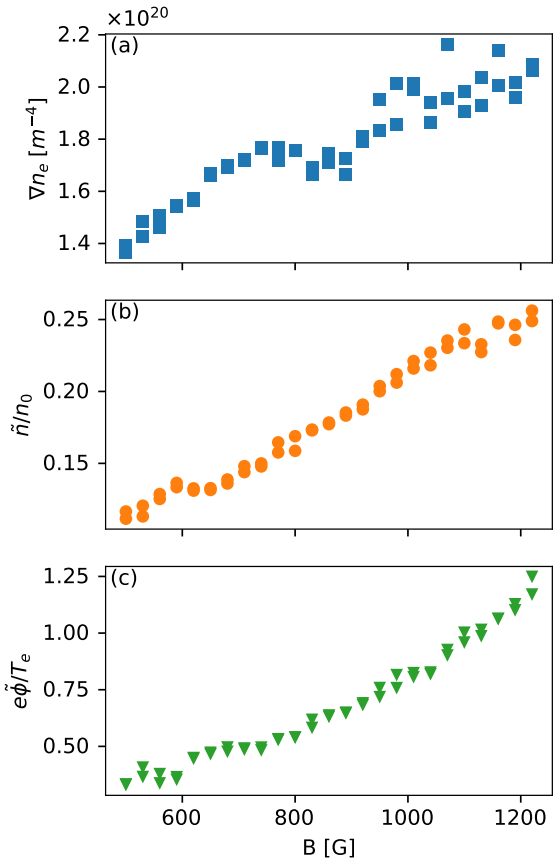


**Figure 3.4**: Maximum of (a) density gradient $\nabla n_e$, (b) normalized density fluctuations $\tilde{n}_e/n_0$, and (c) normalized potential fluctuations $e\tilde{\phi}/T_e$ as a function of magnetic field strength.

With increased density gradient and fluctuations, we seek to determine the profile evolution of axial flow and its turbulent drive. Figure 3.5 shows the radial profiles of the time-averaged parallel velocity $V_z$, the axial Reynolds stress $\langle\tilde{v}_z\tilde{v}_r\rangle$, and the corresponding axial Reynolds force $\mathcal{F}_z^{Re} = -\nabla_r\langle\tilde{v}_z\tilde{v}_r\rangle$. The time window for the averaging is about 0.1 second, i.e. $5 \times 10^4$ samples in each window with a sampling rate of $f_s = 500$ kHz. As B field is raised, the density profile has a larger peak value and a sharper gradient (figure 3.4(a)). The core axial velocity $V_z$ and its radial gradient also increase with the

B field (figure 3.5(a)). The magnitude of the $V_z$ is in agreement with previous axial ion flow measurements using laser-induced fluorescence techniques. [TAG+16] The axial Reynolds stress, $\langle \tilde{v}_z \tilde{v}_r \rangle$, is estimated using velocity fluctuations in the frequency range of $2 < f < 30$ kHz. As shown in figure 3.5(b), the axial Reynolds stress is negligible in $r < 3$ cm at lower magnetic field, and its magnitude becomes substantially negative as $B \gtrsim 800$ G. The rise in the magnitude of axial Reynolds stress leads to an increase in the axial Reynolds force $\mathcal{F}_z^{Re}$, which act to reinforce the axial velocity in core region (figure 3.5(c)). The parallel Reynolds force is about 5 times larger than the force on the ions arising from the (weak) parallel electric field that arises from the Boltzmann equilibrium associated with the electron pressure drop along the axial direction (figure 3.5(d)); thus the axial shear flows in CSDX reported here are predominantly driven by the turbulent Reynolds force and present an opportunity to test the symmetry breaking model discussed above.

The mean azimuthal flow and its turbulent drive (Reynolds stress/force) are also studied. As shown in figure 3.6(a), the azimuthal plasma fluid velocity, which is measured by the Mach probe, propagates in electron diamagnetic drift direction (negative in the plot).The peak value of $V_\theta$ increases with the magnetic field but then decreases again after approximately 800 G. Meanwhile, the magnitude of azimuthal Reynolds stress $\langle \tilde{v}_r \tilde{v}_\theta \rangle$ increases in negative direction at higher magnetic field (figure 3.6(b), leading to larger azimuthal Reynolds force $\mathcal{F}_\theta^{Re} = -\nabla_r \langle \tilde{v}_r \tilde{v}_\theta \rangle$ (figure 3.6(c)). Corresponding to the evolution of $V_\theta$ profile, $\mathcal{F}_\theta^{Re}$ also drops as B field exceeds 800 G. Noting that the fluctuation rms amplitude does not show such a drop at higher magnetic field, this collapse of $\mathcal{F}_\theta^{Re}$ suggests a threshold magnetic field strength above which the correlation between radial and azimuthal velocity fluctuation drops, i.e. a partial collapse of the eddy-tilting process in the plane perpendicular to B, although the amplitude of potential fluctuations remains increasing.

## 3.5 Scaling Properties of Intrinsic Axial Flow

The evolution of the mean profiles can also be described in terms of the magnetic field scaling, as shown in figure 3.7. The parallel flow shearing rate, $V_z' = |\partial_r V_z|$, increases with the B field for $B < 800$ G, and saturates when $B > 800$ G (figure 3.7(a)). The corresponding volume-averaged parallel Reynolds power, $\mathcal{P}_z^{av} = \int -\langle v_z \rangle \nabla_r \langle \tilde{v}_r \tilde{v}_z \rangle r dr / \int r dr$, rises with the B field but saturates after 900 G (figure 3.7(c)). At the same time, the azimuthal flow shearing rate, $V_\theta' = |\partial_r V_\theta - V_\theta / r|$, increases at lower B field but decreases subsequently after roughly 800 G (figure 3.7(b)). The volume-averaged azimuthal Reynolds power, $\mathcal{P}_\theta^{av} = \int -\langle v_\theta \rangle \nabla_r \langle \tilde{v}_r \tilde{v}_\theta \rangle r dr / \int r dr$, rises as the B field is raised to 800 G, but it drops substantially when $B > 800$ G (figure 3.7(d)). These observations indicate a fundamental change in the flow generation physics near $B_{cr} \approx 800$ G. Below $B_{cr}$, the azimuthal shear flow and its turbulence drive increase as the B field is raised; when $B_{cr}$ is exceeded, the azimuthal shear flow and corresponding Reynolds power begins to collapse. It also shows that $\mathcal{P}_z^{av}$ grows rapidly with larger azimuthal shear flow $V_\theta'$.

The magnetic field scan also demonstrates a clear rise in density gradient, as was seen in figure 3.4(a). In figure 3.8 the shearing rates and the Reynolds powers are plotted against the plasma density gradient $\nabla n_e$ which has been previously identified as the major free energy source for turbulence-driven azimuthal flow in CSDX [BTA+05, THY+06]. The results show that when $\nabla n_e$ exceeds $\nabla n_{cr} \approx 1.6 \times 10^{20}\,\mathrm{m}^{-4}$, the shearing rate of both axial and azimuthal velocities increase substantially (figure 3.8(a) and (b)). The axial Reynolds power $\mathcal{P}_z^{av}$ also begins to increase significantly at the same density gradient (figure 3.8(c)). The azimuthal Reynolds power $\mathcal{P}_\theta^{av}$, on the other hand, reaches a peak at about $1.6 \times 10^{20} < \nabla n_e < 1.7 \times 10^{20}\,\mathrm{m}^{-4}$, and then drops nearly to zero as $\nabla n_e$ exceeds $1.7 \times 10^{20}\,\mathrm{m}^{-4}$. Accordingly, the azimuthal flow shearing rate $V_\theta'$ decreases when $\mathcal{P}_\theta^{av}$ drops at larger density gradients.

The development of the turbulent drive, as mentioned in Section 3.2, is considered to be a consequence of the symmetry breaking in **k**-space. The symmetry breaking hypothesis can be assessed by checking the asymmetry and anisotropy of the correlator $\langle k_z k_\theta \rangle$, which is empirically represented by the joint PDFs of radial and axial velocity fluctuations, i.e. $\mathsf{P}(\tilde{v}_r, \tilde{v}_z) \sim \langle \tilde{v}_r \tilde{v}_z \rangle \sim \sum_{\mathbf{k}} k_z k_\theta \left|\hat{\phi}_{\mathbf{k}}\right|^2$. Figure 3.9 shows the contours of $\mathsf{P}(\tilde{v}_r, \tilde{v}_z)$ at different B field strengths at $r \approx 3$ cm. The anisotropy of $\mathsf{P}(\tilde{v}_r, \tilde{v}_z)$ grows with increasing magentic field strength. Highly tilted and anisotropic PDFs at higher B fields are associated with large asymmetry in the **k**-spectra $\sum_{\mathbf{k}} k_z k_\theta \left|\hat{\phi}_{\mathbf{k}}\right|^2$. As discussed in the theory summary above, this asymmetry can then induce a finite residual stress that drives the intrinsic flows along the axial direction.

The working hypothesis of the dynamical symmetry breaking model is that increased density gradient can drive larger turbulent Reynolds stress, which then provides the turbulent force to reinforce the radially sheared axial flows. The residual stress $\Pi_{rz}^{\mathrm{Res}}$ was computed from the measured turbulent stress and the diffusive stress inferred from experimental measurements, as discussed earlier. The resulting $\Pi_{rz}^{\mathrm{Res}}$ increases in proportion to the normalized density gradient for $B < 1000$G as shown in figure 3.10, with a slope $\sigma_{vT} \approx 0.15$. Furthermore, the magnitude of $\Pi_{rz}^{\mathrm{Res}}$ is positively related to axial flow shearing rate $V_z'$ the axial flow shearing rate $V_z'$ (3.11), suggesting that the axial velocity shear can enhanced the residual stress which in turn reinforces the axial sheared flow, e.g. a closed feedback loop like in a modulational instability. These results qualitatively agree with the picture of the dynamical symmetry breaking model [LDXT16], in which the residual stress driven by the electron drift wave turbulence induces a negative viscosity and enhances the profile gradient of intrinsic axial flow.

## 3.6 Role of Azimuthal Flow Shear

As indicated above, azimuthal shear flow itself undergoes a significant change near $B = 800$ G. In particular, as shown in figure 3.12, below 800 G, an increase in B is associated with increases in both $\mathcal{P}_\theta^{av}$ and in azimuthal flow shear $V_\theta'$; when $B > 800$ G, $\mathcal{P}_\theta^{av}$ and $V_\theta'$ both decrease with further increases in B even though the potential fluctuation RMS amplitude continues to increase with the B field (figure 3.4(c)). This collapse of $\mathcal{P}_\theta^{av}$ and $V_\theta'$ for $B > 800$G suggests destabilization of shear induced modes such as KH-like and/or interchange instabilities. We note that earlier work in CSDX [TBC$^+$14] discussed evidence for such instabilities at higher B fields.

Figure 3.13(a) demonstrates that the axial flow shear $V_z'$ is proportional to azimuthal flow shear $V_\theta'$ for $B < 800G$. Above 800G, $V_z'$ appears to saturate when $V_\theta'$ is saturated at about $2 \times 10^4$ s$^{-1}$. Meanwhile, as displayed in figure 3.13(b), for $B < 800$ G, the axial Reynolds power $\mathcal{P}_z^{av}$ increases with $V_\theta'$. For $B > 800$G, $\mathcal{P}_z^{av}$ still continues to increase with B despite the fact that $V_\theta'$ decreases by about 10%. Previous measurements in toroidal confinement devices [GHP$^+$06, XHS$^+$13] demonstrate that the residual stress and the resulting turbulent force for the axial flow can be triggered by strong $E_r \times B$ shear flow, which was taken to be consistent with the prediction of conventional symmetry breaking models [GDHS07, DKG$^+$13] that electric field shear can induce centroid shift of mean $\langle k_\parallel \rangle$ in spectrum and therefore enhance the residual stress, i.e. $\Pi_{rz}^{\mathrm{Res}} \sim V_E'$. Here, we observe that both $V_z'$ and $\mathcal{P}_z^{av}$ also increase with rising $V_\theta'$ at relatively lower magnetic field strength ($B < 800$ G), but exhibit unexpected trends at higher B fields. However, existing dynamical symmetry breaking model does not account for the effect of $V_E'$ on intrinsic axial flow. These observations suggest that it is necessary to include the interaction between the azimuthal flow, drive-wave turbulence and the axial flow in future modeling.

Figure 3.14 shows the comparison between the axial and azimuthal Reynolds

powers, i.e. $\mathcal{P}_z^{av}$ versus $\mathcal{P}_\theta^{av}$. Before 800 G, the azimuthal Reynolds power $\mathcal{P}_\theta^{av}$ increases faster than the axial counterpart $\mathcal{P}_z^{av}$, suggesting the turbulent force is dominantly in driving the azimuthal flows. When $B > 800$ G, $\mathcal{P}_\theta^{av}$ begins to decrease and reaches zero at higher B fields, while $\mathcal{P}_z^{av}$ continues increasing. For all discharges, $\mathcal{P}_z^{av}$ is smaller than $\mathcal{P}_\theta^{av}$ by about an order of magnitude. Such large distinction between the magnitudes of $\mathcal{P}_z^{av}$ and $\mathcal{P}_\theta^{av}$ indicates that the direct energy exchange is weak between axial and azimuthal flows.

## 3.7 Summary

In this study, detailed measurements of plasma profiles, including flows and turbulent Reynolds stresses in both axial and azimuthal directions, have been performed in a helicon source linear magnetized plasma deviceÃćÂĂÂŤCSDX. The probe measurements reveal that both axial flow shearing rate and its turbulent drive (Reynolds force/power) increase with increasing density gradient as the B field is raised. The parallel Reynolds stress is induced by the density gradient and becomes the primary source driving the axial flow as density gradient is steepened.

A simple dynamical symmetry breaking model is used to explore the origin of the intrinsic axial flow in plasmas with uniform magnetic field. In this model, the imbalance of spectral correlator, $\langle k_\theta k_z \rangle = \sum_{\mathbf{k}} k_\theta k_z \left|\hat{\phi}_{\mathbf{k}}\right|^2 \sim \langle \tilde{v}_r \tilde{v}_z \rangle$, is triggered by seed axial shear flow, leading to a negative diffusivity and a self-amplification of the axial shear flow via the modulational instability. The 2D joint PDF of radial and axial velocity fluctuations, $\mathsf{P}(\tilde{v}_r, \tilde{v}_z)$, has been calculated and used to represent the spectral correlator $\langle k_\theta k_z \rangle$. $\mathsf{P}(\tilde{v}_r, \tilde{v}_z)$ is highly tilted and anisotropic at higher density gradient and axial velocity shear. Furthermore, the residual stress is linearly proportional to the density gradient and is also positively related to the axial flow shear $V_z'$. These observations are

consistent with the prediction by the dynamical symmetry breaking mechanism.

On the other hand, the turbulence-driven azimuthal flow exhibits a bifurcation during the B field scan: before the transition ($B < 800$ G), the azimuthal velocity shear $V'_\theta$ and Reynolds power $\mathcal{P}_\theta^{Re}$ increase with the B field; after 800 G, $\mathcal{P}_\theta^{Re}$ collapses and $V'_\theta$ starts to fall correspondingly. Before the transition, the rises in both axial velocity shear $V'_z$ and axial Reynolds power $\mathcal{P}_z^{Re}$ are associated with increasing azimuthal velocity shear $V'_\theta$, suggesting that $V'_\theta$ plays an important role in triggering the intrinsic axial flow. However, the azimuthal Reynolds power $\mathcal{P}_\theta^{Re}$ is about 10 times larger than axial counterpart $\mathcal{P}_z^{Re}$. Therefore, the direct energy exchange between axial and azimuthal flows are relatively negligible. Until now, the effect of $V'_\theta$ is still lacking from existing dynamical symmetry breaking model and needs to be included in future studies.

# Acknowledgments

Chapter 3, in part is currently being prepared for submission for publication. R Hong, J C Li, S C Thakur, R Hajjar, P H Diamond, and G R Tynan. The dissertation author was the primary investigator and author of this material.

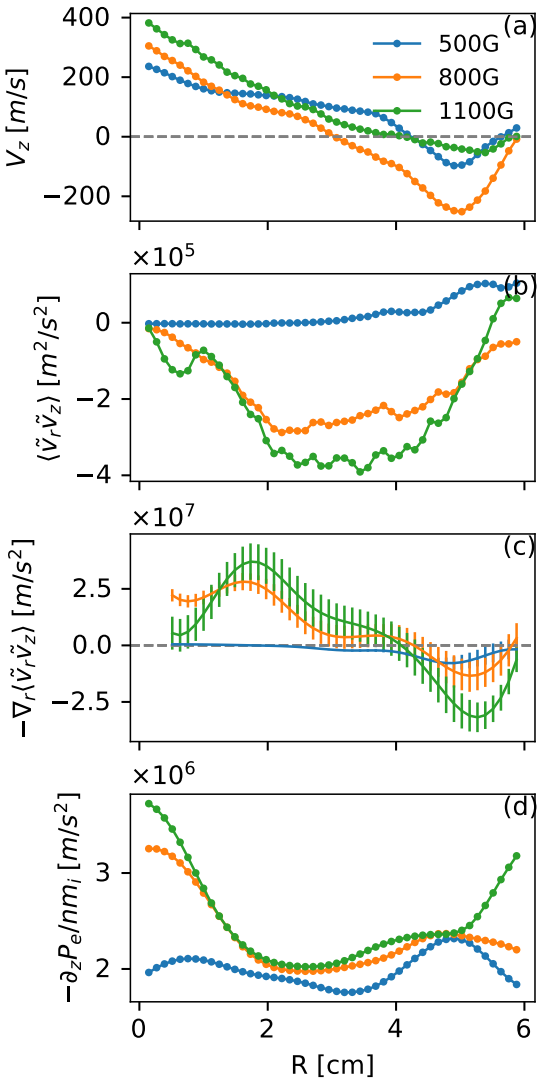


**Figure 3.5**: The time-averaged radial profiles of (a) axial velocity $V_z$, (b) axial Reynolds stress $\langle \tilde{v}_z \tilde{v}_r \rangle$ , (c) the axial Reynolds force $\mathcal{F}_z^{Re} = -\nabla_r \langle \tilde{v}_z \tilde{v}_r \rangle$, (d) and axial pressure force at 3 different magnetic fields.

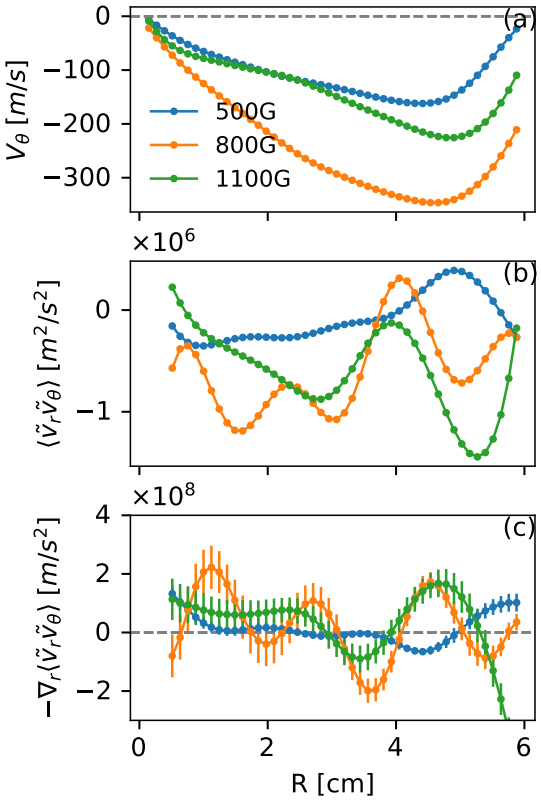


**Figure 3.6**: The time-averaged radial profiles of (a) azimuthal velocity $V_\theta$, (b) azimuthal Reynolds stress $\langle \tilde{v}_r \tilde{v}_\theta \rangle$, and (c) the azimuthal Reynolds force $\mathcal{F}_\theta^{Re} = -\nabla_r \langle \tilde{v}_r \tilde{v}_\theta \rangle$ at 3 different magnetic fields.

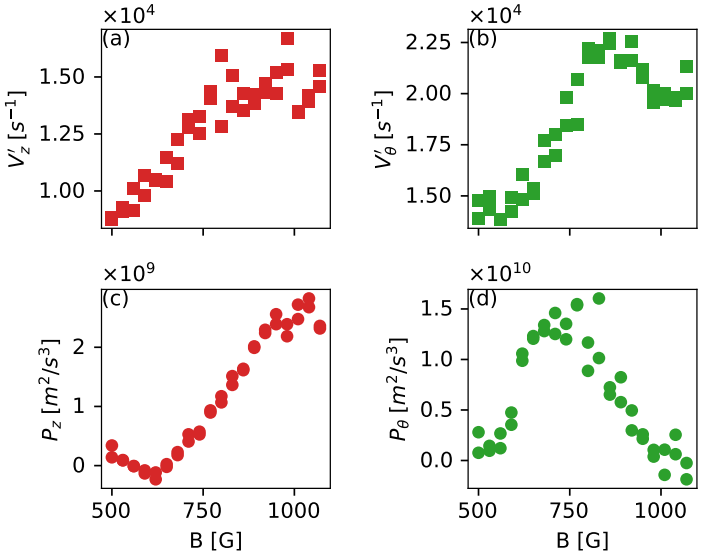


**Figure 3.7**: The axial flow shearing rate of $V_z'$ (a), azimuthal flow shearing rate $V_\theta'$ (b), the volume-averaged axial Reynolds power $\mathcal{P}_z^{av}$ (c), and the volume-averaged azimuthal Reynolds power $\mathcal{P}_\theta^{av}$ (d) are plotted as a function of the B field.

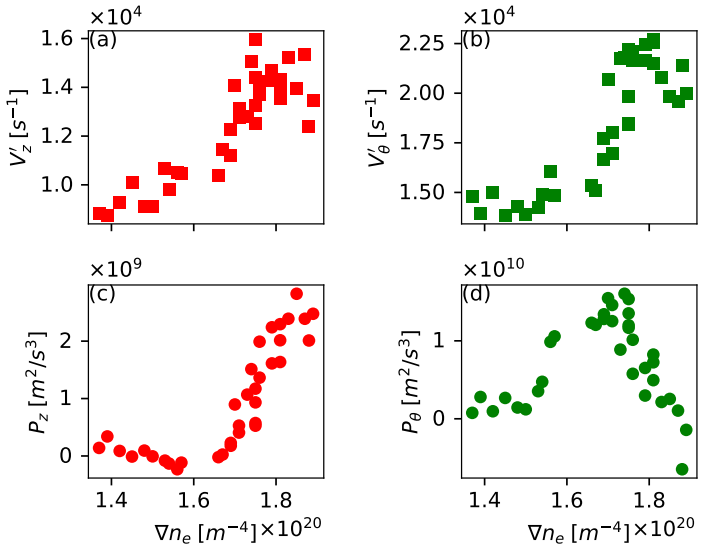


**Figure 3.8**: The axial flow shearing rate of $V_z'$ (a), azimuthal flow shearing rate $V_\theta'$ (b), the volume-averaged axial Reynolds power $\mathcal{P}_z^{av}$ (c), and the volume-averaged azimuthal Reynolds power $\mathcal{P}_\theta^{av}$ (d) are plotted as a function of the density gradient $\nabla n_e$.

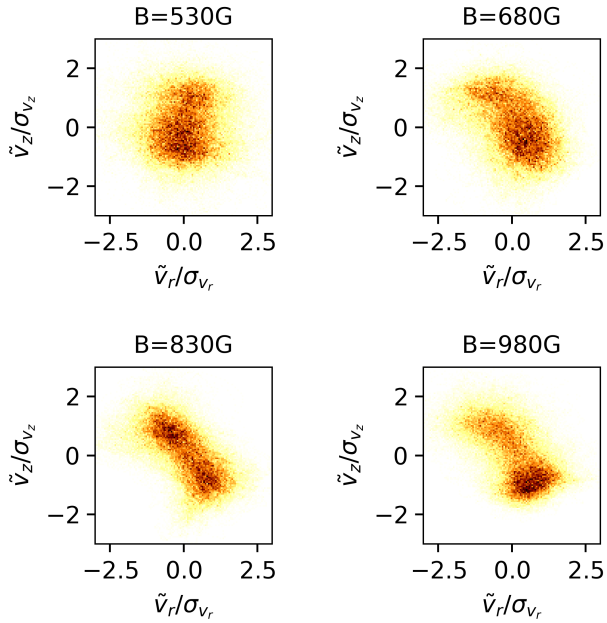


**Figure 3.9**: Joint PDF of radial and axial velocity fluctuations, $\mathrm{P}(\tilde{v}_r, \tilde{v}_z)$, at six magnetic fields at $r \approx 3$ cm. Normalization is the standard deviations.

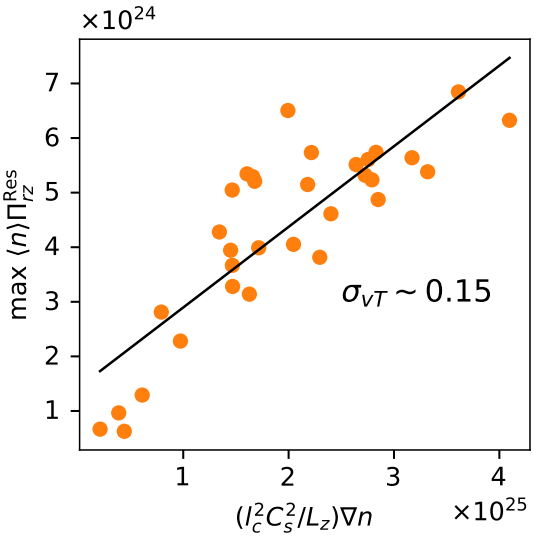


**Figure 3.10**: Comparison between residual stress and normalized density gradient. The coefficient, $\sigma_{vT}$, is estimated to be about 0.15 by the linear fit.

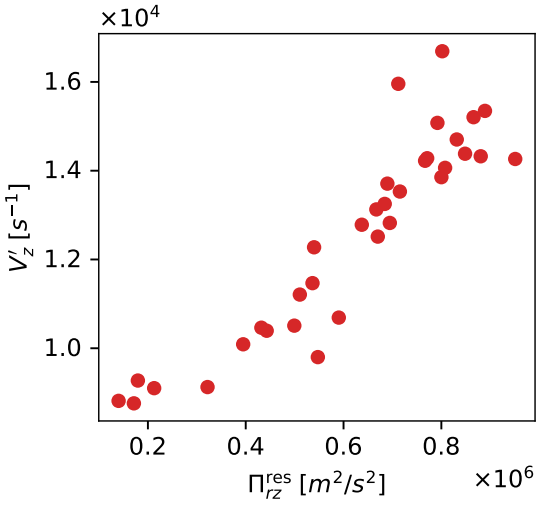


**Figure 3.11**: Axial flow shearing rate $V_z'$ plotted as a function of residual stress $\Pi_{rz}^{\mathrm{Res}}$.

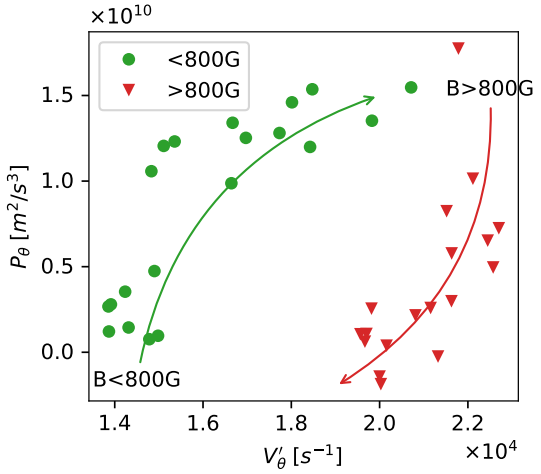


**Figure 3.12**: Azimuthal Reynolds power $\mathcal{P}_\theta^{av}$ is plotted as a function of azimuthal velocity shearing rate $V_\theta'$. Low field data ($B < 800$ G) are presented by green circles, high field data ($B > 800$ G) by red triangles.

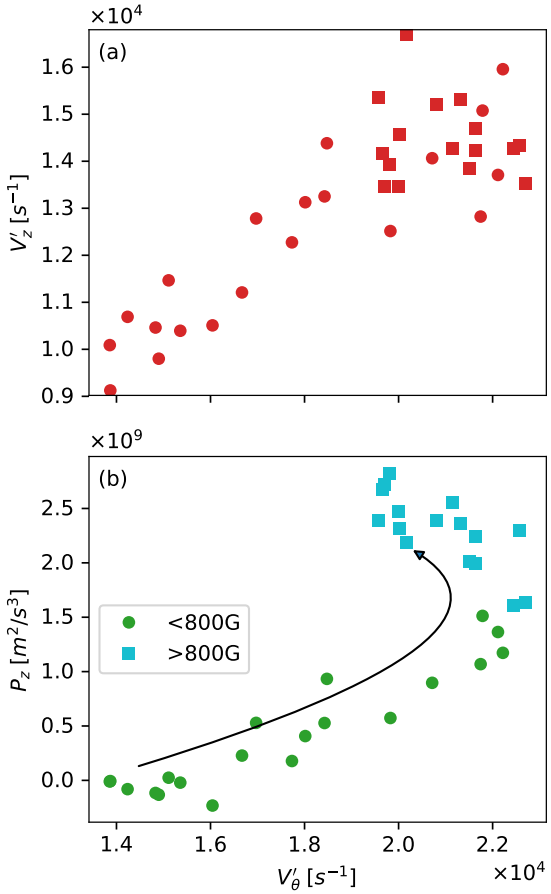


**Figure 3.13**: Azimuthal velocity shear, $V'_\theta$, versus (a) axial velocity shear, $V'_z$, and (b) axial Reynolds power, $\mathcal{P}_z^{av}$. The black curve in (b) indicates the evolution trajectory of $\mathcal{P}_z^{av}$ as B field is raised.

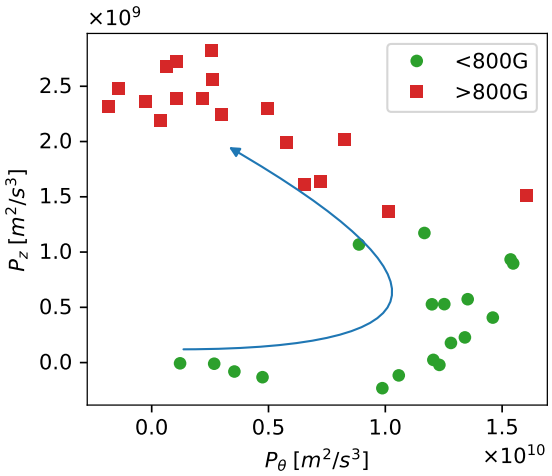


**Figure 3.14**: Comparison between $\mathcal{P}_z^{av}$ and $\mathcal{P}_\theta^{av}$. Blue curve indicates the evolution trajectory as B field is raised.

# Chapter 4

# Characterization of SOL Plasma Flows and Potentials in ICRF-Heated Plasmas in Alcator C-Mod

In previous two chapters, we have seen the development of turbulence-driven shear flows in both toroidal devices like HL-2A tokamak and linear laboratory machines like CSDX. These shear flows usually occur near regions with strong fluctuations driven by large gradient of various profiles. However, there are other large-scale sheared flows observed in regions in the absence of large pressure gradient, such as scrape-off layer (SOL) region in tokamaks. These dc flows are driven by externally launched electric field excited by RF antennas, and significantly change the motion of turbulent eddies moving across the region affected by the external RF fields. However, these electric fields not only affect the flows of plasmas near the antennas, but also accelerate the ions and increase the erosion rate of the plasma facing materials. In this chapter, we are going to characterize these electric fields and induced plasma potentials, by tracking motion of the turbulent eddies near the RF antennas.

## 4.1 Introduction

Ion cyclotron range of frequency (ICRF) heating is one of a few promising auxiliary heating techniques for achieving thermonuclear fusion relevant temperatures in magnetic confinement fusion devices. Furthermore, 20 MW of ICRF power is planned for in ITER for plasma heating and current drive [SG07]. While demonstrated to efficiently heat D-T plasmas to thermonuclear temperatures, e.g. TFTR [WBD$^+$95] and JET [SJB$^+$98], ICRF heating is often associated with enhanced core impurity contamination, which makes it incompatible with high performance plasmas [LPL$^+$01, WGO$^+$13, BBD$^+$16]. Although the mechanism is not fully understood, the RF-enhanced plasma potential associated with ICRF power has been thought to play a significant role through increased sputtering near the ICRF antennas [WGO$^+$13, GW12]. RF-enhanced plasma potentials and electric fields have been observed in the vicinity of the energized RF antennas in C-Mod and Tore-Supra [FCHG10, GW12, MD08, MD10b, CTW$^+$12, OWB$^+$14].

The basic physical picture for RF-enhanced plasma potentials is well known [BK63, NO89, Per89]. Electrons respond faster to the parallel electric field of RF waves ($E_\parallel$) than ions, and develop rectified sheath potentials to balance the electron and ion fluxes over a RF-cycle and maintain time-averaged quasi-neutrality. This rectified sheath potential is associated with the slow wave (SW) that can be generated directly from the antenna or be converted from unabsorbed fast waves (FWs) into SWs in the scrape-off layer (SOL) [MD08, MD10b]. According to conventional models, the decay length of the SW is the same order as the plasma skin depth, $\delta_{\mathrm{pe}} = c/\omega_{\mathrm{pe}}$, which is no more than a few millimeters in the far SOL region of tokamaks. Some experimental observations, however, have confirmed that the radial expansion of RF-enhanced plasma potentials could be considerably larger than the skin depth [CTW$^+$12, OWB$^+$14]. Since the discover of this ‘anomalousÃćÂĂÂŹ penetration depth of the dc potential structures, a number

of models have been proposed to explain the underlying physics that broaden the radial structure of the RF-sheath [FCHG10, CJH+12, CLK+17].

In most experiments, the rectified sheath structures are directly measured by conventional or emissive Langmuir probes [OWB+14, OWB+13]. However, the operation of probes is often limited in RF-heated plasmas since the high heat flux easily shortens the lifetime of the probe. Moreover, probes can only measure the 1D profile of the RF sheath potential in each single shot, while 2D resolution would be highly useful as the currents in the ICRF antenna are expected to break the poloidal symmetry. Recently the gas-puffing-imaging (GPI) diagnostics have been utilized to detect the structures of the RF-enhanced plasma potentials in the Alcator C-Mod tokamak [CTW+12]. The GPI diagnostics, being capable of observing a 2D area near the ICRF antenna in a single shot and at higher temperature, can overcome challenges of using probes in RF-heated plasmas.

In this study, we use the 2D GPI signals to estimate the velocity of the SOL turbulent structures, which are advected by the ICRF-induced $\mathbf{E} \times \mathbf{B}$ flows. The 2D velocity field is calculated using the time-delay estimation (TDE) techniques. Then the magnitude and radial extension of RF-enhanced electric fields and plasma potentials near the ICRF antennas can be determined.

## 4.2 Experimental Setup

The SOL plasma flows and ICRF-enhanced plasma potentials are measured in ICRF-heated deuterium majority plasmas in Alcator C-Mod tokamak in which the plasma-facing components (PFCs) are entirely composed of high-Z molybdenum tiles [HBB+94]. ICRF antennas are located at three different ports (Fig. 4.1(b)-(c)). More detailed descriptions of C-Mod and its ICRF antennas can be found in previous papers

[HBB+94, GBB+14, WGO+13, BPW+07].All discharges in this study were operated in L-mode. The plasma response to ICRF waves is diagnosed using the 2D gas-puffing imaging (GPI) system, which detects the line radiation of the injected neutral gas (He 586 nm in this study) and is able to trace the motion of the emissive turbulent structures [CTHL10, CTW+12, CDF+13]. The diagnostic gas puffs are injected from a 4-barrel nozzle mounted on the low-field-side (LFS) limiter. To avoid disturbing the measurements of RF-induced plasma flows, the amount of the helium gas used by GPI diagnostics is precisely controlled and is much less than that for impurity seeding. Further GPI derived potentials were compared with emissive probe measurements and we found to agree [OWB+13]. In the discharges studied in this paper, the nozzle is 3 cm outside the separatrix and 2.54 cm below the midplane. The field of view (FOV) of the 2D GPI array, as shown in Fig. 4.1(a), covers an area of 3.5 cm × 3.9 cm in the radial-vertical plane. The imaging data are sampled at 2 MHz by avalanche photodiodes (APDs). Although the FOV of GPI is toroidally separated from the energized ICRF antennas ($L_{\|} \sim 2$ m), it is magnetically connected with some parts of the D and J antenna, as can be seen in Fig. 4.1(c). Therefore, the GPI system is able to measure the plasma potential on fields local to ICRF antennas. In 2012 the toroidally aligned (TA) J antenna was replaced by a "field-aligned" antenna, the "FA-J ant", whose four current straps and antenna box structure are perpendicular to the total magnetic field (for $q_{95} \sim 3.8$) [WGO+13]. One of the primary motivations for installing the field-aligned antenna was to reduce integrated parallel RF electric fields, the very field whose sheath rectification is suspected to produce the RF-induced plasma potentials that are examined in this study.

## 4.3 Plasma Flows and Electric Fields in the SOL Region

### 4.3.1 Time-Delay Estimation and 2D Velocity Field

By using the data from the 2D APD GPI array, we are able to obtain the plasma flows induced by the rectified sheath potential in the SOL region via the time-delay estimation (TDE) technique. In the TDE technique, the cross-correlations of the observed brightness fluctuations $\tilde{I}$ from the 586 nm He I line emission on neighboring spots are calculated. To estimate the time interval for fluctuations to propagate between two observation locations, the time lag of the maximum correlation, $\tau_m$, can be obtained and the local velocities of the emissive structures are simply estimated as

$$v_{ij} = \frac{d_{ij}}{\tau_m},$$

where $d_{ij}$ is the distance between two observation points. In this study, a time window of $\tau \sim 0.1$ ms is used for calculating the cross correlation, which corresponds to a sample length of 200 frames, introducing an effective Nyquist frequency of 10 kHz in the velocity estimations.

Typical equilibrium velocity fields of SOL plasmas at varied ICRF heating powers are shown in Fig. 4.2. Different colors stand for different directions and magnitudes of poloidal flows. Red arrows point in the electron diamagnetic direction (EDD) which is upward, while the blue arrows point in the ion diamagnetic direction (IDD) which is downward. In ohmic plasmas, the poloidal flows in the SOL region is usually in the IDD direction, because the Bohm sheath drop leads to an outward radial electric field [Sta00], $E_r \approx -3\partial_r T_e/e > 0$, and thus a $\mathbf{E}\times\mathbf{B}$ poloidal velocity in the IDD, $V_\theta \approx 3\partial_r T_e/eB_\varphi$, where $B_\varphi$ is the strength of the toroidal magnetic field. At low ICRF powers, poloidal flows near the LCFS are still in the IDD direction ($89 < R < 90$ cm), but poloidal

velocities near the antenna change from IDD to EDD ($90 < R < 91$ cm). The changes of flow patterns near the antenna strongly suggest that large-scale flow patterns are induced on the field lines magnetically connected to active ICRF antennas.

In our previous study, radial profiles of the poloidal phase velocities were estimated from the experimental dispersion relation, i.e. local conditional spectra $S(k_\theta|f)$ [CTW+12]. The TDE techniques used in this study have been benchmarked against the phase velocity estimations. The velocity profiles from the TDE techniques are in agreement with previous estimations based on $S(k_\theta|f)$ structures. However, the poloidal phase velocity estimations are based on Fourier transform and simply assume that $V_\theta$ is uniform along poloidal direction, while the TDE techniques are able to give more information such as 2D velocity fields and variations in $V_\theta$ along the poloidal direction, as shown in Fig. 4.2. The oversimplified assumption of uniformity along poloidal direction encounters difficulty as the currents in active antennas and their box frames break the poloidal symmetry. Therefore, the analysis based on phase velocity estimations have inherit difficulty in capturing the poloidal variations of RF-induced electric fields and plasma potentials. On the other hand, although not presented in this study, the TDE techniques are capable of showing the 2D distribution of RF-induced radial electric fields and the poloidal profile of RF-induced plasma potentials, and hence would be beneficial to future investigations of the RF physics.

### 4.3.2 Broadening of Radial Electric Fields at Higher ICRF Power

The radial profiles of the poloidal velocity can be obtained by averaging the 2D velocity field along the poloidal direction. Figure 4.3(a) shows the resulting equilibrium profiles of poloidal velocities, $V_\theta(r)$, at $B_\varphi = 2.7$ T under different ICRF powers in L-mode plasmas. The radial electric field can then be inferred from the poloidal velocity, $E_r(r) = -V_\theta B_\varphi$ (shown in Fig. 4.3(b)), since the $\mathbf{E} \times \mathbf{B}$ flows is large compared to the

flow induced by thermal sheath drop in the far SOL region [CTW$^+$12, OWB$^+$14]. For the discharge at $B_\varphi = 2.7$ T, ICRF waves induce an inward radial electric field, $E_r$, near the active antenna, while the direction of $E_r$ near the separatrix remains outward. This change in $E_r$ is considered as a result of the ICRF rectified sheath. Results also show that as ICRF power is raised, the magnitude of $V_\theta$ and the RF-induced $E_r$ become larger.

Figure 4.4 shows the radial profiles of poloidal velocity, $V_\theta(r)$, and radial electric field, $E_r(r)$, at different ICRF powers launched by the D antenna when $B_\varphi = 7.9\,\mathrm{T}$ . In this discharge, the radial extension of the inward $E_r$ induced by ICRF waves is less than 1 cm when $P_{\mathrm{ICRF}} \leq 0.5$ MW. But the induced $E_r$ immediately extends to the separatrix, as $P_{\mathrm{ICRF}}$ is raised to 0.75 MW and beyond.

As observed from profiles plotted Fig. 4.3 and 4.4, the width of inward $E_r$ induced by ICRF waves near the antenna is $\lambda_\perp \sim 1 - 2\,\mathrm{cm}$ and is much larger than the local skin depth $\delta_{\mathrm{pe}} = c/\omega_{\mathrm{pe}} \approx 1 - 3\,\mathrm{mm}$ which is the expected penetration length of the SW. A number of theoretical models have been proposed to explain this "anomalous" penetration length of the dc potential and electric field structure [FCHG10, MD08, MD10b]. A possible mechanism is due to the self-consistent exchange of the transverse RF current between neighboring flux tubes [FCHG10]. The broadening of the penetration length, according to the linear modeling, is predicted to be $\lambda_\perp \sim \left(L_\parallel \rho_{\mathrm{ci}}/2\right)^{1/2}$ at large RF powers. This model yields $\lambda_\perp \approx 1\,\mathrm{cm}$ at the real C-Mod conditions of $\rho_{\mathrm{ci}} \approx 0.01\,\mathrm{cm}$ and the connection length $L_\parallel \approx 200\,\mathrm{cm}$, which is shown to be consistent with preceding GPI observations [CTW$^+$12] at $B_\varphi = 5.4\,\mathrm{T}$ (data points shown in Fig. 4.5). In addition, the model indicates that the radial width should be reduced at higher magnetic field ($\lambda_\perp \sim \rho_{\mathrm{ci}}^{1/2} \sim B_\varphi^{-1/2}$). However, as can be seen in Fig. 4.5, the observed radial width of the ICRF-induced $E_r$ substantially *increases* from $\lambda_\perp \approx 0.9\,\mathrm{cm}$ to $\sim 1.8$ cm when $B_\varphi$ is raised from 2.7 to 7.9 T at larger ICRF heating powers. The radial expansion of ICRF-induced $E_r$ at $B_\varphi = 7.9$ T with larger heating power covers the whole SOL

region, i.e. $\lambda_\perp \approx L_{\mathrm{SOL}}$, which corresponds to a significantly increased plasma potential, $\phi_{\mathrm{ind}}$, near the active antenna. This large plasma potential can accelerate ions along the magnetic field and enhance the sputtering on PFCs.

## 4.4 ICRF-induced Plasma Potentials

Since the ICRF-induced plasma potential arises from the rectified parallel electric field from slow waves, it is predicted to be proportional to the square root of the ICRF power [FCHG10],

$$\phi_{\mathrm{ind}} \sim P_{\mathrm{ICRF}}^{1/2}.$$

This scaling has been examined in previous power scan experiments [CTW+12, OWB+13, OWB+14, WGO+13]. This plasma potential can also be estimated by integrating $E_r$ determined by the GPI measurement. The inferred radial electric field near the active ICRF antenna consists of two components: (a) the rectified RF field from the ICRF antenna; (b) the background electric field due to the thermal sheath drop, i.e. $E_{r0} = -3\partial_r T_e/e$, which can be estimated from the ohmic plasmas and is typically small compared to the RF-enhanced part [CTW+12]. The peak value of the induced potential can be evaluated as

$$\phi_{\mathrm{ind}} = -\int_{r_{\mathrm{sep}}}^{r_{\mathrm{ant}}} E_{r,\mathrm{ind}}\,\mathrm{d}r = B_\varphi \int V_{\theta,\mathrm{ind}}\,\mathrm{d}r. \tag{4.1}$$

In this experiment, different heating scenarios have been utilized to study other effects on the rectified sheath potential, such as the toroidal field strength, the impurity seeding, antenna geometry and current strap phasing.

### 4.4.1 Dependence on Toroidal Field Strength

Recent experiments suggest that large convective cells induced by RF waves may play an important role in enhanced ICRF impurity sources and contamination [WGO$^+$13, CTW$^+$12]. The cell strength scales $B_\varphi^{-1/2}$ [FCHG10] and thus we expect the convective cell and peak potential to decrease with higher toroidal field strength. To probe the convective cell strength and induced plasma potentials, we seek to characterize the dependence of the SOL turbulence poloidal velocity on toroidal field using GPI imaging data and TDE techniques.

Estimated peak values of the ICRF-enhanced plasma potentials that are induced by the D antenna are plotted in Fig. 4.6, as a function of the ICRF powers, at three different toroidal magnetic fields, $B_\varphi$ = 2.7, 5.4 and 7.9 T. To achieve a similar safety factor and plasma shape, the plasma current $I_p$ was scaled with $B_\varphi$. The induced potentials $\phi_{\rm ind}$ scaled approximately as $P_{\rm ICRF}^{1/2}$, which is in agreement with the model of rectified sheath potentials. As $B_\varphi$ was increased from 2.7 to 7.9 T, $\phi_{\rm ind}$ increased substantially. This could be partly attributed to the significant radial expansion of $E_r$ at higher $B_\varphi$. In addition, the measured $V_\theta$ did *not* scale down as the $B_\varphi$ was raised, which could also contribute to the large plasma potential.

In all cases the induced potentials were much larger than the background thermal sheath potential ($3T_e \sim 30$ eV). In particular, for $B_\varphi = 7.9$ T and $P_{\rm ICRF} = 1.5$ MW, the maximum of the induced potential was about 600 V. The large induced potential can enhance the sputtering yield on the PFCs and thus increase the background impurity content considerably [WLL$^+$09, OWB$^+$13]. This result presents a challenge to the control of the plasma-material interaction in high-field fusion devices, as well as the concepts of high-field-side launch of RF waves, which are expected to yield a better heating efficiency of thermal ions without generating energetic minority ion tails [WBB$^+$15].

Complicating the interpretation of the RF enhanced potential dependence on $B_\varphi$

are the differences in ICRF absorption scenarios and edge conditions. In C-Mod, different $B_\varphi$ correspond to different ICRF absorption mechanisms in these experiments. For 2.7 T, second harmonic H minority heating is utilized whereas fundamental minority H and $^3$He heating are used at 5.4 T and 7.9 T, respectively. In C-Mod, the RF power absorption effectiveness in the plasma core is highest for H minority heating whereas both the second harmonic H minority and fundamental minority $^3$He heating are both substantially weaker. Within this data set, the lowest and highest RF enhanced potentials correspond with the weaker central absorption indicating that dependence on $B_\varphi$ is unlikely to be a result of differences between core absorption scenarios. The normalized density, ratio of density to the Greenwald density $\bar{n}/n_G$, for the three discharges shown is 0.4-0.44, 0.23-0.28, and 0.21-0.23 for the 2.7 T, 5.4 T, and 7.9 T discharges respectively. The RF enhanced potentials are lowest for the largest normalized density and highest for the smallest normalized density. This suggests the plasma edge conditions play a role as well as the RF fields. The understanding, however, between strength of RF absorption, plasma edge conditions and induced plasma potential is incomplete and requires further studies.

### 4.4.2 Effects of Impurity Seeding

The performance of ICRF-heated plasmas was found to be improved with impurity seeding in previous experiments [GBB$^+$14]. Contributing to this effect is the reduction of ICRF-specific impurities particularly core Mo concentration and reduced core impurity radiation. To investigate the response of the RF-induced plasma potential to the impurity seeding, low-Z gases (helium, nitrogen and neon) were puffed near the antenna. The seeding gases were puffed with a pressure of 2 psi and a pulse duration of 200 ms at 50 V on the piezo. Figure 4.7 shows the estimated RF sheath potentials induced by the TA D antenna with different kinds of low-Z impurities. The peak values of RF-induced plasma potentials decreased by about 30% when impurity gases are injected. Moreover, with

impurity seeding the response of the RF-induced potential to the ICRF power deviates from the $P_{\mathrm{ICRF}}^{1/2}$ scaling considerably. A possible cause of the reduction in RF sheath potential is that high neutral contents may substantially increase the collisionality/resistivity and damp the plasma flows in the SOL region. High collisionality/resistivity will limit the transverse current between neighboring flux tubes, and thus inhibit expansion of the radial electric field and the plasma potential induced by the ICRF waves.

Injecting impurity gases usually increases the plasma density in the SOL region. The increase in the edge density, as predicted by the SW rectification model, will increase the RF sheath potential, as long as the edge density is greater than a threshold (about $10^{16}\,\mathrm{m}^{-3}$ in C-Mod) [MD08, MD10b]. The threshold has been observed by the probe measurements in C-Mod [OWB$^+$14], however, the GPI observations in the impurity seeding experiments do not agree with the model. Clearly, further work is needed to understand the effects of the impurity seeding on the RF sheath.

### 4.4.3 Field-Aligned Antenna vs. Toroidally-Aligned Antenna

To reduce the RF sheath potential and the impurity content, C-Mod has recently implemented the design of the field-aligned (FA) antenna [GW12]. The FA antenna is distinguished from the conventional toroidally-aligned (TA) antenna by current straps and an antenna box structure that are perpendicular to the total magnetic field. Such a symmetrical design, as predicted by 3D antenna modeling, are expected to minimize the integrated $E_{\|}$ (electric field along a magnetic field line), and lead to a reduction of the RF-induced plasma potential [GW12, WGO$^+$13]. The RF-induced plasma potentials calculated using TDE techniques are shown in Fig. 4.8, which is consistent with previous analysis based poloidal phase velocity estimations [WGO$^+$13]. Although the reduction of the impurity level has been observed in the plasmas heated by FA antenna [WGO$^+$13, GBB$^+$14], the potential induced by FA antenna was similar to that by TA

antenna in present study. The observations indicate that, although the reduction in the integrated $E_{\|}$ can reduce the release of ICRF-specific impurities, the local RF-$E_{\|}$ and RF sheath potential may not decrease.

On the other hand, we note that recent experiments in ASDEX Upgrade also show a significant reduction of the impurity tungsten (W) released from ICRF antennas when the new 3-strap antenna (toroidally-aligned) is used [BBD+16]. Particularly, a minimum W content in core plasma was achieved as the power ratio between the central strap and the outer straps was varied from $\frac{1}{1}$ to $\frac{3}{1}$. This narrow range of the power ratio corresponds to a cancellation of RF image currents and therefore minimizations of both local RF-$E_{\|}$ fields and RF sheath potentials on the side limiters [BAB+17]. These findings imply that the significant plasma potentials induced by FA antennas may result from the image currents on the side limiters and antenna box structures.

### 4.4.4 Monopole Phasing vs. Dipole Phasing

According to 3D antenna modeling, the reduction in integrated $E_{\|}$ depends on the relative phases of the current straps [WGO+13]. For the FA antenna, the monopole phasing is predicted to exhibit the lowest integrated $E_{\|}$. The TDE techniques have also been used to estimated the RF-induced plasma potentials, and show consistent results with previous analysis [WGO+13]. As demonstrated in Fig. 4.9, the measured plasma potential induced in the monopole phasing was significantly larger than in the dipole phasing. Consistent with the behavior of RF-enhanced plasma potentials, the local impurity source from the antenna in the monopole phasing is also found to be larger than that in the dipole phasing [WGO+13]. Again, this substantially higher value of RF sheath potential might arise from the RF image currents on the FA antenna box structures. The lack of poloidal symmetry in monopole phasing antenna might also lead to larger image currents and RF sheath potentials.

## 4.5 Summary

In this study, the ICRF-induced plasma potentials and radial electric fields have been investigated using gas-puffing imaging techniques in the Alcator C-Mod tokamak. The equilibrium plasma flows that advect turbulent structures in SOL region has been calculated using TDE techniques. The results of radial profiles from TDE analysis are in agreement with previous analysis based on poloidal phase velocity estimations. The TDE techniques are able to show 2D distributions of RF-induced $E_r$ and $\phi_{\rm ind}$, and will be beneficial for future studies of RF physics.

The large convective cells induced by the RF sheath electric field are observed in the vicinity of the active ICRF antenna. The radial width of this field is $1-2\,$cm and *increases* as the toroidal magnetic field is raised. In most discharges, the peak values of the ICRF-induced potential, $\phi_{\rm ind}$, scale as $P_{\rm ICRF}^{1/2}$ and are proportional to the strength of the toroidal magnetic field. In particular, $\phi_{\rm ind} \approx 600\,$V is observed at $B_\varphi = 7.9\,$T. However, $\phi_{\rm ind}$ was decreased by sufficiently strong low-Z impurity seeding, and the potentials began to deviate from the $P_{\rm ICRF}^{1/2}$ scaling. The sheath potential induced by the FA antenna was similar to that by TA antenna in disagreement with the modeling which indicate that the FA antenna should produce lower integrated $E_\parallel$. In addition, while monopole FA antenna modeling predicts lower integrated $E_\parallel$ than dipole phasing modeling, it induced substantially higher sheath potential in our experiments. These discrepancies between the observations and the modeling may be attributed to the RF image currents on the FA antenna box structures, but further work is needed to test these conjectures.

The large $\phi_{\rm ind}$ at high toroidal magnetic field is expected to enhance the sputtering yields on PFCs adjacent to the active antenna. Therefore, new designs of ICRF antenna should try to minimize the local RF-$E_\parallel$ fields and related plasma-material interactions close to the antenna.

Finally, the measurements of the radial broadening of the RF sheath structure at different magnetic field do not support the scaling $\lambda_\perp \sim \left(L_\parallel \rho_{\mathrm{ci}}/2\right)^{1/2}$ predicted by theoretical modeling. Additional theory and experimental work is required to clarify the underlying physics.

# Acknowledgments

The text and data in Chapter 4 is a reprint of the material as it appears in Plasma Physics and Controlled Fusion, 2017, R Hong, S J Wukitch, Y Lin, J L Terry, I Cziegler, M L Reinke and G R Tynan. Copyright 2017 IOP Publishing. The dissertation author was the primary investigator and author of this paper.

The authors greatly appreciate the effort and support of the entire Alcator C-Mod team in performing these experiments. This work is supported by the U.S. DoE, Office of Science, Office of Fusion Energy Sciences, User Facility Alcator C-Mod under DE-FC02-99ER54512 and DE-SC 0010720.

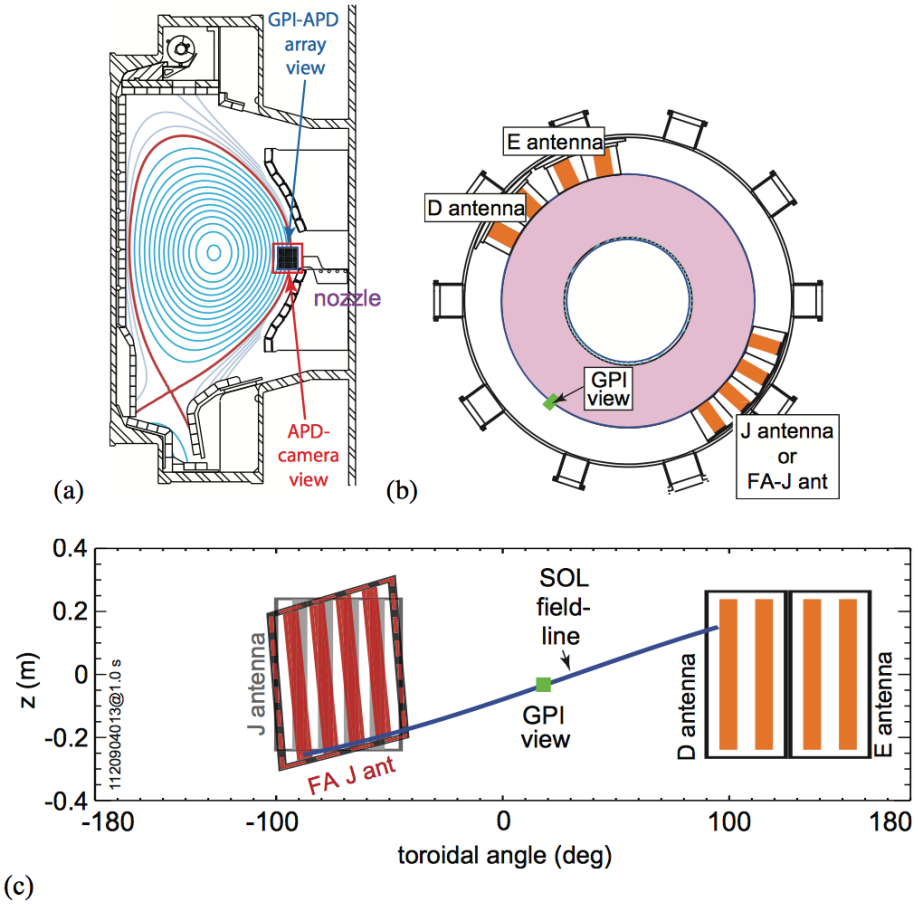


**Figure 4.1**: (a) Poloidal X-section of C-Mod at the GPI toroidal location. GPI views are oversize for clarity. (b) Top view of C-Mod showing the GPI view in relation to the ICRF antennas. (c) The toroidal layout of the antennas and GPI view along with the field-line that maps from the GPI view to its magnetically connected location on the FA-J antenna. The "TA-J antenna" (in gray behind the "FA-J ant") was replaced by the ÃćÂĂÂIJFA-J antÃćÂĂÂİ in early 2012. Note that the straps of the "TA-J antenna" were vertical, while those of the "FA-J ant" are perpendicular to the local field-line for $q_{95} = 3.8$.

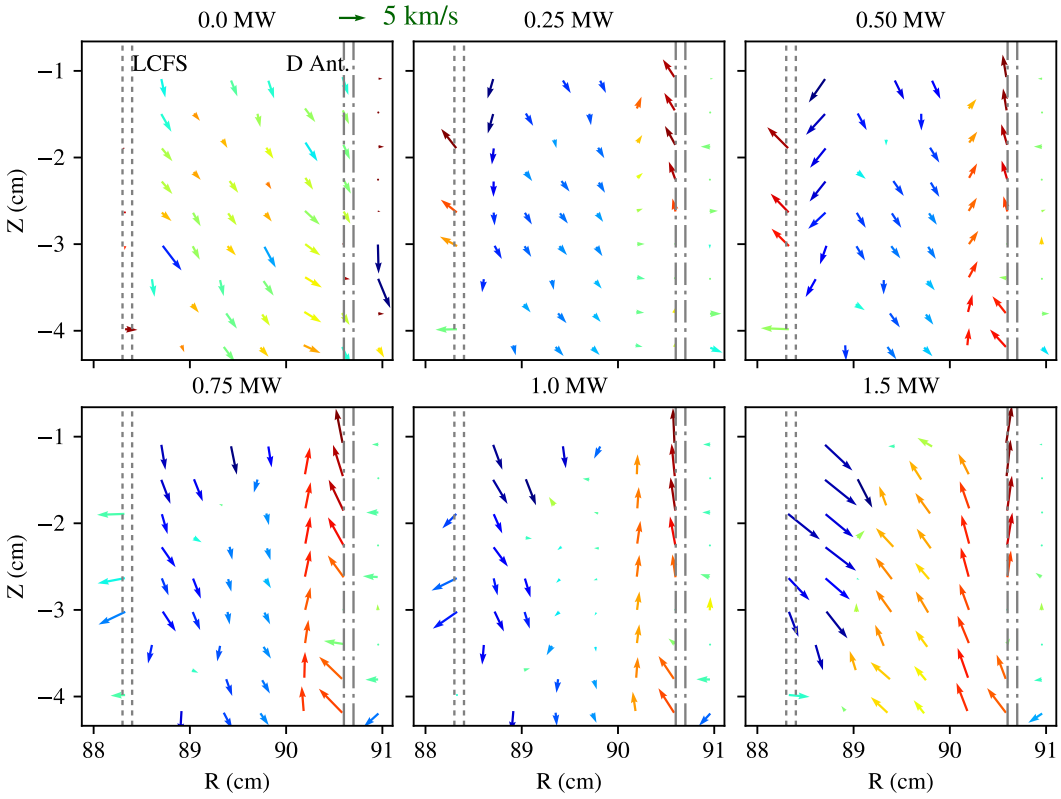


**Figure 4.2**: Equilibrium velocity fields in the SOL region at different ICRF heating powers. Red arrows point in the EDD (upward); blue arrows point in the IDD (downward). Black dotted lines indicate the position of the LCFS; black dash-dot lines indicate the position of the D antenna. The green arrow at top of the figure indicates the scale of $V = 5$ km/s. Clearly, the poloidal flows near antenna change direction as the ICRF power is increased.

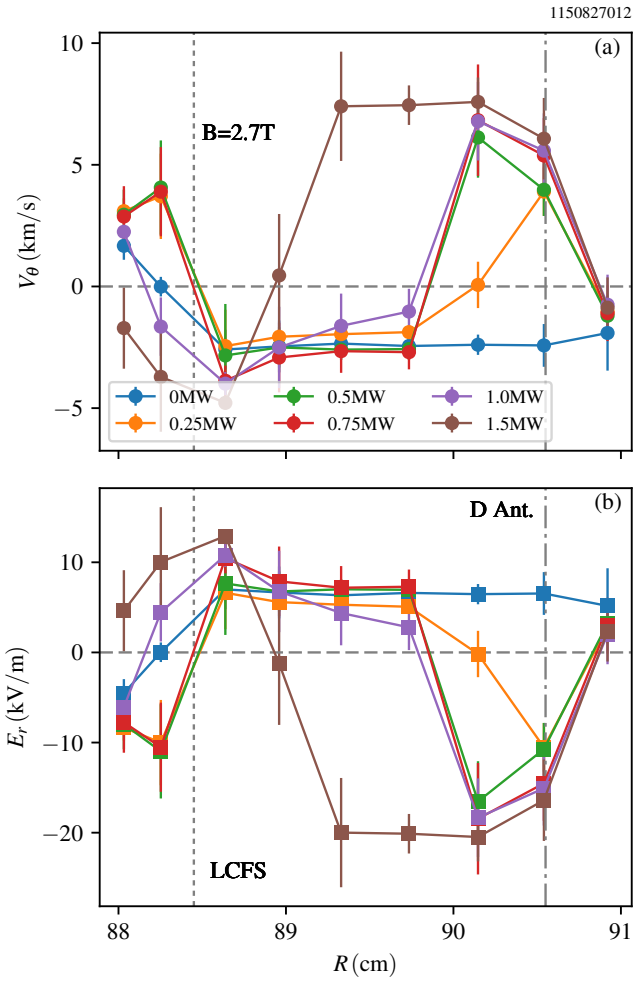


**Figure 4.3**: Equilibrium profiles of (a) poloidal velocity $V_\theta(r)$ and (b) radial electric field $E_r(r) = -V_\theta B_\varphi$, at different ICRF heating powers launched by the D antenna. The toroidal magnetic field is $B_\varphi = 2.7\,\mathrm{T}$. Black dotted lines indicate the position of the LCFS; black dash-dot lines indicate the position of the D antenna. The RF-induced $E_r$ field increases as RF power is raised.

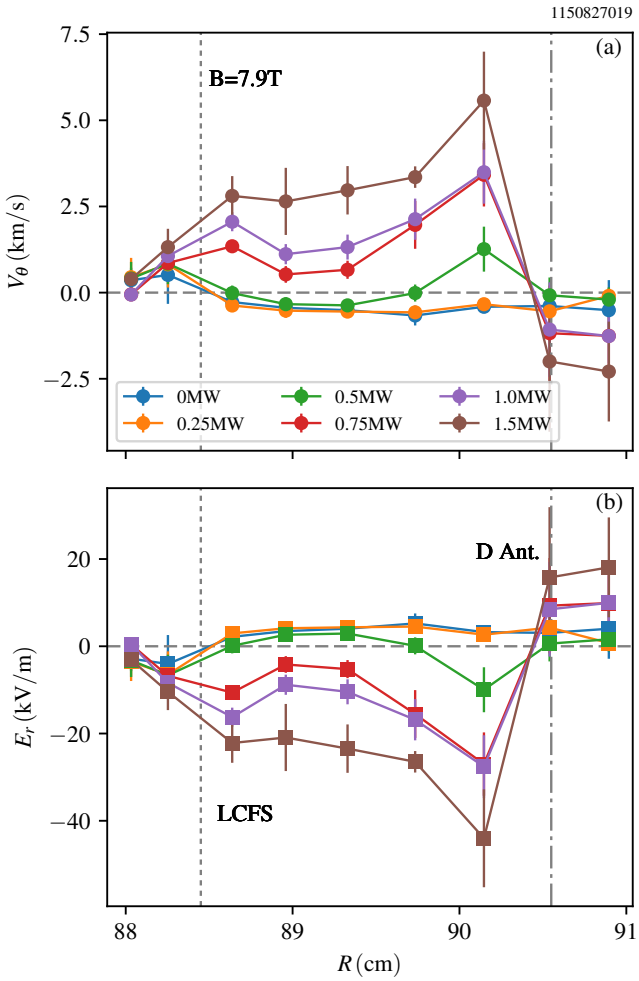


**Figure 4.4**: Profiles of (a) poloidal velocity $V_\theta(r)$ and (b) radial electric field $E_r(r) = -V_\theta B_\varphi$, at different ICRF heating powers launched by the D antenna. The toroidal magnetic field is $B_\varphi = 7.9\,\mathrm{T}$. Black dotted lines indicate the position of the LCFS; black dash-dot lines indicate the position of the D antenna. The RF-induced $E_r$ field increases as RF power is raised.

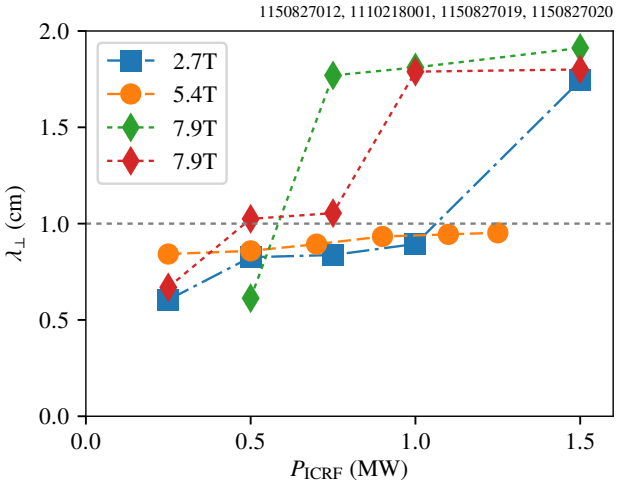


**Figure 4.5**: The radial width of the RF-induced radial electric field, $E_r$, compared against the ICRF heating powers, at different toroidal magnetic field.

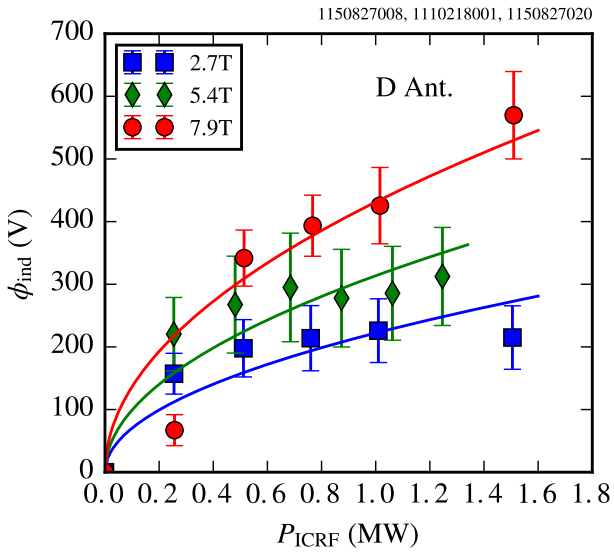


**Figure 4.6**: Peak values of RF-induced plasma potential as a function of ICRF heating power at three different toroidal magnetic fields. Markers represent experimental estimates and solid lines represent their best fits in the form of $P_{\mathrm{ICRF}}^{1/2}$. The error bars indicate two standard errors of the mean values.

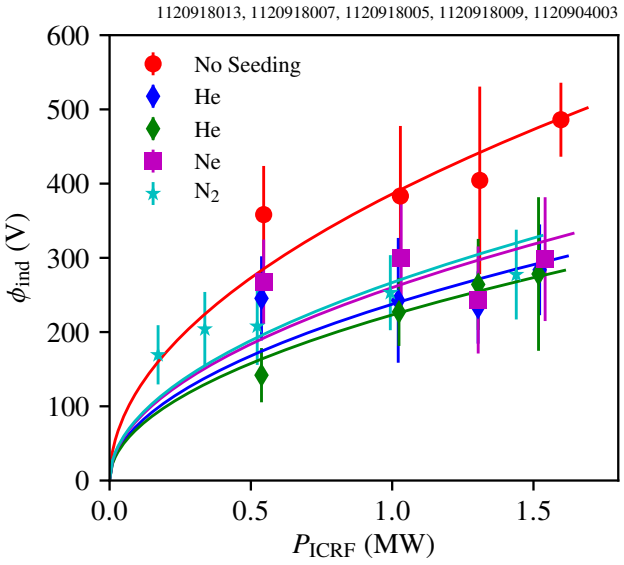


**Figure 4.7**: Peak values of RF-induced plasma potential as a function of ICRF heating power of D antenna with different species of low-Z impurity seeding. $B_\varphi = 5.4\,\mathrm{T}$ and $I_p = 0.8\,\mathrm{MA}$. Markers represent experimental estimates and solid lines represent their best fits in the form of $P_{\mathrm{ICRF}}^{1/2}$.

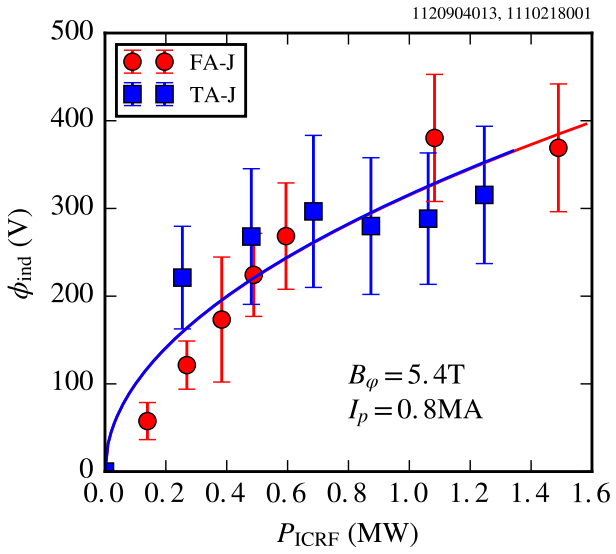


**Figure 4.8**: Peak values of the RF-induced sheath potential as a function of ICRF heating power by FA and TA antenna. Markers represent experimental estimates and solid lines represent their best fits in the form of $P_{\mathrm{ICRF}}^{1/2}$.

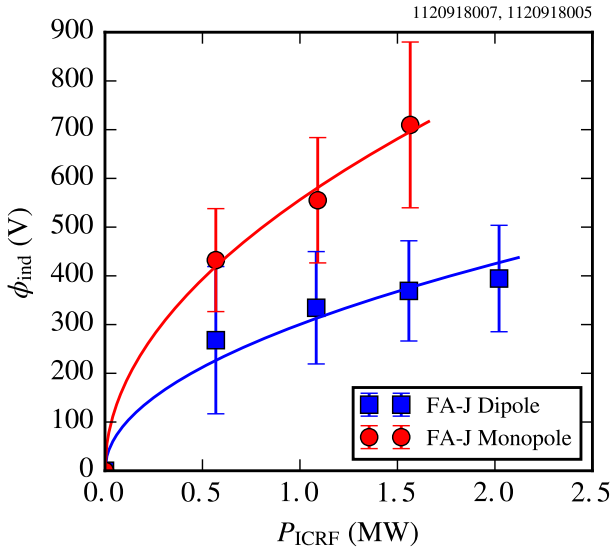


**Figure 4.9**: Peak values of RF-induced sheath potential as a function of ICRF heating power in dipole and monopole phasing. $B_\varphi = 5.4\,\mathrm{T}$ and $I_p = 0.8\,\mathrm{MA}$. Markers represent experimental estimates and solid lines represent their best fits in the form of $P_{\mathrm{ICRF}}^{1/2}$.

# Chapter 5

# Summary and Future Outlook

In this chapter, we will first summarize the key objectives and conclusions of each section, and then discuss the implications of the work and make suggestions for the future work.

## 5.1 Edge Shear Flows near the Density Limit

The Chapter 2 of this dissertation is devoted to the topic of the Greenwald density limit in toroidally confined plasmas. As has been introduced in early Chapters, the density limit is an operation limit observed in confined toroidal plasmas. The empirical scaling for the density limit is written as

$$n_G = \frac{I_p}{\pi a^2},$$

where $n_G$ is the line-averaged density in units of $10^{20}$ m$^{-3}$, $I_p$ is the plasma current in the unit of MA, and $a$ is the minor radius of plasma in the unit of meter. Raising the plasma density $\bar{n}$ to $n_G$ usually leads to degradation of plasma confinement, or even disruption when $n_G$ is exceeded.

The most common existing models used to explain this disruptive limit is the

radiative model, in which the radiative heat loss due to increased impurity content dominates the power balance inside an magnetic island, resulting in edge cooling and thus an increased resistivity, causing the toroidal current channel to shrink. The current shrinkage then leads to an increased current density gradient and the onset of resistive MHD instabilities. But this mechanism fails to explain the cases in which the density limit happened without a larger magnetic island. On the other hand, it has long been observed that enhanced edge particle flux occurs in advance of any MHD activity change [BYB$^+$91]. Since the particle transport is always mediated by the sheared flow in plasmas, the increased particle flux leads us to the questions:

- Does the zonal flow collapse when the density limit is approached?
- If so, is the damping of zonal flow due to collisional process or to reduced turbulent drive?

To answer these questions, we performed shot-by-shot density scanning experiments on HL-2A tokamak, and measured the evolution of the zonal flow and turbulent Reynolds stress at different plasma densities.

The results show that as the line-averaged density increases, the density gradient inside the separatrix increases sharply. The electron temperature profile and poloidal phase velocity of turbulent fluctuations drop as the density increases toward the Greenwald limit. Meanwhile, both the low-frequency zonal flow shearing rate $\omega_{\rm sh}$ and the Reynolds power $\mathcal{P}^{Re}$ are observed to decrease in high collisionality discharges. These observations suggest that the low-frequency zonal flow is not only subject to the collisional damping but also has lower turbulent drive in higher density plasmas. As a result, ZFs cannot regulate turbulent transport.

The frequency-resolved nonlinear energy transfer analysis shows that GAMs have larger effective nonlinear growth rate $\gamma_{\rm NL}^{\rm GAM}$ at higher $\bar{n}_e/n_G$ values. However, $\omega_{\rm GAM}$ is

still less than the shearing rate of mean flows by a factor of $3-5$. Furthermore, the increase of the cross-correlation between $\tilde{n}_e$ and $\tilde{v}_r$, as well as the amplitude of $\tilde{n}_e$, results in substantial enhancement of particle transport in high collisionality plasmas, increasing edge cooling and therefore driving the strong MHD instabilities that lead to disruptions. The adiabatic parameter, $k_{\parallel}^2 v_{t,e}^2/\omega\nu_e$, drops significantly from about 3 to 0.5 as $\bar{n}_e/n_G$ increases from 0.3 to 0.8. These findings suggest that the increased collisionality may not only damp the low-frequency zonal flow via Coulomb collisions, but also increase the non-adiabatic electron response and hence increase particle transport.

A key finding here is that the turbulent Reynolds stress collapses with decreasing adiabaticity, $\alpha = k_{\parallel}^2 v_{t,e}^2/\omega\nu_e$, and therefore the ambient turbulence cannot drive the low-frequency zonal flow even though the turbulent fluctuations increase. This picture is opposite to the mechanism of *L*-*H* transition physics where the zonal flows are driven by the drift wave turbulence via the Reynolds force and in turn suppress the turbulent transport [DIIH05, TXD$^+$13, TCD$^+$16]. To achieve the *L*-*H* transition, we essentially rise the heating power, effectively increasing the adiabatic parameter.

In this study, we tried shot-by-shot density scanning experiments. However, it would be benefit to carry out dynamic studies using perturbative techniques such as density and/or heating power modulation. Also, more detailed measurement edge profiles, including edge sheared flows, density and temperature, should be obtained to assess the entire physics picture, i.e. the evolution from reduced zonal flows to enhanced particle flux and thus the onset of MHD instabilities.

Moreover, our measurements in this study are focused on electrostatic fluctuations, i.e. the Reynolds stress $\langle\tilde{v}_r\tilde{v}_\theta\rangle$, and do not account for the effect of magnetic stress $\langle\tilde{B}_r\tilde{B}_\theta\rangle$ on the driving force for zonal flows near the Greenwald limit. The divergence of the magnetic stress is known to induce a force on plasmas. The signs of the divergences of the Reynolds stress and magnetic stress are opposite for the drift-Alfven waves

[DIIH05, KG08], resulting in a lower driving force for the zonal flows in the limit of finite $\hat{\beta}$. As reported in both experiments [LHM$^+$05] and numerical simulations [RDZ98], electromagnetic fluid drift turbulence grows and becomes the dominant modes controlling edge transport when the density limit is approached.

In present study, the MHD ballooning parameter, $\alpha_{\mathrm{MHD}} = \frac{q^2 R}{L_{Pe}}\beta$ with $\beta = \frac{4\mu_0 P_{e0}}{B^2}$, increases from about 0.1 to 0.3 at the edge as $\bar{n}_e/n_G$ is raised from 0.3 to 0.8. Therefore, magnetic fluctuations are supposed to increase, and their effects on shear flows should be considered. Nonetheless, even without any direct measurement of electromagnetic effects, the reduction in turbulent force for the zonal flows at higher densities suggests that zonal flow is an important element in density limit physics.

## 5.2 Intrinsic Flows in Cylindrical Plasmas

In addition to the zonal flows, which are toroidally symmetrical transverse flows in plasmas, the parallel shear flows can also regulate the turbulent transport and improve MHD stabilities. A phenomenon called intrinsic parallel flow has been identified in magnetically confined plasmas [SBd$^+$07, dRB$^+$07, MBB$^+$11, RHD$^+$11, DKG$^+$13, IR14, Ric16], i.e. the plasma rotates without any input of toroidal momentum. This intrinsic flow can be large [RICd$^+$07, MBB$^+$11, Ric16], and thus there is strong interest in knowing whether there is sufficient toroidal torque in future fusion devices to affect confinement and MHD stability.

In this study, we carried out experiments in a linear device, the Controlled Shear Decorrelation eXperiment (CSDX), and seek to answer the following questions: (1) Are parallel flows in a linear device driven by an intrinsic mechanism? (2) What is the effect of turbulent stress on mean parallel flow? (3) How do the self-generated transverse and parallel flows interact with each other?

Detailed measurements of plasma profiles, including flows and turbulent Reynolds stresses in both axial and azimuthal directions, have been performed in a helicon source linear magnetized plasma deviceÃćÂĂÂŤCSDX. The probe measurements reveal that both axial flow shearing rate and its turbulent drive (Reynolds force/power) increase with increasing density gradient as the $B$ field is raised. The parallel Reynolds stress is induced by the density gradient and becomes the primary source driving the axial flow as the density gradient is steepened.

A simple dynamical symmetry breaking model is used to explore the origin of the intrinsic axial flow in plasmas with uniform magnetic field. In this model, the imbalance of the spectral correlator, $\langle k_\theta k_z \rangle = \sum_{\mathbf{k}} k_\theta k_z \left|\hat{\phi}_{\mathbf{k}}\right|^2 \sim \langle \tilde{v}_r \tilde{v}_z \rangle$, is triggered by seed axial shear flow, leading to negative diffusivity and self-amplification of the axial shear flow via the modulational instability. The 2D joint PDF of radial and axial velocity fluctuations, $\mathsf{P}(\tilde{v}_r, \tilde{v}_z)$, has been calculated and used to represent the spectral correlator $\langle k_\theta k_z \rangle$. $\mathsf{P}(\tilde{v}_r, \tilde{v}_z)$ is highly tilted and anisotropic at higher density gradient and axial velocity shear. Furthermore, the residual stress is linearly proportional to the density gradient and is also positively related to the axial flow shear $V_z'$. These observations are consistent with the prediction by the dynamical symmetry breaking mechanism.

On the other hand, the turbulence-driven azimuthal flow exhibits a bifurcation during the B field scan: before the transition ($B < 800$ G), the azimuthal velocity shear $V_\theta'$ and Reynolds power $\mathcal{P}_\theta^{Re}$ increase with the B field; after 800 G, $\mathcal{P}_\theta^{Re}$ collapses and $V_\theta'$ starts to fall correspondingly. Before the transition, the rises in both the axial velocity shear $V_z'$ and axial Reynolds power $\mathcal{P}_z^{Re}$ are associated with increasing azimuthal velocity shear $V_\theta'$, suggesting that $V_\theta'$ plays an important role in triggering the intrinsic axial flow. However, the azimuthal Reynolds power $\mathcal{P}_\theta^{Re}$ is about 10 times larger than the axial counterpart $\mathcal{P}_z^{Re}$. Therefore, the direct energy exchange between axial and azimuthal flows is relatively negligible. However, the existing dynamical symmetry breaking model

does not account for the effect of $V_E'$ on intrinsic axial flow. It would be more convincing to include the interaction between the azimuthal flow, drive-wave turbulence and the axial flow in future modeling.

## 5.3 ICRF-induced Plasma Flows and Potentials

Chapter 4 is focused on characterizing the ICRF-induced plasma flows and potentials in scrape-off layer of Alcator C-Mod tokamak. While ICRF-heating has been an efficient and reliable heating method on C-Mod, plasmas with strong ICRF heating and high-Z PFCs have often suffered from increased core impurity concentrations that result from the ICRF. Enhanced sputtering due to large ICRF-induced plasma potentials on open field-lines has long been thought of as the primary cause for the increased impurity concentrations. It is therefore of great importance to characterize the response of enhanced plasma flows and potentials to the ICRF antenna.

In this study, the ICRF-induced plasma potentials and radial electric fields have been investigated using gas-puffing imaging techniques. The equilibrium plasma flows that advect turbulent structures in SOL region have been calculated using TDE techniques. The results of radial profiles from TDE analysis are in agreement with previous analysis based on poloidal phase velocity estimations. The TDE techniques are able to show 2D distributions of RF-induced $E_r$ and $\phi_{\rm ind}$, and will be beneficial for future studies of RF physics.

The large convective cells induced by the RF sheath electric field are observed in the vicinity of the active ICRF antenna. The radial width of this field is $1-2\,$cm and *increases* as the toroidal magnetic field is raised. In most discharges, the peak values of the ICRF-induced potential, $\phi_{\rm ind}$, scale as $P_{\rm ICRF}^{1/2}$ and are proportional to the strength of the toroidal magnetic field. In particular, $\phi_{\rm ind} \approx 600\,$V is observed at $B_\varphi = 7.9\,$T. However,

$\phi_{\mathrm{ind}}$ was decreased by sufficiently strong low-Z impurity seeding, and the potentials began to deviate from the $P_{\mathrm{ICRF}}^{1/2}$ scaling. The sheath potential induced by the FA antenna was similar to that by the TA antenna, in disagreement with the modeling which indicate that the FA antenna should produce lower integrated $E_{\|}$. In addition, while monopole FA antenna modeling predicts lower integrated $E_{\|}$ than dipole phasing modeling, it induced substantially higher sheath potential in our experiments. These discrepancies between the observations and the modeling may be attributed to the RF image currents on the FA antenna box structures, but further work is needed to test these conjectures.

The large $\phi_{\mathrm{ind}}$ at high toroidal magnetic field is expected to enhance the sputtering yields on PFCs adjacent to the active antenna. Therefore, new designs of ICRF antenna should try to minimize the local RF-$E_{\|}$ fields and related plasma-material interactions close to the antenna.

Finally, the measurements of the radial broadening of the RF sheath structure at different magnetic field do not support the scaling $\lambda_{\perp} \sim \left(L_{\|}\rho_{\mathrm{ci}}/2\right)^{1/2}$ predicted by theoretical modeling. Additional theory and experimental work is required to clarify the underlying physics.

# Bibliography


[BAB+17] V. Bobkov, D. Aguiam, R. Bilato, S. Brezinsek, L. Colas, H. Faugel, H. FÃČÂijnfgelder, A. Herrmann, J. Jacquot, A. Kallenbach, D. Milanesio, R. Maggiora, R. Neu, J.-M. Noterdaeme, R. Ochoukov, S. Potzel, T. PÃČÂijtterich, A. Silva, W. Tierens, A. Tuccilo, O. Tudisco, Y. Wang, Q. Yang, W. Zhang, ASDEX Upgrade Team, and the EUROfusion MST1 Team. Making icrf power compatible with a high-z wall in asdex upgrade. *Plasma Physics and Controlled Fusion*, 59(1):014022, 2017.

[BBD+16] V. Bobkov, F. Braun, R. Dux, A. Herrmann, H. Faugel, H. FÃČÂijnfgelder, A. Kallenbach, R. Neu, J.-M. Noterdaeme, R. Ochoukov, T. PÃČÂijtterich, A. Tuccilo, O. Tudisco, Y. Wang, Q. Yang, and ASDEX Upgrade team. First results with 3-strap icrf antennas in asdex upgrade. *Nuclear Fusion*, 56(8):084001, 2016.

[BDT90] H. Biglari, P. H. Diamond, and P. W. Terry. Influence of sheared poloidal rotation on edge turbulence. *Physics of Fluids B: Plasma Physics*, 2(1):1–4, 1990.

[BK63] H. S. Butler and G. S. Kino. Plasma sheath formation by radio-frequency fields. *Physics of Fluids*, 6(9):1346–1355, 1963.

[Boe64] F. Boeschoten. Review of experiments on the diffusion of plasma across a magnetic field. *Journal of Nuclear Energy. Part C, Plasma Physics, Accelerators, Thermonuclear Research*, 6(4):339, 1964.

[BPW+07] P. Bonoli, R. Parker, S. J. Wukitch, Y. Lin, M. Porkolab, J. C. Wright, E. Edlund, T. Graves, L. Lin, and J. Liptac. Wave-particle studies in the ion cyclotron and lower hybrid ranges of frequencies in alcator c-mod. *Fusion Science and Technology*, 51(3):401–436, 2007.

[BRSS13] G. Birkenmeier, M. Ramisch, B. Schmid, and U. Stroth. Experimental evidence of turbulent transport regulation by zonal flows. *Phys. Rev. Lett.*, 110:145004, Apr 2013.

[BSB+10] J. W. Berkery, S. A. Sabbagh, R. Betti, B. Hu, R. E. Bell, S. P. Gerhardt, J. Manickam, and K. Tritz. Resistive wall mode instability at intermediate plasma rotation. *Phys. Rev. Lett.*, 104:035003, Jan 2010.

[BTA+05] M. J. Burin, G. R. Tynan, G. Y. Antar, N. A. Crocker, and C. Holland. On the transition to drift turbulence in a magnetized plasma column. *Physics of Plasmas*, 12(5):052320, 2005.

[Bur97] K. H. Burrell. Effects of e × b velocity shear and magnetic shear on turbulence and transport in magnetic confinement devices. *Physics of Plasmas*, 4(5):1499–1518, 1997.

[Bur06] K. H. Burrell. Turbulence behaviour in the presence of transport barriers. *Plasma Physics and Controlled Fusion*, 48(5A):A347, 2006.

[BYB+91] D. L. Brower, C. X. Yu, R. V. Bravenec, H. Lin, N. C. Luhmann, W. A. Peebles, C. P. Ritz, B. A. Smith, A. J. Wootton, Z. M. Zhang, and S. J. Zhao. Confinement degradation and enhanced microturbulence as long-time precursors to high-density-limit tokamak disruptions. *Phys. Rev. Lett.*, 67:200–203, Jul 1991.

[CBJ+00] P. M. Cox, R. A. Betts, C. D. Jones, S. A. Spall, and I. J. Totterdell. Acceleration of global warming due to carbon-cycle feedbacks in a coupled climate model. *Nature*, 408(6809):184–187, 11 2000.

[CDF+13] I. Cziegler, P. H. Diamond, N. Fedorczak, P. Manz, G. R. Tynan, M. Xu, R. M. Churchill, A. E. Hubbard, B. Lipschultz, J. M. Sierchio, J. L. Terry, and C. Theiler. Fluctuating zonal flows in the i-mode regime in alcator c-moda). *Physics of Plasmas*, 20(5), 2013.

[CHH+17] I. Cziegler, A. E. Hubbard, J. W. Hughes, J. L. Terry, and G. R. Tynan. Turbulence nonlinearities shed light on geometric asymmetry in tokamak confinement transitions. *Phys. Rev. Lett.*, 118:105003, Mar 2017.

[CJH+12] L. Colas, J. Jacquot, S. Heuraux, E. Faudot, K. CrombÃČÂľ, V. Kyrytsya, J. Hillairet, and M. Goniche. Self consistent radio-frequency wave propagation and peripheral direct current plasma biasing: Simplified three dimensional non-linear treatment in the ÃćÂĂÂIJwide sheathÃćÂĂÂİ asymptotic regime. *Physics of Plasmas*, 19(9):092505, 2012.

[CLK+17] L. Colas, L.-F. Lu, A. KÃĚÂŹivskÃČÂą, J. Jacquot, J. Hillairet, W. Helou, M. Goniche, S. Heuraux, and E. Faudot. Spatial proximity effects on the excitation of sheath rf voltages by evanescent slow waves in the ion cyclotron range of frequencies. *Plasma Physics and Controlled Fusion*, 59(2):025014, 2017.

[CTD+14] I. Cziegler, G. R. Tynan, P. H. Diamond, A. E. Hubbard, J. W. Hughes, J. Irby, and J. L. Terry. Zonal flow production in the lÃćÂĂÂŞh transition in alcator c-mod. *Plasma Physics and Controlled Fusion*, 56(7):075013, 2014.

[CTD+15] I. Cziegler, G. Tynan, P. Diamond, A. Hubbard, J. Hughes, J. Irby, and J. Terry. Nonlinear transfer in heated l-modes approaching the lÃćÂĂÂŞh transition threshold in alcator c-mod. *Nuclear Fusion*, 55(8):083007, 2015.

[CTHL10] I. Cziegler, J. L. Terry, J. W. Hughes, and B. LaBombard. Experimental studies of edge turbulence and confinement in alcator c-mod. *Physics of Plasmas*, 17(5), 2010.

[CTW+12] I. Cziegler, J. L. Terry, S. J. Wukitch, M. L. Garrett, C. Lau, and Y. Lin. Ion-cyclotron range of frequencies in the scrape-off-layer: fine structure radial electric fields. *Plasma Physics and Controlled Fusion*, 54(10):105019, 2012.

[CY02] J. W. Connor and S. You. On the density limit in tokamaks. *Plasma Physics and Controlled Fusion*, 44(1):121, 2002.

[DDD+13] X. Duan, X. Ding, J. Dong, L. Yan, Y. Liu, Y. Huang, X. Song, X. Zou, M. Xu, Q. Yang, D. Liu, J. Rao, W. Xuan, L. Chen, W. Mao, Q. Wang, Z. Cao, B. Li, J. Cao, G. Lei, J. Zhang, X. Li, W. Chen, K. Zhao, W. Xiao, C. Chen, D. Kong, M. Isobe, S. Morita, J. Cheng, S. Chen, C. Cui, Z. Cui, W. Deng, Y. Dong, B. Feng, W. Hong, M. Huang, X. Ji, G. Li, H. Li, Q. Li, C. Liu, J. Peng, B. Shi, Y. Wang, L. Yao, L. Yao, D. Yu, L. Yu, B. Yuan, J. Zhou, Y. Zhou, W. Zhong, G. Tynan, P. Diamond, C. Yu, Y. Liu, and the HL-2A Team. An overview of recent hl-2a experiments. *Nuclear Fusion*, 53(10):104009, 2013.

[DIIH05] P. H. Diamond, S.-I. Itoh, K. Itoh, and T. S. Hahm. Zonal flows in plasmaÃćÂĂÂŤa review. *Plasma Physics and Controlled Fusion*, 47(5):R35, 2005.

[DKG+13] P. Diamond, Y. Kosuga, O. Gürcan, C. McDevitt, T. Hahm, N. Fedorczak, J. Rice, W. Wang, S. Ku, J. Kwon, G. Dif-Pradalier, J. Abiteboul, L. Wang, W. Ko, Y. Shi, K. Ida, W. Solomon, H. Jhang, S. Kim, S. Yi, S. Ko, Y. Sarazin, R. Singh, and C. Chang. An overview of intrinsic torque and momentum transport bifurcations in toroidal plasmas. *Nuclear Fusion*, 53(10):104019, 2013.

[DMG+09] P. Diamond, C. McDevitt, O. Gurcan, T. Hahm, W. X. Wang, E. Yoon, I. Holod, Z. Lin, V. Naulin, and R. Singh. Physics of non-diffusive turbulent transport of momentum and the origins of spontaneous rotation in tokamaks. *Nuclear Fusion*, 49(4):045002, 2009.

[dRB+07] J. S. deGrassie, J. E. Rice, K. H. Burrell, R. J. Groebner, and W. M. Solomon. Intrinsic rotation in diii-d. *Physics of Plasmas*, 14(5):056115, 2007.

[FCHG10] E. Faudot, L. Colas, S. Heuraux, and J. P. Gunn. Broadening of rectified potential structures induced by rf currents in a magnetized plasma: Application to iter scrape-off-layer. *Physics of Plasmas*, 17(4), 2010.

[Fuj09] A. Fujisawa. A review of zonal flow experiments. *Nuclear Fusion*, 49(1):013001, 2009.

[GBB+14] M. Greenwald, A. Bader, S. Baek, M. Bakhtiari, H. Barnard, W. Beck, W. Bergerson, I. Bespamyatnov, P. Bonoli, D. Brower, D. Brunner, W. Burke, J. Candy, M. Churchill, I. Cziegler, A. Diallo, A. Dominguez, B. Duval, E. Edlund, P. Ennever, D. Ernst, I. Faust, C. Fiore, T. Fredian, O. Garcia, C. Gao, J. Goetz, T. Golfinopoulos, R. Granetz, O. Grulke, Z. Hartwig, S. Horne, N. Howard, A. Hubbard, J. Hughes, I. Hutchinson, J. Irby, V. Izzo, C. Kessel, B. LaBombard, C. Lau, C. Li, Y. Lin, B. Lipschultz, A. Loarte, E. Marmar, A. Mazurenko, G. McCracken, R. McDermott, O. Meneghini, D. Mikkelsen, D. Mossessian, R. Mumgaard, J. Myra, E. Nelson-Melby, R. Ochoukov, G. Olynyk, R. Parker, S. Pitcher, Y. Podpaly, M. Porkolab, M. Reinke, J. Rice, W. Rowan, A. Schmidt, S. Scott, S. Shiraiwa, J. Sierchio, N. Smick, J. A. Snipes, P. Snyder, B. Sorbom, J. Stillerman, C. Sung, Y. Takase, V. Tang, J. Terry, D. Terry, C. Theiler, A. Tronchin-James, N. Tsujii, R. Vieira, J. Walk, G. Wallace, A. White, D. Whyte, J. Wilson, S. Wolfe, G. Wright, J. Wright, S. Wukitch, and S. Zweben. 20 years of research on the alcator c-mod tokamak. *Physics of Plasmas*, 21(11), 2014.

[GBDA+16] D. A. Gates, D. P. Brennan, L. Delgado-Aparicio, Q. Teng, and R. B. White. Thermo-resistive disruptions and the tokamak density limit. *Physics of Plasmas*, 23(5):056113, 2016.

[GDA12] D. A. Gates and L. Delgado-Aparicio. Origin of tokamak density limit scalings. *Phys. Rev. Lett.*, 108:165004, Apr 2012.

[GDAW13] D. Gates, L. Delgado-Aparicio, and R. White. Physics of radiation-driven islands near the tokamak density limit. *Nuclear Fusion*, 53(6):063008, 2013.

[GDH+10] O. D. Gürcan, P. H. Diamond, P. Hennequin, C. J. McDevitt, X. Garbet, and C. Bourdelle. Residual parallel reynolds stress due to turbulence intensity gradient in tokamak plasmas. *Physics of Plasmas*, 17(11):112309, 2010.

[GDHS07] O. D. Gürcan, P. H. Diamond, T. S. Hahm, and R. Singh. Intrinsic rotation and electric field shear. *Physics of Plasmas*, 14(4):042306, 2007.

[GHP+06] B. GonÃČÂğalves, C. Hidalgo, M. A. Pedrosa, R. O. Orozco, E. Sánchez, and C. Silva. Role of turbulence on edge momentum redistribution in the tj-ii stellarator. *Phys. Rev. Lett.*, 96:145001, Apr 2006.

[Gre02] M. Greenwald. Density limits in toroidal plasmas. *Plasma Physics and Controlled Fusion*, 44(8):R27, 2002.

[GSJ+02] A. M. Garofalo, E. J. Strait, L. C. Johnson, R. J. La Haye, E. A. Lazarus, G. A. Navratil, M. Okabayashi, J. T. Scoville, T. S. Taylor, and A. D. Turnbull. Sustained stabilization of the resistive-wall mode by plasma rotation in the diii-d tokamak. *Phys. Rev. Lett.*, 89:235001, Nov 2002.

[GTW+88] M. Greenwald, J. Terry, S. Wolfe, S. Ejima, M. Bell, S. Kaye, and G. Neilson. A new look at density limits in tokamaks. *Nuclear Fusion*, 28(12):2199, 1988.

[GW12] M. Garrett and S. Wukitch. Mitigation of radio frequency sheaths through magnetic field-aligned icrf antenna design. *Fusion Engineering and Design*, 87(9):1570 – 1575, 2012.

[HBB+94] I. H. Hutchinson, R. Boivin, F. Bombarda, P. Bonoli, S. Fairfax, C. Fiore, J. Goetz, S. Golovato, R. Granetz, M. Greenwald, and the Alcator C-MOD Team. First results from alcator-c-mod. *Physics of Plasmas (1994-present)*, 1(5):1511–1518, 1994.

[HH76] F. L. Hinton and R. D. Hazeltine. Theory of plasma transport in toroidal confinement systems. *Rev. Mod. Phys.*, 48:239–308, Apr 1976.

[Hor99] W. Horton. Drift waves and transport. *Rev. Mod. Phys.*, 71:735–778, Apr 1999.

[Hut08] I. H. Hutchinson. Ion collection by oblique surfaces of an object in a transversely flowing strongly magnetized plasma. *Phys. Rev. Lett.*, 101:035004, Jul 2008.

[HYJ+06] C. Holland, J. H. Yu, A. James, D. Nishijima, M. Shimada, N. Taheri, and G. R. Tynan. Observation of turbulent-driven shear flow in a cylindrical laboratory plasma device. *Phys. Rev. Lett.*, 96:195002, May 2006.

[IKK+16] S. Inagaki, T. Kobayashi, Y. Kosuga, S. I. Itoh, T. Mitsuzono, Y. Nagashima, H. Arakawa, T. Yamada, Y. Miwa, N. Kasuya, M. Sasaki, M. Lesur, A. Fujisawa, and K. Itoh. A concept of cross-ferroic plasma turbulence. *Scientific Reports*, 6:22189, 02 2016.

[IMM+95] K. Ida, Y. Miura, T. Matsuda, K. Itoh, S. Hidekuma, and S.-I. Itoh. Evidence for a toroidal-momentum-transport nondiffusive term from the jft-2m tokamak. *Phys. Rev. Lett.*, 74:1990–1993, Mar 1995.

[IR14] K. Ida and J. Rice. Rotation and momentum transport in tokamaks and helical systems. *Nuclear Fusion*, 54(4):045001, 2014.

[Jas72] D. L. Jassby. Transverse velocity shear instabilities within a magnetically confined plasma. *The Physics of Fluids*, 15(9):1590–1604, 1972.

[KG08] R. G. Kleva and P. N. Guzdar. Loss of confinement at the density limit due to the suppression of stabilizing zonal flows by magnetic turbulence. *Physics of Plasmas*, 15(8):082307, 2008.

[KHY+91] Y. Kamada, N. Hosogane, R. Yoshino, T. Hirayama, and T. Tsunematsu. Study of the density limit with pellet fuelling in jt-60. *Nuclear Fusion*, 31(10):1827, 1991.

[KIK+16] T. Kobayashi, S. Inagaki, Y. Kosuga, M. Sasaki, Y. Nagashima, T. Yamada, H. Arakawa, N. Kasuya, A. Fujisawa, S.-I. Itoh, and K. Itoh. Structure formation in parallel ion flow and density profiles by cross-ferroic turbulent transport in linear magnetized plasma. *Physics of Plasmas*, 23(10):102311, 2016.

[LBG+01] B. LaBombard, R. L. Boivin, M. Greenwald, J. Hughes, B. Lipschultz, D. Mossessian, C. S. Pitcher, J. L. Terry, S. J. Zweben, and the Alcator C-Mod Team. Particle transport in the scrape-off layer and its relationship to discharge density limit in alcator c-mod. *Physics of Plasmas*, 8(5):2107–2117, 2001.

[LBGP04] Y. Liu, A. Bondeson, Y. Gribov, and A. Polevoi. Stabilization of resistive wall modes in iter by active feedback and toroidal rotation. *Nuclear Fusion*, 44(2):232, 2004.

[LDXT16] J. C. Li, P. H. Diamond, X. Q. Xu, and G. R. Tynan. Dynamics of intrinsic axial flows in unsheared, uniform magnetic fields. *Physics of Plasmas*, 23(5):052311, 2016.

[LDY+05] Y. Liu, X. Ding, Q. Yang, L. Yan, D. Liu, W. Xuan, L. Chen, X. Song, Z. Cao, J. Zhang, W. Mao, C. Zhou, X. Li, S. Wang, J. Yan, M. Bu, Y. Chen, C. Cui, Z. Cui, Z. Deng, W. Hong, H. Hu, Y. Huang, Z. Kang, B. Li, W. Li, F. Li, G. Li, H. Li, Q. Li, Y. Li, Z. Li, Y. Liu, Z. Liu, C. Luo, X. Mao, Y. Pan, J. Rao, K. Shao, X. Song, M. Wang, M. Wang, Q. Wang, Z. Xiao, Y. Xie, L. Yao, L. Yao, Y. Zheng, G. Zhong, Y. Zhou, and C. Pan. Recent advances in the hl-2a tokamak experiments. *Nuclear Fusion*, 45(10):S239, 2005.

[LHL+99] Z. Lin, T. S. Hahm, W. W. Lee, W. M. Tang, and P. H. Diamond. Effects of collisional zonal flow damping on turbulent transport. *Phys. Rev. Lett.*, 83:3645–3648, Nov 1999.

[LHM+05] B. LaBombard, J. Hughes, D. Mossessian, M. Greenwald, B. Lipschultz, J. Terry, and the Alcator C-Mod Team. Evidence for electromagnetic fluid drift turbulence controlling the edge plasma state in the alcator c-mod tokamak. *Nuclear Fusion*, 45(12):1658, 2005.

[Lie85] P. C. Liewer. Measurements of microturbulence in tokamaks and comparisons with theories of turbulence and anomalous transport. *Nuclear Fusion*, 25(5):543, 1985.

[LLY+08] T. Lan, A. D. Liu, C. X. Yu, L. W. Yan, W. Y. Hong, K. J. Zhao, J. Q. Dong, J. Qian, J. Cheng, D. L. Yu, and Q. W. Yang. Spectral characteristics of geodesic acoustic mode in the hl-2a tokamak. *Plasma Physics and Controlled Fusion*, 50(4):045002, 2008.

[LPL+01] B. Lipschultz, D. Pappas, B. LaBombard, J. Rice, D. Smith, and S. Wukitch. A study of molybdenum influxes and transport in alcator c-mod. *Nuclear Fusion*, 41(5):585, 2001.

[LSB+12] P. Lang, W. Suttrop, E. Belonohy, M. Bernert, R. M. Dermott, R. Fischer, J. Hobirk, O. Kardaun, G. Kocsis, B. Kurzan, M. Maraschek, P. de Marne, A. Mlynek, P. Schneider, J. Schweinzer, J. Stober, T. Szepesi, K. Thomsen, W. Treutterer, E. Wolfrum, and the ASDEX Upgrade Team. High-density h-mode operation by pellet injection and elm mitigation with the new active in-vessel saddle coils in asdex upgrade. *Nuclear Fusion*, 52(2):023017, 2012.

[MBB+11] S. H. Müller, J. A. Boedo, K. H. Burrell, J. S. deGrassie, R. A. Moyer, D. L. Rudakov, and W. M. Solomon. Experimental investigation of the role of fluid turbulent stresses and edge plasma flows for intrinsic rotation generation in diii-d *h*-mode plasmas. *Phys. Rev. Lett.*, 106:115001, Mar 2011.

[MD08] J. R. Myra and D. A. D'Ippolito. Resonance cone interaction with a self-consistent radio-frequency sheath. *Phys. Rev. Lett.*, 101:195004, Nov 2008.

[MD10a] K. Miki and P. H. Diamond. Role of the geodesic acoustic mode shearing feedback loop in transport bifurcations and turbulence spreading. *Physics of Plasmas*, 17(3):032309, 2010.

[MD10b] J. R. Myra and D. A. D'Ippolito. Slow-wave propagation and sheath interaction in the ion-cyclotron frequency range. *Plasma Physics and Controlled Fusion*, 52(1):015003, 2010.

[MD11] K. Miki and P. Diamond. Novel states of pre-transition edge turbulence emerging from shearing mode competition. *Nuclear Fusion*, 51(10):103003, 2011.

[MOL+02] M. Mahdavi, T. Osborne, A. Leonard, M. Chu, E. Doyle, M. Fenstermacher, G. McKee, G. Staebler, T. Petrie, M. Wade, S. Allen, J. Boedo, N. Brooks, R. Colchin, T. Evans, C. Greenfield, G. Porter, R. Isler, R. L. Haye, C. Lasnier, R. Maingi, R. Moyer, M. Schaffer, P. Stangeby, J. Watkins, W. West, D. Whyte, and N. Wolf. High performance h mode plasmas at densities above the greenwald limit. *Nuclear Fusion*, 42(1):52, 2002.

[MRS09] P. Manz, M. Ramisch, and U. Stroth. Physical mechanism behind zonal-flow generation in drift-wave turbulence. *Phys. Rev. Lett.*, 103:165004, Oct 2009.

[MXTT11] P. Manz, M. Xu, S. C. Thakur, and G. R. Tynan. Nonlinear energy transfer during the transition to drift-interchange turbulence. *Plasma Physics and Controlled Fusion*, 53(9):095001, 2011.

[NO89] R. V. Nieuwenhove and G. V. Oost. Experimental evidence for sheath effects at the icrf antenna and ensuing changes in the plasma boundary during icrf on textor. *Journal of Nuclear Materials*, 162:288 – 291, 1989.

[OWB+13] R. Ochoukov, D. Whyte, D. Brunner, I. Cziegler, B. LaBombard, B. Lipschultz, J. Myra, J. Terry, and S. Wukitch. Investigation of rf-enhanced plasma potentials on alcator c-mod. *Journal of Nuclear Materials*, 438:S875 – S878, 2013.

[OWB+14] R. Ochoukov, D. G. Whyte, D. Brunner, D. A. D'Ippolito, B. LaBombard, B. Lipschultz, J. R. Myra, J. L. Terry, and S. J. Wukitch. Icrf-enhanced plasma potentials in the sol of alcator c-mod. *Plasma Physics and Controlled Fusion*, 56(1):015004, 2014.

[Per89] F. Perkins. Radiofrequency sheaths and impurity generation by icrf antennas. *Nuclear Fusion*, 29(4):583, 1989.

[PH09] L. Patacchini and I. H. Hutchinson. Kinetic solution to the mach probe problem in transversely flowing strongly magnetized plasmas. *Phys. Rev. E*, 80:036403, Sep 2009.

[PY03] C. Parmesan and G. Yohe. A globally coherent fingerprint of climate change impacts across natural systems. *Nature*, 421(6918):37–42, 01 2003.

[RBG+99] J. Rice, P. Bonoli, J. Goetz, M. Greenwald, I. Hutchinson, E. Marmar, M. Porkolab, S. Wolfe, S. Wukitch, and C. Chang. Central impurity toroidal rotation in icrf heated alcator c-mod plasmas. *Nuclear Fusion*, 39(9):1175, 1999.

[RDZ98] B. N. Rogers, J. F. Drake, and A. Zeiler. Phase space of tokamak edge turbulence, the *L-H* transition, and the formation of the edge pedestal. *Phys. Rev. Lett.*, 81:4396–4399, Nov 1998.

[RGH+98] J. Rice, M. Greenwald, I. Hutchinson, E. Marmar, Y. Takase, S. Wolfe, and F. Bombarda. Observations of central toroidal rotation in icrf heated alcator c-mod plasmas. *Nuclear Fusion*, 38(1):75, 1998.

[RGJ+07] H. Reimerdes, A. M. Garofalo, G. L. Jackson, M. Okabayashi, E. J. Strait, M. S. Chu, Y. In, R. J. La Haye, M. J. Lanctot, Y. Q. Liu, G. A. Navratil, W. M. Solomon, H. Takahashi, and R. J. Groebner. Reduced critical rotation for resistive-wall mode stabilization in a near-axisymmetric configuration. *Phys. Rev. Lett.*, 98:055001, Feb 2007.

[RHD+11] J. E. Rice, J. W. Hughes, P. H. Diamond, Y. Kosuga, Y. A. Podpaly, M. L. Reinke, M. J. Greenwald, O. D. Gürcan, T. S. Hahm, A. E. Hubbard, E. S. Marmar, C. J. McDevitt, and D. G. Whyte. Edge temperature gradient as intrinsic rotation drive in alcator *c*-mod tokamak plasmas. *Phys. Rev. Lett.*, 106:215001, May 2011.

[Ric16] J. E. Rice. Experimental observations of driven and intrinsic rotation in tokamak plasmas. *Plasma Physics and Controlled Fusion*, 58(8):083001, 2016.

[RICd+07] J. Rice, A. Ince-Cushman, J. deGrassie, L.-G. Eriksson, Y. Sakamoto, A. Scarabosio, A. Bortolon, K. Burrell, B. Duval, C. Fenzi-Bonizec, M. Greenwald, R. Groebner, G. Hoang, Y. Koide, E. Marmar, A. Pochelon, and Y. Podpaly. Inter-machine comparison of intrinsic toroidal rotation in tokamaks. *Nuclear Fusion*, 47(11):1618, 2007.

[RLM+04] J. Rice, W. Lee, E. Marmar, P. Bonoli, R. Granetz, M. Greenwald, A. Hubbard, I. Hutchinson, J. Irby, Y. Lin, D. Mossessian, J. Snipes, S. Wolfe, and S. Wukitch. Observations of anomalous momentum transport in alcator c-mod plasmas with no momentum input. *Nuclear Fusion*, 44(3):379, 2004.

[RMS+05] M. Ramisch, N. Mahdizadeh, U. Stroth, F. Greiner, C. Lechte, and K. Rahbarnia. $\rho_s$ scaling of characteristic turbulent structures in the torsatron tj-k. *Physics of Plasmas*, 12(3):032504, 2005.

[RPH+03] T. L. Root, J. T. Price, K. R. Hall, S. H. Schneider, C. Rosenzweig, and J. A. Pounds. Fingerprints of global warming on wild animals and plants. *Nature*, 421(6918):57–60, 01 2003.

[RPR+13] J. E. Rice, Y. A. Podpaly, M. L. Reinke, R. Mumgaard, S. D. Scott, S. Shiraiwa, G. M. Wallace, B. Chouli, C. Fenzi-Bonizec, M. F. F. Nave, P. H. Diamond, C. Gao, R. S. Granetz, J. W. Hughes, R. R. Parker, P. T. Bonoli, L. Delgado-Aparicio, L.-G. Eriksson, C. Giroud, M. J. Greenwald, A. E. Hubbard, I. H. Hutchinson, J. H. Irby, K. Kirov, J. Mailloux, E. S. Marmar, and S. M. Wolfe. Effects of magnetic shear on toroidal rotation

in tokamak plasmas with lower hybrid current drive. *Phys. Rev. Lett.*, 111:125003, Sep 2013.

[SBd+07] W. M. Solomon, K. H. Burrell, J. S. deGrassie, R. Budny, R. J. Groebner, J. E. Kinsey, G. J. Kramer, T. C. Luce, M. A. Makowski, D. Mikkelsen, R. Nazikian, C. C. Petty, P. A. Politzer, S. D. Scott, M. A. V. Zeeland, and M. C. Zarnstorff. Momentum confinement at low torque. *Plasma Physics and Controlled Fusion*, 49(12B):B313, 2007.

[SBF+97] W. Suttrop, K. Buchl, J. Fuchs, M. Kaufmann, K. Lackner, M. Maraschek, V. Mertens, R. Neu, M. Schittenhelm, M. Sokoll, and H. Zohm. Tearing mode formation and radiative edge cooling prior to density limit disruptions in asdex upgrade. *Nuclear Fusion*, 37(1):119, 1997.

[SG07] D. Swain and R. Goulding. Iter ion cyclotron system: Overview and plans. *Fusion Engineering and Design*, 82(5Ã¢ÂĂÂŞ14):603 – 609, 2007. Proceedings of the 24th Symposium on Fusion Technology SOFT-24.

[SHH+16] C. Silva, J. Hillesheim, C. Hidalgo, E. Belonohy, E. Delabie, L. Gil, C. Maggi, L. Meneses, E. Solano, M. Tsalas, and J. Contributors. Experimental investigation of geodesic acoustic modes on jet using doppler backscattering. *Nuclear Fusion*, 56(10):106026, 2016.

[SJB+98] D. F. H. Start, J. Jacquinot, V. Bergeaud, V. P. Bhatnagar, G. A. Cottrell, S. Clement, L.-G. Eriksson, A. Fasoli, A. Gondhalekar, C. Gormezano, G. Grosshoeg, K. Guenther, P. Harbour, L. D. Horton, A. Howman, H. Jackel, O. N. Jarvis, K. D. Lawson, C. Lowry, M. Mantsinen, F. B. Marcus, R. Monk, E. Righi, F. G. Rimini, G. J. Sadler, G. R. Saibene, R. Sartori, B. Schunke, S. Sharapov, A. C. C. Sips, M. Stamp, and P. van Belle. D-t fusion with ion cyclotron resonance heating in the jet tokamak. *Phys. Rev. Lett.*, 80:4681–4684, May 1998.

[SMM+99] W. Suttrop, V. Mertens, H. Murmann, J. Neuhauser, J. Schweinzer, and ASDEX-Upgrade Team. Operational limits for high edge density h-mode tokamak operation. *Journal of Nuclear Materials*, 266-269:118 – 123, 1999.

[SMR11] U. Stroth, P. Manz, and M. Ramisch. On the interaction of turbulence and flows in toroidal plasmas. *Plasma Physics and Controlled Fusion*, 53(2):024006, 2011.

[SRB+14] P. Simon, M. Ramisch, A. A. Beletskii, A. Dinklage, M. Endler, S. Marsen, B. Nold, U. Stroth, P. Tamain, and R. Wilcox. Scaling and transport analyses based on an international edge turbulence database. *Plasma Physics and Controlled Fusion*, 56(9):095015, 2014.

[Sta00] P. C. Stangeby. *The Plasma Boundary of Magnetic Fusion Devices*. Institute of Physics Publishing Bristol, 2000.

[SY85] G. Sivashinsky and V. Yakhot. Negative viscosity effect in largeÃćÂĂÂŘscale flows. *The Physics of Fluids*, 28(4):1040–1042, 1985.

[TAG+16] S. C. Thakur, K. Adriany, J. J. Gosselin, J. McKee, E. E. Scime, S. H. Sears, and G. R. Tynan. Laser induced fluorescence measurements of axial velocity, velocity shear, and parallel ion temperature profiles during the route to plasma turbulence in a linear magnetized plasma device. *Review of Scientific Instruments*, 87(11):11E513, 2016.

[TBC+14] S. C. Thakur, C. Brandt, L. Cui, J. J. Gosselin, A. D. Light, and G. R. Tynan. Multi-instability plasma dynamics during the route to fully developed turbulence in a helicon plasma. *Plasma Sources Science and Technology*, 23(4):044006, 2014.

[TCD+16] G. R. Tynan, I. Cziegler, P. H. Diamond, M. Malkov, A. Hubbard, J. W. Hughes, J. L. Terry, and J. H. Irby. Recent progress towards a physics-based understanding of the h-mode transition. *Plasma Physics and Controlled Fusion*, 58(4):044003, 2016.

[TCG+04] C. D. Thomas, A. Cameron, R. E. Green, M. Bakkenes, L. J. Beaumont, Y. C. Collingham, B. F. N. Erasmus, M. F. de Siqueira, A. Grainger, L. Hannah, L. Hughes, B. Huntley, A. S. van Jaarsveld, G. F. Midgley, L. Miles, M. A. Ortega-Huerta, A. Townsend Peterson, O. L. Phillips, and S. E. Williams. Extinction risk from climate change. *Nature*, 427(6970):145–148, 01 2004.

[TD87] D. R. Thayer and P. H. Diamond. Thermally driven convective cells and tokamak edge turbulence. *Physics of Fluids*, 30(12):3724–3734, 1987.

[Ter00] P. W. Terry. Suppression of turbulence and transport by sheared flow. *Rev. Mod. Phys.*, 72:109–165, Jan 2000.

[TFM09] G. R. Tynan, A. Fujisawa, and G. McKee. A review of experimental drift turbulence studies. *Plasma Physics and Controlled Fusion*, 51(11):113001, 2009.

[TGM+16] S. C. Thakur, J. J. Gosselin, J. McKee, E. E. Scime, S. H. Sears, and G. R. Tynan. Development of core ion temperature gradients and edge sheared flows in a helicon plasma device investigated by laser induced fluorescence measurements. *Physics of Plasmas*, 23(8):082112, 2016.

[THY+06] G. R. Tynan, C. Holland, J. H. Yu, A. James, D. Nishijima, M. Shimada, and N. Taheri. Observation of turbulent-driven shear flow in a cylindrical laboratory plasma device. *Plasma Physics and Controlled Fusion*, 48(4):S51, 2006.

[TMA+07] M. Takechi, G. Matsunaga, N. Aiba, T. Fujita, T. Ozeki, Y. Koide, Y. Sakamoto, G. Kurita, A. Isayama, and Y. Kamada. Identification of a low plasma-rotation threshold for stabilization of the resistive-wall mode. *Phys. Rev. Lett.*, 98:055002, Feb 2007.

[TXD+13] G. Tynan, M. Xu, P. Diamond, J. Boedo, I. Cziegler, N. Fedorczak, P. Manz, K. Miki, S. Thakur, L. Schmitz, L. Zeng, E. Doyle, G. McKee, Z. Yan, G. Xu, B. Wan, H. Wang, H. Guo, J. Dong, K. Zhao, J. Cheng, W. Hong, and L. Yan. Turbulent-driven low-frequency sheared eÃĆÂăÃČÂŮÃĆÂăb flows as the trigger for the h-mode transition. *Nuclear Fusion*, 53(7):073053, 2013.

[UND05] U. D. P. UNDP. *The Human Development Report 2005: International Cooperation at a Crossroads*. UNDP, New York, 2005.

[VRC+02] M. Valovic, J. Rapp, J. G. Cordey, R. Budny, D. C. McDonald, L. Garzotti, A. Kallenbach, M. A. Mahdavi, J. Ongena, V. Parail, G. Saibene, R. Sartori, M. Stamp, O. Sauter, J. Strachan, W. Suttrop, and contributors to the EFDA-JET Workprogramme. Long timescale density peaking in jet. *Plasma Physics and Controlled Fusion*, 44(9):1911, 2002.

[WBB+82] F. Wagner, G. Becker, K. Behringer, D. Campbell, A. Eberhagen, W. Engelhardt, G. Fussmann, O. Gehre, J. Gernhardt, G. v. Gierke, G. Haas, M. Huang, F. Karger, M. Keilhacker, O. Klüber, M. Kornherr, K. Lackner, G. Lisitano, G. G. Lister, H. M. Mayer, D. Meisel, E. R. Müller, H. Murmann, H. Niedermeyer, W. Poschenrieder, H. Rapp, H. Röhr, F. Schneider, G. Siller, E. Speth, A. Stäbler, K. H. Steuer, G. Venus, O. Vollmer, and Z. Yü. Regime of improved confinement and high beta in neutral-beam-heated divertor discharges of the asdex tokamak. *Phys. Rev. Lett.*, 49:1408–1412, Nov 1982.

[WBB+15] G. M. Wallace, S. G. Baek, P. T. Bonoli, I. C. Faust, B. L. LaBombard, Y. Lin, R. T. Mumgaard, R. R. Parker, S. Shiraiwa, R. Vieira, D. G. Whyte, and S. J. Wukitch. High field side launch of rf waves: A new approach to reactor actuators. *AIP Conference Proceedings*, 1689(1):030017, 2015.

[WBD+95] J. R. Wilson, C. E. Bush, D. Darrow, J. C. Hosea, E. F. Jaeger, R. Majeski, M. Murakami, C. K. Phillips, J. H. Rogers, G. Schilling, J. E. Stevens, E. Synakowski, and G. Taylor. Ion cyclotron range of frequency heating of a deuterium-tritium plasma via the second-harmonic tritium cyclotron resonance. *Phys. Rev. Lett.*, 75:842–845, Jul 1995.

[WC11] J. Wesson and D. J. Campbell. *Tokamaks*. Oxford University Press, 2011.

[WCM+90] A. J. Wootton, B. A. Carreras, H. Matsumoto, K. McGuire, W. A. Peebles, C. P. Ritz, P. W. Terry, and S. J. Zweben. Fluctuations and anomalous

transport in tokamaks. *Physics of Fluids B: Plasma Physics*, 2(12):2879–2903, 1990.

[WGH+89] J. Wesson, R. Gill, M. Hugon, F. SchÃČÂijller, J. Snipes, D. Ward, D. Bartlett, D. Campbell, P. Duperrex, A. Edwards, R. Granetz, N. Gottardi, T. Hender, E. Lazzaro, P. Lomas, N. L. Cardozo, K. Mast, M. Nave, N. Salmon, P. Smeulders, P. Thomas, B. Tubbing, M. Turner, and A. Weller. Disruptions in jet. *Nuclear Fusion*, 29(4):641, 1989.

[WGO+13] S. J. Wukitch, M. L. Garrett, R. Ochoukov, J. L. Terry, A. Hubbard, B. Labombard, C. Lau, Y. Lin, B. Lipschultz, D. Miller, M. L. Reinke, D. Whyte, and Alcator C-Mod Team. Characterization and performance of a field aligned ion cyclotron range of frequency antenna in alcator c-moda). *Physics of Plasmas*, 20(5), 2013.

[WKMH95] R. E. Waltz, G. D. Kerbel, J. Milovich, and G. W. Hammett. Advances in the simulation of toroidal gyroÃćÂĂÂŘlandau fluid model turbulence. *Physics of Plasmas*, 2(6):2408–2416, 1995.

[WLL+09] S. Wukitch, B. LaBombard, Y. Lin, B. Lipschultz, E. Marmar, M. Reinke, and D. Whyte. Icrf specific impurity sources and plasma sheaths in alcator c-mod. *Journal of Nuclear Materials*, 390-391:951–954, 2009.

[XHS+13] Y. Xu, C. Hidalgo, I. Shesterikov, M. Berte, P. Dumortier, M. V. Schoor, M. Vergote, A. KrÃČÂđmer-Flecken, R. Koslowski, and the TEXTOR Team. Role of symmetry-breaking induced by $e_r \times b$ shear flows on developing residual stresses and intrinsic rotation in the textor tokamak. *Nuclear Fusion*, 53(7):072001, 2013.

[XNR+03] X. Q. Xu, W. M. Nevins, T. D. Rognlien, R. H. Bulmer, M. Greenwald, A. Mahdavi, L. D. Pearlstein, and P. Snyder. Transitions of turbulence in plasma density limits. *Physics of Plasmas*, 10(5):1773–1781, 2003.

[XTD+11] M. Xu, G. R. Tynan, P. H. Diamond, C. Holland, J. H. Yu, and Z. Yan. Generation of a sheared plasma rotation by emission, propagation, and absorption of drift wave packets. *Phys. Rev. Lett.*, 107:055003, Jul 2011.

[XTD+12] M. Xu, G. R. Tynan, P. H. Diamond, P. Manz, C. Holland, N. Fedorczak, S. C. Thakur, J. H. Yu, K. J. Zhao, J. Q. Dong, J. Cheng, W. Y. Hong, L. W. Yan, Q. W. Yang, X. M. Song, Y. Huang, L. Z. Cai, W. L. Zhong, Z. B. Shi, X. T. Ding, X. R. Duan, and Y. Liu. Frequency-resolved nonlinear turbulent energy transfer into zonal flows in strongly heated *l*-mode plasmas in the hl-2a tokamak. *Phys. Rev. Lett.*, 108:245001, Jun 2012.

[XTH+09] M. Xu, G. R. Tynan, C. Holland, Z. Yan, S. H. Muller, and J. H. Yu. Study of nonlinear spectral energy transfer in frequency domain. *Physics of Plasmas*, 16(4):042312, 2009.

[XTH+10] M. Xu, G. R. Tynan, C. Holland, Z. Yan, S. H. Muller, and J. H. Yu. Fourier-domain study of drift turbulence driven sheared flow in a laboratory plasma. *Physics of Plasmas*, 17(3):032311, 2010.

[YMF+14] Z. Yan, G. R. McKee, R. Fonck, P. Gohil, R. J. Groebner, and T. H. Osborne. Observation of the *l*-*h* confinement bifurcation triggered by a turbulence-driven shear flow in a tokamak plasma. *Phys. Rev. Lett.*, 112:125002, Mar 2014.

[YXD+10] Z. Yan, M. Xu, P. H. Diamond, C. Holland, S. H. Müller, G. R. Tynan, and J. H. Yu. Intrinsic rotation from a residual stress at the boundary of a cylindrical laboratory plasma. *Phys. Rev. Lett.*, 104:065002, Feb 2010.

[ZLD+06] K. J. Zhao, T. Lan, J. Q. Dong, L. W. Yan, W. Y. Hong, C. X. Yu, A. D. Liu, J. Qian, J. Cheng, D. L. Yu, Q. W. Yang, X. T. Ding, Y. Liu, and C. H. Pan. Toroidal symmetry of the geodesic acoustic mode zonal flow in a tokamak plasma. *Phys. Rev. Lett.*, 96:255004, Jun 2006.